TESIS DE LA UNIVERSIDAD
DE ZARAGOZA

2024

49

Kunmeng Zhu

Direct oxidation of methane to formaldehyde in conventional reactors and two-zone fluidized bed reactor using SiO2-based catalysts

Director/es
Menéndez Sastre, Miguel Alejandro
Shen, Xiaodong

ISSN 2254-7606

Prensas de la Universidad
Universidad Zaragoza

Servicio de Publicaciones

ISSN 2254-7606

Tesis Doctoral

DIRECT OXIDATION OF METHANE TO FORMALDEHYDE IN CONVENTIONAL REACTORS AND TWO-ZONE FLUIDIZED BED REACTOR USING SIO2-BASED CATALYSTS

Autor

Kunmeng Zhu

Director/es

Menéndez Sastre, Miguel Alejandro
Shen, Xiaodong

UNIVERSIDAD DE ZARAGOZA
Escuela de Doctorado

Programa de Doctorado en Ingeniería Química y del Medio Ambiente

2023

Universidad
Zaragoza
1542

Doctoral Thesis

DIRECT OXIDATION OF METHANE TO FORMALDEHYDE IN CONVENTIONAL REACTORS AND TWO-ZONE FLUIDIZED BED REACTOR USING SIO2-BASED CATALYSTS

Author

Kunmeng Zhu

Directors

Menéndez Sastre, Miguel Alejandro
Xiaodong Shen

UNIVERSITY OF ZARAGOZA
School of Doctorate

PhD Programme in Chemical and Environment Engineering

2023

Direct oxidation of methane to formaldehyde in conventional reactors and two-zone fluidized bed reactor using SiO_2-based catalysts

Author

Kunmeng Zhu

Directors:

Menéndez Sastre, Miguel Alejandro
Xiaodong Shen

PhD Programme in Chemical and Environment Engineering

University of Zaragoza, 2023

Table of Content

Abstract

With the increasing depletion of fossil energy sources and the highly volatile prices of crude oil, natural gas has received increasing attention as an important source of clean fossil energy and as a chemical feedstock. Researchers have been working on the conversion of methane (CH_4), a major component of natural gas, into liquid fuels such as formaldehyde (HCHO) that are easy to store and transport and have high added value. The challenge in the conversion of CH_4 is to overcome the high stability of the C-H bond of CH_4 while avoiding its excessive oxidation. Therefore, there is a need to develop highly selective oxidation catalysts and to design reactors that can efficiently suppress the continuous oxidation of HCHO. Numerous studies have shown that SiO_2 can be used as a catalyst support for the direct catalytic oxidation of CH_4. SiO_2 aerogels are good candidates for support materials due to the low density, high porosity and high specific surface area, etc. The dispersion of Fe sites can achieve high selectivity for HCHO, MoO_3 can help eliminate iron sites on the catalyst surface that are detrimental to the selective oxidation of CH_4, and $FePO_x$ catalysts can be used in the oxidation of CH_4 with O_2 exhibited high selectivity. In a catalyst reactor, the full mixing of catalyst particles in the fluidized state in a fluidized bed reactor (FBR) allows for efficient heat and mass transfer compared to a fixed bed reactor. The reduction of gas-phase oxygen in the reaction zone in a two-zone fluidized bed reactor (TZFBR) can improve the selectivity for the target product.

In this thesis, SiO_2 aerogel (SA) support, Fe-MoO_x/SiO_2 aerogel (FMSA) and $FePO_x$/SiO_2 aerogel (FPSA) candidate catalyst materials were prepared by heating reflux and sol-gel methods in combination with ethanol supercritical drying techniques. Meanwhile, $FePO_x$/SiO_2 particle (FPSP) candidate catalyst materials were prepared by impregnation method. The SiO_2 aerogel and its composites exhibited a mesoporous structure composed of spherical particles with uniform pore size distribution, and the specific surface area could reach over 1000 m^2/g. The extremely high specific surface area provided a good dispersion bed for the active components, and the active components were uniformly distributed in the composites. The catalytic performance of FPSP was compared with that of SiO_2 aerogel-based composite catalyst materials, and FPSP was used for experimental testing of catalytic reactions in FBR and TZFBR.

Candidate catalyst screening was carried out in a fixed bed reactor. By examining the influence of experimental conditions on the catalytic reaction, it was found that a pre-oxidation reaction prior to the catalytic experiment, at a reaction experiment temperature of 650°C, a reaction flow rate of 162.5 mL/min, a catalyst mass of 0.6 g, a CH_4/O_2 ratio of 1/1 and the introduction of water at 62%, the spherical SiO_2 aerogel-based catalyst 4-FPSA obtained higher HCHO selectivity and the 4-FPSP catalysts with sizes of 160~315 μm obtained higher HCHO yields. The 4-FPSP catalysts were used in FBR and TZFBR. The influence of minimum fluidization velocity, catalyst size, oxygen partial pressure and flow rate on the catalytic reaction in FBR were discussed, as well as the influence of experimental process parameters such as catalyst support, CH_4 introduction point, introduction of inert diluent gas and flow rate on the catalytic reaction in TZFBR. The catalytic reaction in TZFBR achieved higher HCHO selectivity (2.18 times) and higher HCHO yield (1.46 times) compared to FBR.

Keywords: SiO_2; methane; direct oxidation; formaldehyde; two-zone fluidized bed reactor

Resumen

Ante el creciente agotamiento de las fuentes de energía fósiles y la gran volatilidad de los precios del crudo, el gas natural ha recibido cada vez más atención como fuente importante de energía fósil limpia y como materia prima química. Los investigadores han estado trabajando en la conversión del metano (CH_4), uno de los principales componentes del gas natural, en combustibles líquidos como el formaldehído (HCHO), fáciles de almacenar y transportar y con un alto valor añadido. El reto en la conversión del CH_4 es superar la gran estabilidad del enlace C-H del CH_4 evitando al mismo tiempo su oxidación excesiva. Por lo tanto, es necesario desarrollar catalizadores de oxidación altamente selectivos y diseñar reactores que puedan suprimir eficazmente la oxidación consecutiva del HCHO. Numerosos estudios han demostrado que el SiO_2 puede utilizarse como soporte catalítico para la oxidación catalítica directa del CH_4. Los aerogeles de SiO_2 son buenos candidatos como materiales de soporte debido a su baja densidad, alta porosidad y alta superficie específica, etc. La dispersión de los centros activos de Fe puede lograr una alta selectividad para HCHO, y la presencia de MoO_3 puede ayudar a eliminar los centros activos de hierro en la superficie del catalizador que son perjudiciales para la oxidación selectiva de CH_4, y los catalizadores $FePO_x$ se pueden utilizar en la oxidación de CH_4 con O_2, reacción para la que han mostrado alta selectividad. La mezcla completa de partículas de catalizador en un reactor de lecho fluidizado (FBR) permite una transferencia eficiente de calor y masa en comparación con un reactor de lecho fijo. La reducción de la presión parcial de oxígeno en fase gaseosa en la zona de reacción en un reactor de lecho fluidizado de dos zonas (TZFBR) puede mejorar la selectividad hacia el producto objetivo.

En esta tesis, se prepararon materiales candidatos a catalizadores de aerogel de SiO_2 (SA), aerogel de Fe-MoO_x/SiO_2 (FMSA) y aerogel de $FePO_x$/SiO_2 (FPSA) mediante los métodos de reflujo térmico y sol-gel en combinación con técnicas de secado supercrítico con etanol. Además, se prepararon materiales catalíticos de $FePO_x$/SiO_2 (FPSP) mediante el método de impregnación. El aerogel de SiO_2 y sus compuestos presentaban una estructura mesoporosa compuesta por partículas esféricas con una distribución uniforme del tamaño de los poros, y la superficie específica podía alcanzar más de 1000 m^2/g. La superficie específica extremadamente alta facilita la dispersión de los componentes activos, y éstos se distribuyeron uniformemente en los compuestos. El rendimiento catalítico del FPSP se comparó con el de los catalizadores compuestos basados en aerogeles de SiO_2, y el FPSP se utilizó para pruebas experimentales de reacciones catalíticas en FBR y TZFBR.

La selección entre los catalizadores candidatos se llevó a cabo en un reactor de lecho fijo. Se examinó la influencia de las condiciones experimentales en la reacción catalítica, se comprobó que tras una reacción de pre-oxidación previa al experimento catalítico, y operando a una temperatura de 650°C, un caudal de reacción de 162,5 mL/min, una masa de catalizador de 0,6 g, una relación CH_4/O_2 de 1/1 y una fracción molar de agua en la alimentación del 62%, el catalizador 4-FPSA basado en aerogeles esféricos de SiO_2 obtuvo una mayor selectividad de HCHO y los catalizadores 4-FPSP con tamaños de 160~315 μm obtuvieron mayores rendimientos de HCHO. Los catalizadores 4-FPSP se utilizaron en FBR y TZFBR. Se analizó la influencia del tamaño del catalizador, la presión parcial de oxígeno y el caudal en la reacción catalítica en FBR, así como la influencia de parámetros experimentales del proceso como el soporte del catalizador, el punto de introducción del CH_4, la introducción de gas diluyente inerte y el caudal en la reacción catalítica en TZFBR. La reacción catalítica en TZFBR alcanzó una mayor selectividad a HCHO (2,18 veces) y un mayor rendimiento a HCHO (1,46 veces) en comparación con FBR.

Palabras clave: SiO_2; metano; oxidación directa; formaldehído; reactor de lecho fluidizado de dos zonas

Chapter 1 Introduction

With the increasing depletion of fossil energy sources and the significant fluctuation of crude oil prices, there is a growing interest in using abundant and renewable natural gas as an important source of clean fossil energy and chemical feedstock[1, 2]. Natural gas is a multi-component mixed gaseous fossil fuel existing in gas fields, coal seams, oil fields and shale formations, and is the third largest energy source in the world after coal and oil. Compared with coal, oil and other energy sources, natural gas has advantages such as clean and high safety calorific value, and its position in the world's energy structure is becoming more and more important[3]. The main component of natural gas is methane, which usually contains 83% to 99%[4]. Methane is abundant in nature and widely distributed in all regions of the world, with proven reserves of about 190 trillion cubic meters, mainly in the Middle East, Russia, the United States and China. In particular, shale gas (unconventional natural gas stored in organic rich shale and its interlayer in an adsorbed or free state) and combustible ice (natural gas hydrate) discovered in recent years further enhance the potential reserves of methane. Compared with other hydrocarbons, methane has a higher combustion heat (approximately 56 $kJ \cdot g^{-1}$) and is a highly attractive and feasible feedstock for refining and environmentally friendly chemical processing. Therefore, it is of great significance to study and utilize methane as a new carbon-based resource to replace petroleum.

Since most natural gas and shale gas in the world are distributed in remote areas with inconvenient transportation and far away from the market, it is not convenient for liquefaction transportation. Moreover, the storage environment for liquefied natural gas requires strict requirements, such as methane gas having a boiling point of only 109 K at atmospheric pressure, which inevitably leads to the leakage of liquefied natural gas and poses serious environmental hazards[5]. If directly transported through pipelines or after liquefaction treatment, the process is cumbersome and expensive. The extraction of natural gas hydrates can bring serious greenhouse effects (25 times more than CO_2)

and cause submarine landslides and damage to the marine ecological environment. Therefore, from the perspective of full energy utilization or environmental governance, how to extract and utilize methane hydrates has attracted great attention from scientists around the world. Since the last century, researchers have been working on converting methane into liquid fuels with convenient storage and transportation and high added value, such as olefins, aromatics, methanol, and formaldehyde[6, 7].

Methane is the simplest alkane, the molecular formula is CH_4, and its molecule is a regular tetrahedral structure. This stable non-polar structure makes methane to have very high chemical stability [8, 9]. The C-H bond energy of methane is as high as 440 kJ/mol, the polarizability is very low, while the dissociation energy is very high. The activation of the C-H bond requires a high reaction temperature over a wide range of methane conversions[10]. Therefore, the conversion of methane usually requires harsh reaction conditions such as high temperature and pressure. The harsh reaction conditions make it difficult to control the selectivity of the reaction, which is usually accompanied by a large number of side reactions. The challenge of methane conversion is to overcome the high stability of the C-H bond while avoiding its over-oxidation and improving the selectivity of high value-added chemicals[11].

At present, the utilization of methane can be divided into two basic ways: indirect method and direct method. In industry, the use of natural gas mainly adopts indirect conversion method: methane steam is reformed into synthesis gas ($CO+H_2$), and then converted into other high value-added products such as methanol, dimethyl ether, low-carbon olefins, etc. (reactions 1-1 to 1-4). Since the first industrial application of methane steam reforming by BASF in 1926, the syngas ($CO+H_2$) manufacturing process and catalyst development and manufacturing processes have been continuously improved and refined, with 90% of syngas now being derived from methane steam reforming.

$$CH_4 + H_2O \xrightarrow{Ni/Al_2O_3} 3H_2 + CO \qquad (1\text{-}1)$$

$$2CH_4 + O_2 \longrightarrow 4H_2 + 2CO \qquad (1\text{-}2)$$

$$2H_2 + CO \xrightarrow{Cu-Zn/Al_2O_3} CH_3OH \qquad (1\text{-}3)$$

$$2nH_2 + nCO \xrightarrow{Co} C_nH_{2n} + nH_2O \qquad (1\text{-}4)$$

However, methane water vapor reforming to syngas is a strong endothermal process that requires high temperature (800~1000°C) and pressure, the reaction has to cut all the hydrocarbon bonds in the methane molecule, more than 25% of the feedstock natural gas will be burned directly to provide the heat required for the reaction, which consumes a lot of energy. Moreover, the process also has problems such as long process, low one-way conversion, complex process flow and high equipment investment cost[12, 13]. Therefore, it is necessary to find more efficient methane conversion methods.

Compared with traditional indirect routes, the direct conversion of methane into high value-added chemical products needs simple equipment, which can shorten the process route, save costs, and improve carbon atom utilization efficiency[14-18]. At present, research on the direct conversion of methane is extremely abundant, such as selective oxidation of methane to formaldehyde (methanol), oxidative coupling of methane to ethylene, non-oxidative aromatization of methane, oxidative carbonylation of methane to acetic acid, and oxidative sulfonation of methane to methyl sulfonic acid. Among them, the selective oxidation of methane to methanol, formaldehyde and other oxygenated compounds has been studied for more than 100 years[19, 20]. There are at least two difficulties in this research: development of high-performance selective oxidation catalysts and design of reactors to efficiently inhibit the continuous oxidation of methanol or formaldehyde

1.1 Selective oxidation of methane

Table 1.1 presents thermodynamic data for methane conversion reactions. It can be seen that these reactions are thermodynamically spontaneous. Among these reactions, the selective oxidation of methane to products such as formaldehyde and methanol is relatively mild in reaction conditions and thermodynamically more favorable and is considered to be the route with the most industrial potential[21].

Table 1.1 Gibbs free energy variations for a partial reaction related to methane conversion.

Reaction	$\triangle G°$ (kcal mol^{-1})	
	400 K	1000 K
$2CH_4+O_2 \rightarrow C_2H_4+2H_2O$	-34.6	-36.4
$2CH_4+O_2 \rightarrow C_2H_6+H_2O$	-18.4	-14.5
$CH_4+Cl_2 \rightarrow CH_3Cl+HCl$	-26.0	-27.8
$CH_4+Br_2 \rightarrow CH_3Br+HBr$	-8.4	-10.3
$CH_4+1/2O_2 \rightarrow CH_3OH$	-25.4	-18.0
$CH_4+O_2 \rightarrow CH_3OH$	-69.0	-71.2
$CH_4+CO+1/2O_2 \rightarrow CH_3COOH$	-40.0	-10.0

1 kcal=4.18 kJ

However, methane is difficult to be activated, the intermediate products methanol or formaldehyde are more reactive than methane. At the reaction temperature (above 500°C), the intermediate product is more easily deeply oxidized to CO and CO_2. The selective oxidation of methane is a kinetically controlled reaction, and it is possible to achieve the selective synthesis of methanol and formaldehyde by choosing an appropriate catalyst system. It is difficult to combine high aldol selectivity with high methane conversion on most of the reported catalysts so far. Therefore, the catalytic selective oxidation of methane to directly produce C1 oxygenates is still considered to be one of the biggest challenges in the field of catalysis[22-24].

In the decades from the end of the last century to the beginning of this century, there were numerous studies on the selective oxidative conversion of methane to C1 oxygenates, especially methanol and formaldehyde. The dissociation of C-H bond in methane is the key step in methane oxidation, and the dissociation reaction mechanisms can be divided into two categories: dehydrogenation and deprotonation. According to the basic properties of the reaction pathway and the different activation systems, the selective oxidation of methane can be divided into homogeneous catalytic system and heterogeneous catalytic system, as shown in Fig. 1.1[25].

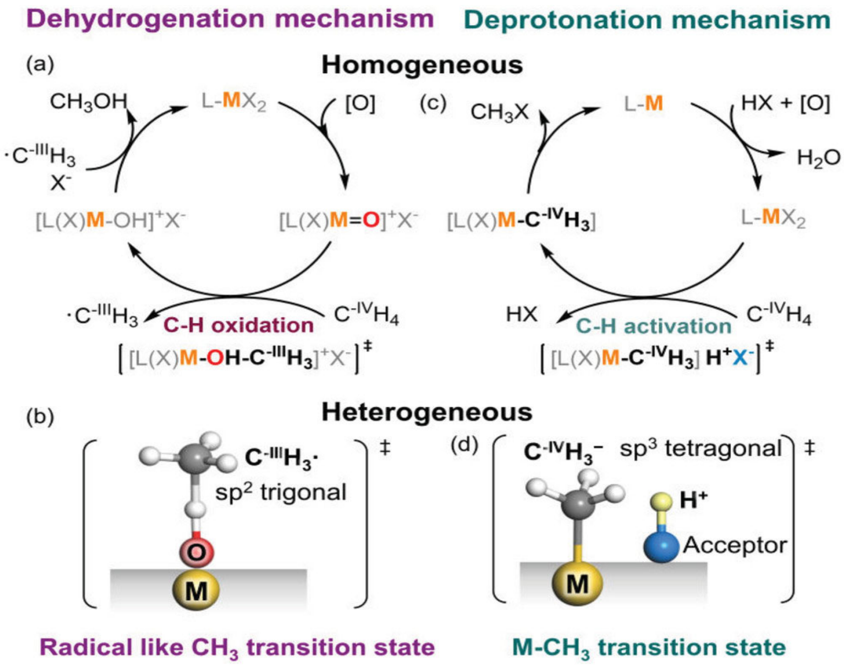

Fig. 1.1 Two mechanisms of methane activation for homogenous and heterogenous catalysis.[25]

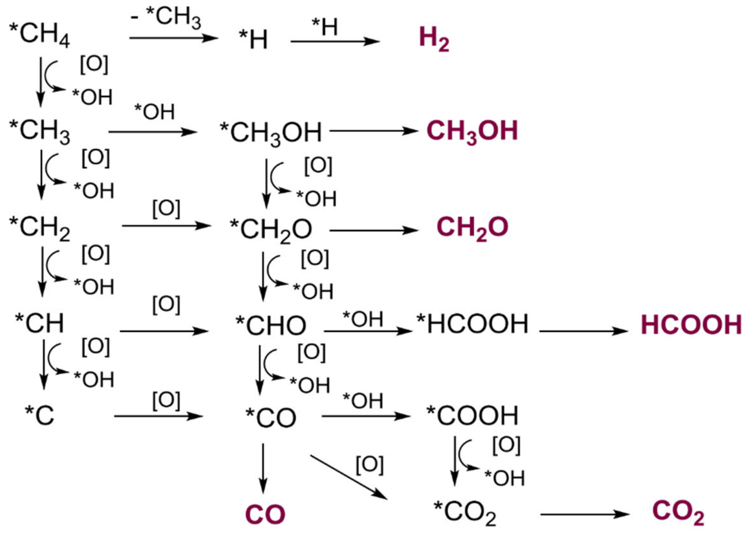

Fig. 1.2 Schematic representation of proposed reaction pathways for methane oxidation with C1-intermediates based on the literature.

The reaction mechanism in Fig. 1.1 only describes the conversion pathway from methane to methanol, while the other steps of methane oxidation are shown in Fig. 1.2.

In methane homogeneous selective oxidation systems, the homogeneous catalysts are usually transition inorganic salt or transition metal ions chelated by organic ligands. They enhance methane reactivity by changing the relative energy of molecular orbitals and/or the polarity of methane, thus improving the selectivity of C1 oxygenated compounds (e.g., methanol, formaldehyde, etc.) at lower reaction temperatures. Although the methane homogeneous selective oxidation system has high product selectivity, it is difficult to apply the methane homogeneous selective oxidation system in industry because the noble metal catalysts used in the homogeneous system are difficult to recycle.

In the past decades, researchers have extensively studied the heterogeneous selective oxidation of methane, and have attempted to develop a variety of heterogeneous catalysts for the selective oxidation of methane. The reaction proceeds via the Mars-van Krevelen mechanism. In particular, lattice oxygen (ie, M=O, where M represents metal) is responsible for methane activation, and the reduced metal sites (M) are activated by gas-phase oxygen to regenerate lattice oxygen active sites. This mechanism has been successfully applied to describe the kinetics of methane oxidation reaction, and the whole reaction cycle process is shown in Fig. 1.3.

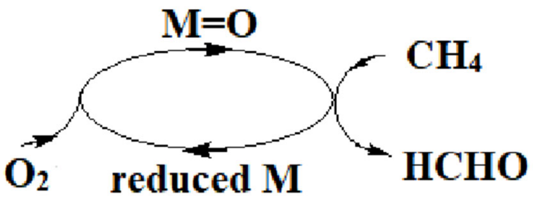

Fig. 1.3 The Mars-van Krevelen mechanism diagram of methane selective oxidation.

Scientific researchers have been committed to improving the yield of formaldehyde, but the repeatable formaldehyde yield of methane multiphase selective oxidation reaction can only reach 3%~4%, its difficult to produce on a large scale. The conversion and selectivity of methane multiphase selective oxidation reactions are usually mutually constrained, resulting in limited formaldehyde yield. Literature research shows that Cu, V, Mo, Fe, Co and multi-component oxides loaded on supports can be used as catalysts for methane selective oxidation. In solid catalyst supports containing transition metal oxides, supports such as TiO_2 and Al_2O_3 are prone to promoting deep oxidation of formaldehyde, which is not conducive to the generation of formaldehyde[26]. SiO_2 supported catalysts exhibit outstanding methane selective oxidation performance.

1.2 Methane selective oxidation catalyst

1.2.1 Molybdenum-based catalysts

Spencer et al.[27] found that loading 1.8 wt% Mo on Cab-O-Sil can obtain 5.3% methane conversion and 32% formaldehyde selectivity (T= 650°C, GHSV= 5000 h^{-1}, CH_4: O_2= 9:1) in 1988. They concluded that Mo-O· radicals were first formed on MoO_3/SiO_2, followed by the formation of methoxy intermediates, as shown in the reaction histories of Fig. 1.4 and Fig. 1.5[28]. If the addition of Na+ to MoO_3/SiO_2 induces further deep oxidation of HCHO to CO, they argue that it is the substitution of =O by -O Na that increases the electron cloud density of oxygen and thus facilitates the attack of nucleophilic groups, leading to the deep oxidation of HCHO.

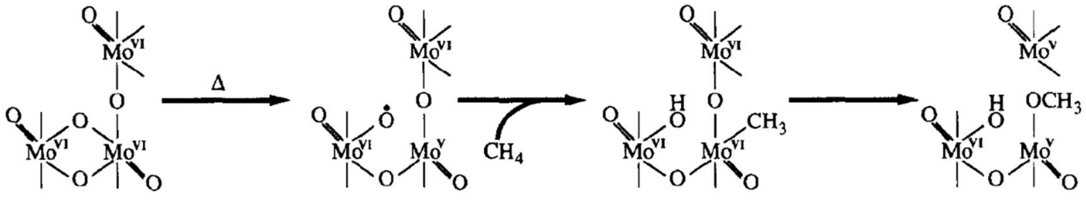

Fig. 1.4 Reaction pathway schematic for initial attack on methane.

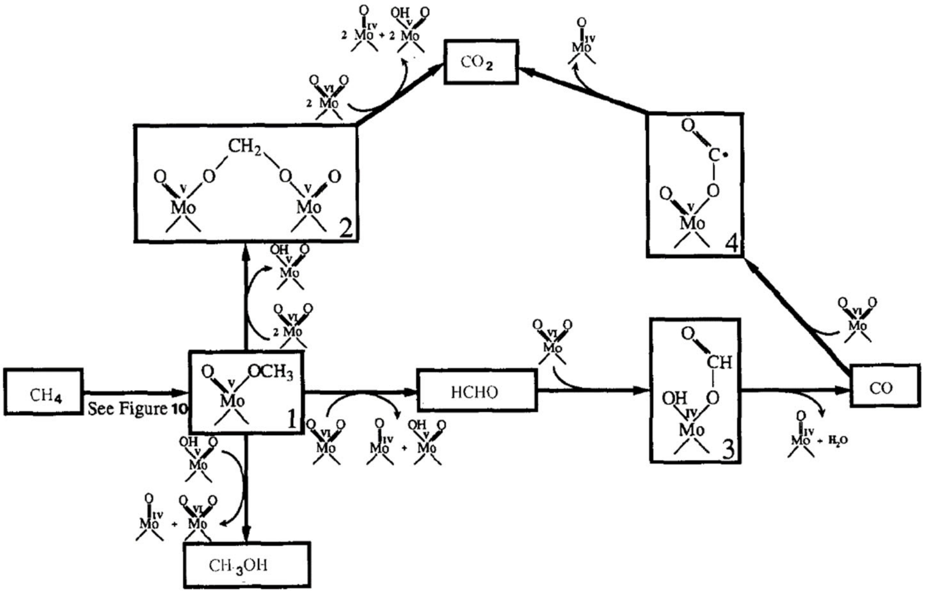

Fig. 1.5 Reaction pathway schematic for methane oxidation reactions.

Smith and Ozkan found that the methane selective oxidation reaction on multimeric MoO_3 is a structure-sensitive reaction, the Mo=O site promoting formaldehyde production, while the Mo-O-Mo bridge oxygen site is more likely to lead to complete oxidation[29]. Smith et al.[30] investigated the influence of MoO_3/SiO_2 catalysts on the activity and selectivity of MoO_3/SiO_2 catalysts. The presence of highly dispersed molybdenum metal species on the catalyst surface at lower MoO_3 loadings, terminated mostly in Mo=O sites. The abundance of Mo=O sites directly affects the conversion and selectivity of the partial oxidation of methane to formaldehyde. With increasing loading, these sites are converted to polymolybdate species at the expense of Mo=O sites to form more Mo-O-Mo bridging sites. At high loadings, crystalline MoO_3 forms on the catalyst surface, allowing direct conversion of methane to CO_x and reducing reaction selectivity. At low levels (<1.3 wt%), tetrahedral molybdenum species predominate. At high loadings, more polymolybdates lead to a decrease in dispersion. The Mo/HZSM-5 catalyst prepared by washing with ammonia solution and using impregnation method by Lucas et al. could almost completely remove the polymeric polymolybdate species from the catalyst surface, forming tetrahedrally isolated Mo=O species with better dispersion, exhibiting better HCHO selectivity and improved HCHO yields compared to the untreated catalyst [31].

Bell et al.[32] found that during the reaction of methane selective oxidation to formaldehyde, about 50~500 ppm MoVI is reduced to MoIV, O_2 reacts with the reduced Mo species to form peroxide species, and methane then reacts with the peroxide species to produce formaldehyde, as in Fig. 1.6. They introduced that the maximum one-way yield of methane to formaldehyde is directly influenced by the reaction temperature and CH_4/O_2 ratio through a reaction kinetic model, with a maximum of 7.0% theoretical one-way yield of formaldehyde on 4.5 wt% MoO_x/SiO_2 can be obtained, and 9.5% theoretical one-way yield of formaldehyde can be obtained if the exposed SiO_2 surface can be completely inerted.

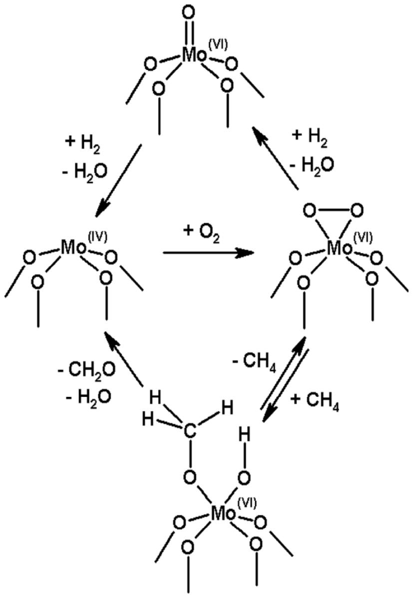

Fig. 1.6 Proposed Mechanism of CH_4 Oxidation at Isolated, SiO_2-supported MoO_x Sites.

Chempath et al.[33] proposed that the reaction mechanism of methane oxidation to formaldehyde on isolated MoO_x/SiO_2 catalysts with single oxygen (Fig. 1.7) and double oxygen (Fig. 1.8) on molybdenum species active sites. The methane consumption rate calculated based on the model of molybdenum species active sites is consistent with the kinetic data obtained from experiments. At the same time, the authors found that the reduced MoIV center reacted with adsorbed oxygen O_2 to generate peroxide species, which further reacted with methane to form formaldehyde. the amount of MoVI reduced to MoIV was much less than 1%.

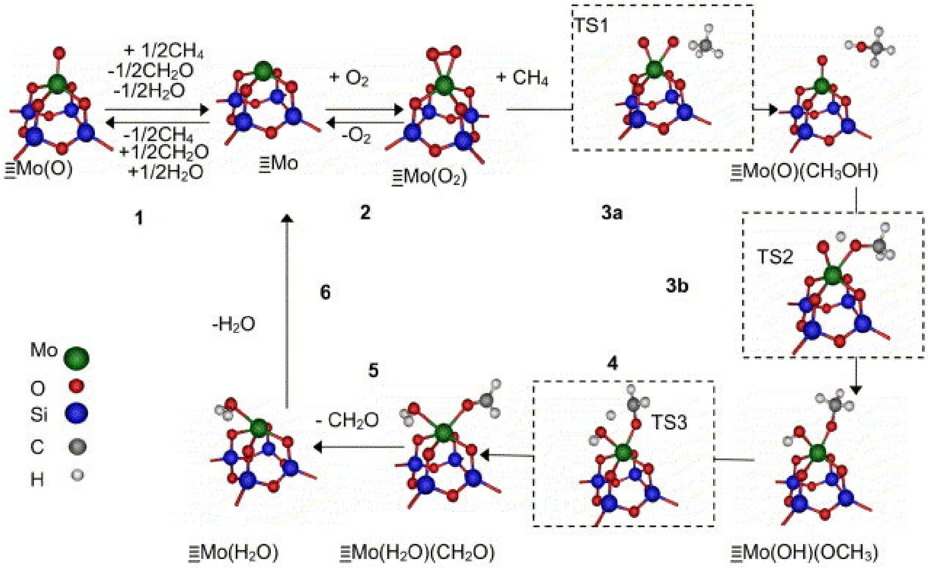

Fig. 1.7 The reaction mechanism of methane selective oxidation over mono-oxo molybdate species.

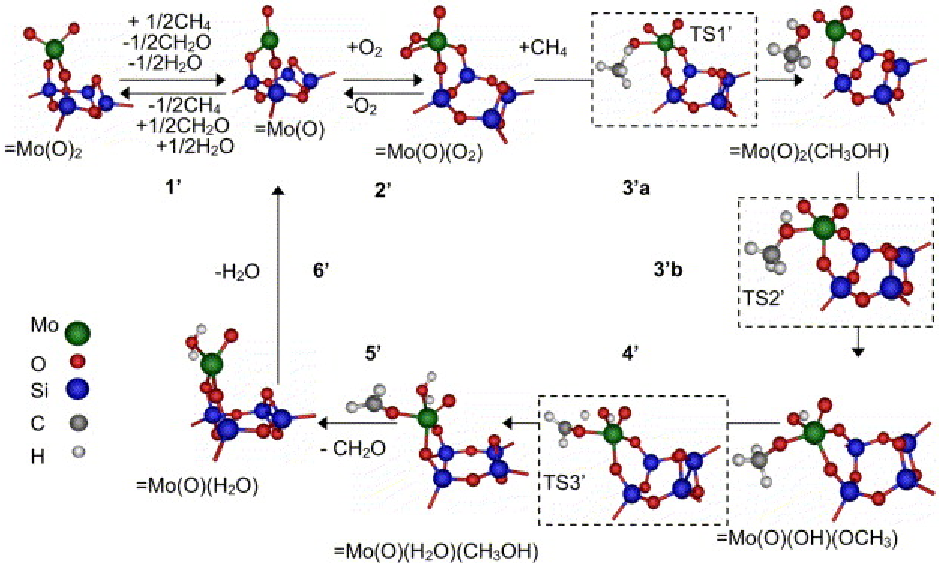

Fig. 1.8 The reaction mechanism of methane selective oxidation over di-oxo molybdate species.

Liu et al. [34] reported the selective oxidation of methane over MoO_3/SiO_2 catalyst with N_2O as oxidant in the presence of water vapor. It was found that the selectivity of methanol and formaldehyde reached 78% when the methane conversion was 3%, CO was the main by-product, and a small amount of water vapor added to the feed gas could significantly improve the catalytic performance of the catalyst. Sugino et al.[35] further investigated the selective oxidation of methane to methanol and formaldehyde over MoO_3/SiO_2 catalysts with highly dispersed active sites under excess amount of water vapor. The reaction took place at 600°C, the feed gas consisted of methane, oxygen and water vapor. The results show that the selectivity of oxygenated compounds is positively correlated with the water vapor content, and when the percentage of water vapor in the feed increases, the selectivity of oxygenated compounds in the product increases, while the selectivity of CO and CO_2 decreases. This is caused by the formation of silicomolybdic acid on the silica support surface. The authors prepared another silica-loaded silicomolybdic acid catalyst and applied it to the selective oxidation of methane under the same conditions. Although the silicomolybdic acid readily cleaved to SiO_2 and MoO_3 at 600°C in the absence of water vapor, it produced oxygenated compounds well when the water vapor in the feed exceeded 50%. The methane conversion is about 25%, and the selectivity of oxygenated compounds reaches 90%, which indicates that silicomolybdic acid is the active species of methane selective oxidation reaction on MoO_3/SiO_2 catalyst in the presence of excess water vapor.

1.2.2 Iron-based catalysts

Kobayashi et al.[36] have reported that the addition of a very small amount of iron (Fe/Si = 0.05) to SiO_2 significantly promoted formaldehyde production, inferred that isolated Fe^{3+} on SiO_2 was the key to promote methane activation and formaldehyde production. Carlos et al. prepared Fe/SiO_2 catalysts with different iron loadings (0.1-0.5 wt%) by sol-gel method and used the catalysts in the reaction of selective oxidation of methane to formaldehyde. The results showed that the conversion of methane was 8.6%

and the yield of formaldehyde was 0.31 g_{HCHO}/kg_{cat} at a reaction temperature of 650°C. Combined with SEM and TEM, it was found that the conversion of methane and the selectivity of formaldehyde were related to the dispersion of Fe. The higher the dispersion, the higher the conversion of methane and the lower the selectivity of formaldehyde.

The iron-oxygen tetrahedra in $FePO_4$ are separated by phosphorus-oxygen tetrahedra, so that the iron ions exist in tetracoordinated form. The FeO_x nanoclusters were modified with the phosphorus additive resulting in the formation of $FePO_4$ nanoclusters. The active sites of iron are dispersed by the phosphorus clusters and thus become isolated active centers. The formaldehyde selectivity can be improved and the formaldehyde yield increased at the same methane conversion. The structure-property correlation studies of methane selective oxidation reactions over FeO_x/SBA-15 or FeO_x-SiO_2 (prepared by sol-gel method) catalysts with different iron contents further confirmed that the isolated FeIII active sites can promote formaldehyde production[37, 38].

Wang et al. found that the hydrogen promotion effect was exhibited on $FePO_4$. With the addition of H_2 to the CH_4-O_2 system, there was a significant increase in the rate of methane conversion and the selectivity of formaldehyde and methanol[39, 40]. It is inferred that peroxide species were first generated on the $FePO_4$ surface, followed by reactivation of methane by surface peroxide species (Fig. 1.9). The catalytic performance of $FePO_4$ nanoparticles confined in the pores of mesoporous molecular sieves in the selective oxidation reaction of methane was also systematically investigated by Wang et al [41]. The study shows that highly dispersed iron phosphate species on molecular sieves are more reducible and have better catalytic properties than iron phosphate in the crystalline phase.

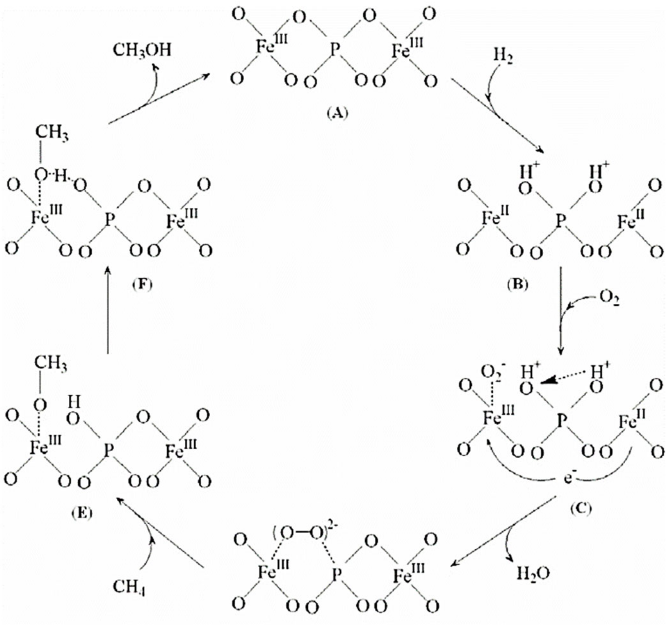

Fig. 1.9 The proposed reaction mechanism for the selective oxidation of CH_4 to CH_3OH by H_2-O_2 over active iron site.

Five catalysts ($FePO_4$, $Fe_3O_3(PO_4)$, $Fe_4(P_2O_7)_3$, $Fe_2P_2O_7$ and α-Fe_2O_3) were synthesized by the sol-gel method by Matsuda et al [42]. The results showed that the Fe/P molar ratio had a significant effect on the oxidation catalytic effect. The methane conversion increased with the increase of Fe/P molar ratio, but the formaldehyde selectivity was decreasing. The $FePO_4$ catalyst with Fe/P molar ratio of 1 synthesized by malic acid-assisted method exhibited the highest formaldehyde selectivity. Although the methane oxidation capacity of Fe_2O_3 is higher than that of $FePO_4$, Fe_2O_3 leads to a deep oxidation of methane to CO_2. The combination of a homogeneous Lewis acidic iron site and a weakly basic phosphate site may contribute to the activation of the C-H bond in methane and inhibit the formation of the deep oxidation product CO_2. The combination of uniform Lewis acid iron sites and weakly alkaline phosphate sites may contribute to the activation of the C-H bond in methane and inhibit the production of the deep oxidation product CO_2. Wang et al. investigated the performance of SBA-15 loaded $FePO_4$ in the partial oxidation of CH_4 with O_2[43]. The results showed that $FePO_4$ species with loadings below 40 wt.% were encapsulated within the mesoporous channels of SBA-15 and that these encapsulated $FePO_4$ clusters could be reduced at much lower temperatures than crystalline $FePO_4$. The SBA-15-loaded $FePO_4$ catalyst exhibited higher CH_4 conversion and HCHO selectivity than the unloaded and MCM-41-loaded catalysts during partial oxidation of CH_4 with O_2. The catalyst loaded with 5 wt.% showed the highest HCHO selectivity as well as the highest HCHO yield for a CH_4 conversion.

1.2.3 Other catalysts

Bhasin et al. combined MoO_3/SiO_2 and SrO/La_2O_3 to obtain high formaldehyde yields (187 g/(kg $_{cat}$)$^{-1}$h^{-1}) using a double layered catalyst bed reactor [44]. The SrO/La_2O_3 catalyst has the function of activating methane to produce methyl radicals, which bed is closer to the reactor inlet, while the MoO_3/SiO_2 catalyst is responsible for capturing methyl radicals to produce the target product formaldehyde.

Transition metal-substituted phosphorus-molybdenum heteropoly acid ($PMo_{12-x}M_xO_{40}$, M=Co, Zr) catalysts have good activity for methane selective oxidation reactions[45, 46], but too little work has been done on this aspect. Mansouri et al. investigated the catalytic performance of transition metal-modified [PW11M] (M=Fe, Co, Ni) catalysts for the selective oxidation of methane to methanol and formaldehyde in the temperature range of 600~650°C at atmospheric pressure using O_2 and N_2O as oxidants[47]. It was found that the cobalt- and iron-doped polyoxometalate catalysts had the best methane activation and selectivity for the target products methanol and formaldehyde. The activity and selectivity of N_2O were higher than that of O_2. The increase in catalyst activity was correlated with the increased oxidation of the metal clusters. Each of the two oxidants reacts with methane in different pathways. Nedyalkova et al. partially replaced zirconium with iron in a cerium oxide-zirconium oxide catalyst for the selective oxidation of methane to formaldehyde reaction[48]. Fe^{3+} was inserted into the lattice of mixed oxides and 25% replacement of zirconium ions by iron ions did not cause phase rejection of iron oxide. The introduction of Fe enhanced the reducibility of the modified ternary oxide species Ce^{4+}. Although the specific surface area of the composite oxide was low, the catalyst still had a high methane activation capacity, and the selectivity of formaldehyde was largely dependent on the iron content of the inserted oxide.

Loaded WO_3 catalysts have a high methane activation capacity and selective oxidation catalytic performance[49, 50]. On W/ZSM-5 catalysts, formaldehyde selectivity depends on the dispersion and properties of the tungsten-oxygen species, the specific surface area of the catalyst and the loading of tungsten metal affect the dispersion and properties of the tungsten-oxygen species and the catalytic performance of the catalyst. The yield of formaldehyde on WO_3/SiO_2 is closely related to the density and activity of the three active sites: both the active site on the silica surface and the terminal W=O site contribute to the production of formaldehyde, while the W-O-W bridge bond leads to the complete oxidation of methane or CO. Erdohelyi et al. investigated the methane selective oxidation performance of $K/WO_3/SiO_2$, K_2WO_4 loaded on different supports and WO_3/SiO_2 catalysts[51]. On the WO_3/SiO_2 catalyst, the main products of the reaction were HCHO and CO_x, while on the potassium-containing catalyst, mainly C2 hydrocarbons were formed. The product distribution was affected by the nature of the support, the catalyst was most active when the support was alumina. Methane was mainly generated on WO_3/SiO_2, while C2 was generated highly selectively on the K_2WO_4/SiO_2 surface. Lucas et al. chose two different specific surface areas of SiO_2 as supports and prepared WO_3/SiO_2 with a loading of 0.8~15.8% using tungstate as the precursor[50]. Both catalysts were able to oxidize methane at atmospheric pressure with molecular oxygen as the oxidant. The catalyst with low specific surface area has low tungsten dispersion and strong reduction of the tungsten oxide phase, thus the catalyst has high methane conversion per unit area. The yield of methane is related to three active sites on the W/SiO_2 catalyst: the active site on the SiO_2 surface, the terminal W=O site and the W-O-W site.

In addition to the above-described catalysts such as molybdenum-based and iron-based for methane selective oxidation reactions, metals such as Sb and Cr are also used as active centers for methane activation. Li et al. prepared Sb_2O_3/SiO_2 and Sb_2O_5/SiO_2 catalysts by impregnation method and used these two catalysts in the methane selective oxidation reaction[52]. The results showed that the highly dispersed SbO_x could inhibit the production of CO_2 and facilitate the production of formaldehyde. The yield of formaldehyde could reach 3% at the reaction temperature of 600°C. Wang et al. prepared a Cr/MCM-41 catalyst for the selective oxidation of methane by hydrothermal synthesis[53]. At the reaction temperature of 500°C, the methane conversion was 5.6% and the formaldehyde production rate was 7.15 mol $kgcat^{-1}h^{-1}$. The results showed that the catalysts prepared by hydrothermal synthesis easily formed highly dispersed chromium species on MCM-41, which facilitated the formaldehyde production. Matsumura et al. investigated the possibility of antimony oxide for the selective oxidation of methane[54]. The Sb_2O_4 formed on the diamond surface shows better catalytic activity, while Sb_6O_{13} formed on the silica surface has poor selective oxidation properties.

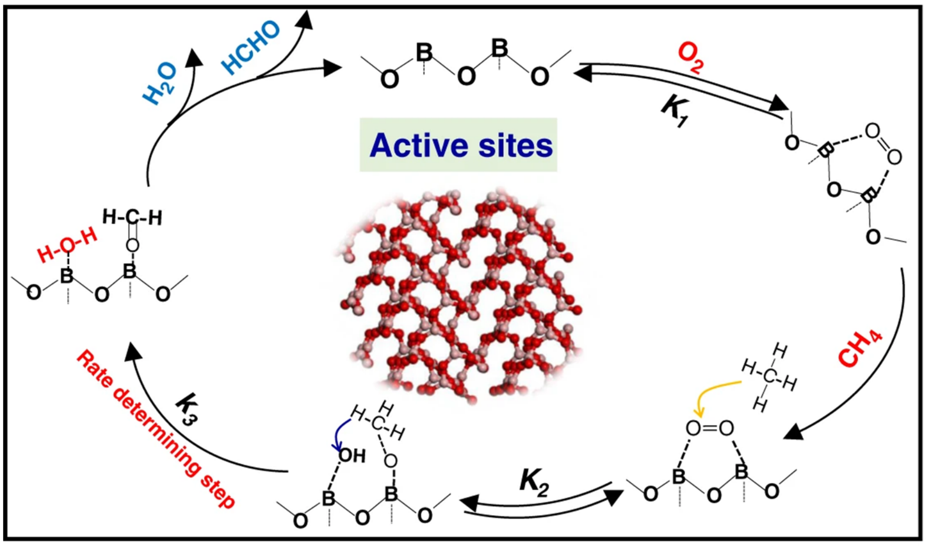

Fig. 1.10 B_2O_3-based catalysts in the partial oxidation of CH_2O and CO.

Tian et al. investigated the good selectivity and stability of B_2O_3-based catalysts in the partial oxidation of CH_2O and CO by methane [18]. The tri-coordinated BO_3 species on the surface is the active centers of the catalysts, the O_2 molecules bound to the electron deficient centers of these BO_3 species are methane-activated oxidants. The reaction mechanism is shown in Fig. 1.10.

Michalkiewic et al. investigated the selective oxidation of methane to formaldehyde on different crystalline forms of Nb_2O_5 and showed that H-Nb_2O_5 and M-Nb_2O_5 with dense stack structure had the highest temporal and yield of formaldehyde, while T-Nb_2O_5 without dense stack structure had the highest yield of formaldehyde loaded on silica[55]. Ohyama et al. investigated the selective oxidation performance of methane over Co/SiO_2 catalysts with different Co loadings at 400~500°C[56]. At lower Co loadings, methane was selectively oxidized to formaldehyde and methanol, while at higher loadings methane was completely oxidized to CO_2. Co(II) single atoms dominated at loadings <0.1wt%, but with increasing loadings, Co_3O_4 nanoparticles became dominant. Using catalytic reactions and theoretical calculations, Tabata et al. investigated the influence of the introduction of germanium ions to tin oxide over $Sn_{1-x}Ge_xO_2$ ($x = 0\sim0.5$) catalysts on the methane selective oxidation performance of the catalysts in the presence of NO[57]. When germanium was introduced, the methane oxidation activity of the catalyst was weakened. When the methane conversion was 10%, the products on the tin oxide catalyst were mainly CO, CO_2 and traces of C2. With the introduction of germanium, there was the formation of formaldehyde. The selectivity of formaldehyde increased with increasing germanium content. The highest selectivity for formaldehyde was achieved when $x= 0.2$.

1.3 SiO_2 aerogel materials and catalytic applications

Aerogel materials are lightweight solid material with a three-dimensional porous network structure formed by the interspersed accumulation of nanoparticles and filled with air as the dispersion medium in the pore structure. Due to their low density (as low as 0.001 g/cm^3), high porosity (up to 99.8%), high specific surface area (>1200 m^2/g) and mesoporous properties (pore size between 1~100 nm), aerogel materials have ultra-low thermal conductivity (as low as 0.012 W/(m·K)), high adsorption capacity and large response area, and have a wide range of applications in thermal insulation, adsorption, photocatalysis and drug delivery. Aerogels were first prepared in 1931 by Professor Kistler of Stanford University, using water glass as the raw material, through the sol-gel method combined with supercritical drying of ethanol, which laid down the basic technical route of aerogel preparation[58]. After 80 years of development, the definition of aerogel material has developed from its initial narrow definition of samples with large specific surface area and low thermal conductivity produced by supercritical drying to a broad definition of gels with air as dispersant. Therefore, the types of aerogels have also developed from a single SiO_2 component to a large family of multi-component, multi-functional and widely used aerogels.

According to the appearance, preparation, pore structure and components, there are many classification methods for aerogel materials. For example, according to the appearance, they can be divided into whole block, granular, powder, fiber and membrane aerogels; according to the drying method, they can be divided into dry gels (normal pressure drying, vacuum drying and microwave drying), freeze gels (freeze drying) and aerogels (ethanol supercritical drying, CO_2 supercritical drying and other supercritical drying of medium); according to the pore size, they can be divided into microporous aerogel (<2 nm), mesoporous aerogel (2~50 nm), macroporous aerogel (>50 nm) and mixed pore aerogel. However, these methods cannot achieve a comprehensive and specific description of aerogels, the composition-based classification method is a more scientific and convenient way to understand their properties.

As shown in Fig. 1.11, aerogels can be classified into inorganic aerogels, organic aerogels and composite aerogels according to their compositions. Inorganic aerogels include oxide aerogels (SiO_2, TiO_2, Al_2O_3, ZnO, ZrO_2 and SnO, etc.), metal monomer aerogels (Fe, Co, Ni, Pd, Au and Ag, etc.) and sulfide aerogels (CuS and CdS). Organic aerogels include carbon aerogels, carbon nanotube aerogels and graphene aerogels, which are mainly made of carbon materials; and cellulose aerogels and polyimide (PI) aerogels, which are mainly made of polymers. Depending on the type of matrix and reinforcing phase, composite aerogels can be classified as binary/ternary oxide composite aerogels (SiO_2-TiO_2, SiO_2-Al_2O_3 and SiO_2-Y_2O_3, etc.), carbon doped composite aerogels, metal doped composite aerogels (Cu- Al_2O_3 and Pd- Al_2O_3, etc.) and fiber mat/porous sheet reinforced aerogel materials[59].

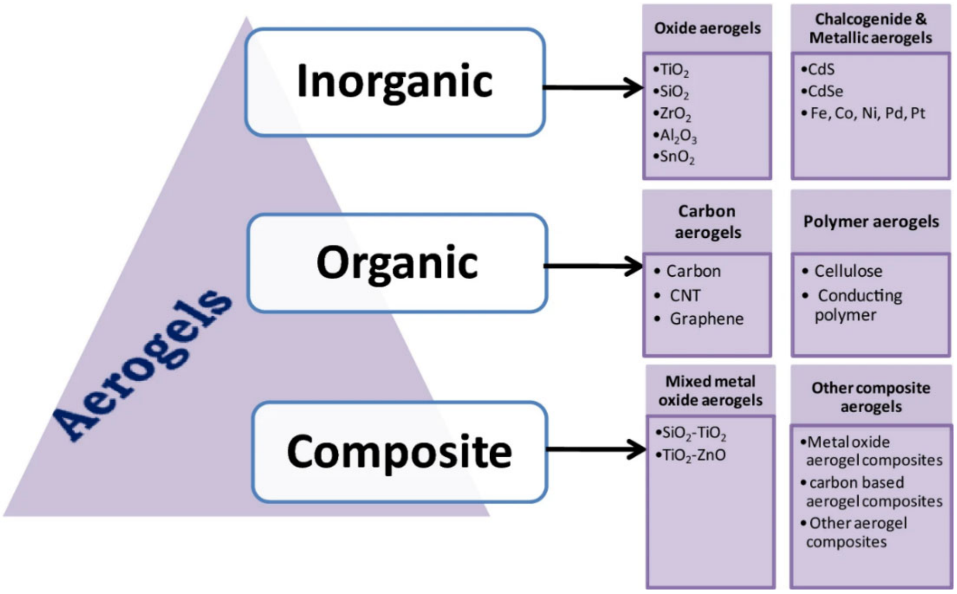

Fig. 1.11 Detailed classification of aerogel materials based on composition.

As the earliest and most used aerogel, SiO_2 aerogel was originally invented with sodium silicate as the precursor. The residual Na^+ in the wet gel had to be removed by solvent replacement in order to obtain a complete and crack-free whole product, which eventually made it impossible to produce on a large scale due to the tedious process and long lead time. In 1968, Professor Teichner successfully synthesised SiO_2 aerogels using tetramethyl orthosilicate (TMOS) as a precursor instead of sodium silicate, which greatly simplified the preparation process [60]. In 1986, Russo adapted the precursor to tetraethyl orthosilicate (TEOS), thus avoiding the hydrolysis of TMOS to produce the toxic solvent methanol. Since the ethanol supercritical drying process required heating and pressurizing ethanol to more than 260°C/10 MPa, which posed safety risks, researchers developed a milder CO_2 supercritical drying process (45°C/10 MPa) in the 1980s using CO_2 instead of ethanol as the supercritical fluid. By now, the basic process flow for the industrialisation of modern SiO_2 aerogels has been formed: sol-gel, aging/solvent replacement, and CO_2 supercritical drying, as shown in Fig. 1.12. Laboratory SiO_2 aerogel materials are still prepared using ethanol as a supercritical fluid due to the high transparency and hydrophobic groups on the surface of the samples obtained by supercritical drying of ethanol.

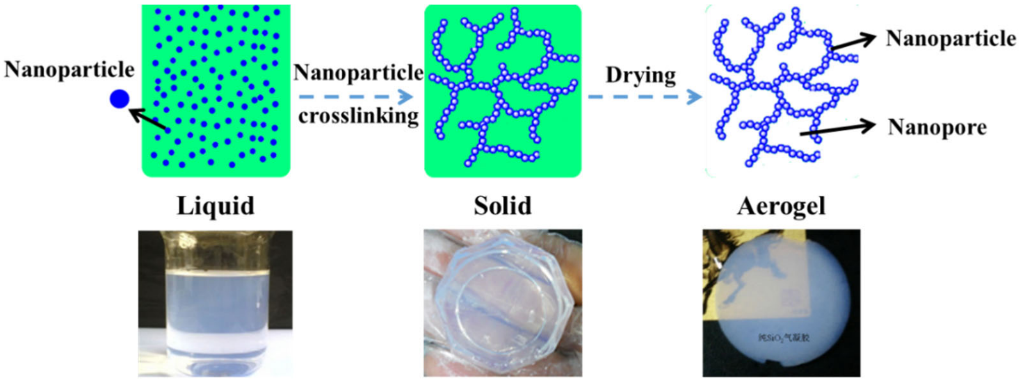

Fig. 1.12 Typical preparation process of aerogel materials.

Due to the advantages such as high specific surface area of SiO_2 aerogels, they are often used as catalyst supports. The active components can be uniformly dispersed in the pore channels of SiO_2 aerogels, thus effectively enhancing the activity, stability and catalytic efficiency of the catalyst system.

The loaded amorphous NiP/SiO_2 aerogel samples with high thermal stability were firstly prepared by Wang et al[61] using sol-gel method. It can be used for the selective hydrogenation of cyclopentene from cyclopentadiene gas-solid phase. In the advanced oxidation process, the catalyst surface-induced generation of highly reactive species or radicals is decisive for the degradation of organic pollutants in the aqueous phase. Zhu et al. prepared a series of rare earth metal-doped anatase TiO_2/SiO_2 composite aerogels by the sol-gel method[62]. The prepared composite aerogel catalysts were able to effectively purify organic dyes in wastewater under solar light. It was found that the doping of rare earth metals not only improved the stability of the crystalline phase of anatase TiO_2 and inhibited the agglomeration of nanoparticles in the aerogel, but also generated oxygen defects on the catalyst surface, which facilitated the separation of

TiO_2 electron-hole pairs, thus enhancing the photocatalytic activity and wastewater treatment effect of TiO_2/SiO_2 composite aerogels.

In addition, Shalygin et al. prepared new HKUST-1@SiO_2 composite aerogel microspheres by sol-gel and oil-in-water emulsification methods for the first time, as shown in Fig. 1.13[63]. The specific surface area of HKUST-1@SiO_2 was found to be efficient in catalytic oxidation of styrene to phenylacetaldehyde, the large particle size facilitated the recycling after the reaction.

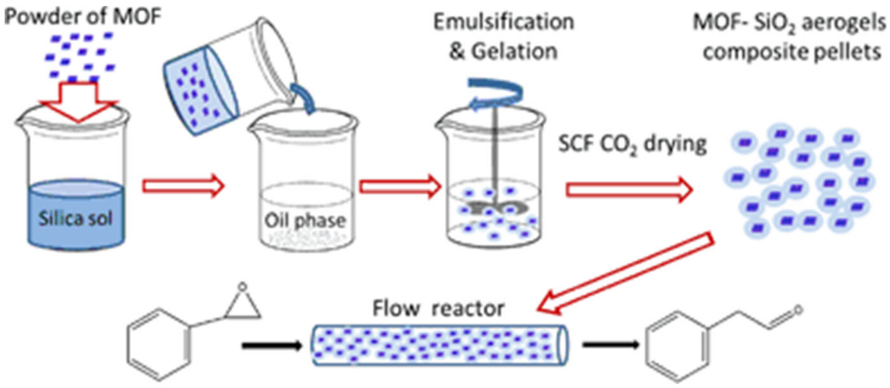

Fig. 1.13 HKUST-1@SiO_2 pellets used as a catalyst for isomerization of styrene oxide to phenyl acetaldehyde in a continuous flow reactor.

Wang et al. synthesized a series of M-Ni/silica (M= Na, K) aerogel catalysts and applied them to n-decane cracking under supercritical conditions, as shown in Fig. 1.14[64]. The results showed that the M-Ni/SiO_2 aerogel catalysts with higher specific surface area, larger pore size, smaller Ni particle size, stronger active metal- support interaction, and higher Ni dispersion due to proper alkalinity were well dispersed in n-decane with better catalytic activity, stability, and anti-coking ability than the wall-covered Ni/SiO_2 catalysts. The results showed that the M-Ni/SiO_2 aerogel catalysts with higher specific surface area were well dispersed in n-decane and had better catalytic activity, stability and anti-coking ability than the wall-coated Ni/SiO_2 catalysts.

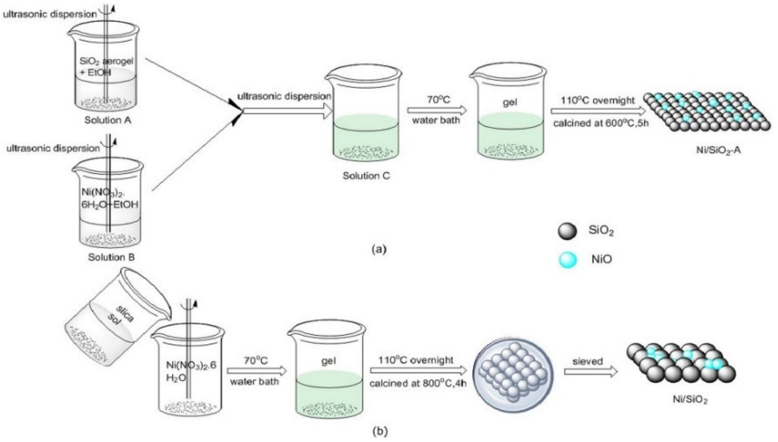

Fig. 1.14 The preparation process of (a) Ni/SiO_2-A and (b) Ni/SiO_2 catalyst.

Prokić-Vidojević et al. prepared Re/Pd-TiO_2/SiO_2 aerogel catalysts by sol-gel method and supercritical drying method, as shown in Fig. 1.15[65]. The amorphous aerogels prepared by the sol-gel and supercritical drying methods have high homogeneity. The conversion of Re/Pd-TiO_2/SiO_2 aerogels with or without the addition of mesitylene to 4,6-DMDBT is 70% and 64% higher than that of conventional Co/Mo catalysts, respectively. The improved catalytic activity could be attributed to the well-dispersed Re and Pd active phases in the catalyst structure.

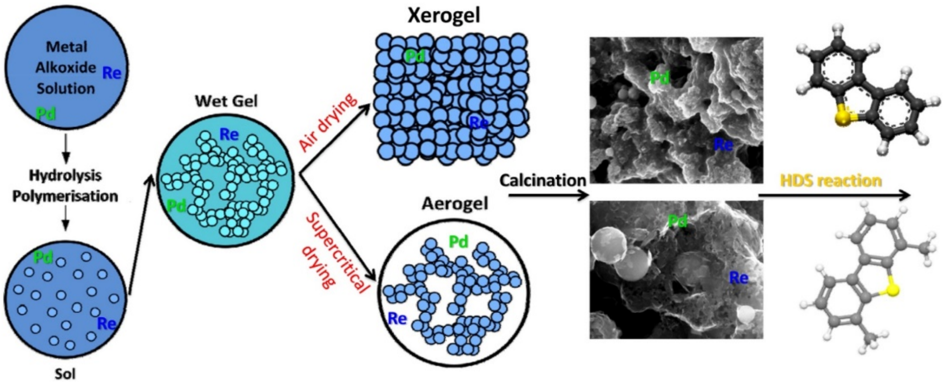

Fig. 1.15 Re/Pd-TiO_2/SiO_2 aerogel catalysts.

Hassan et al. used the sol-gel method to immobilize wavy nickel nanowires (NiNWs) on mesoporous silica (SiO_2) aerogels, as shown in Fig. 1.16[66]. The NiNW-SiO_2 aerogel composites were good CHR non-homogeneous catalysts in both gas and aqueous phases.

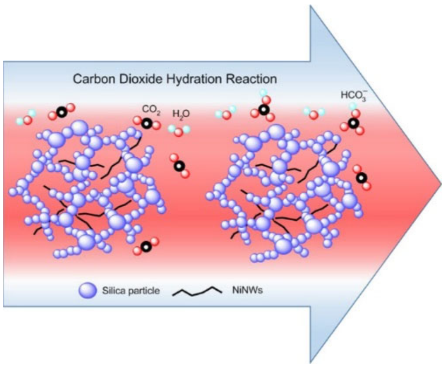

Fig. 1.16 NiNW-SiO_2 aerogels.

Ettekali et al. prepared MoO_3-SiO_2 aerogels with different ratios using micro-mesoporous SiO_2 aerogels as supports (Fig. 1.17), and also evaluated them as catalysts for dibenzothiophene (DBT) oxidation and adsorbents for oxidation products[67]. The results showed that MoO_3 nanoparticles were uniformly distributed on the surface of the silica aerogel. The catalytic activity of DBT oxidation was enhanced due to the increase of MoO_3 content, the increase of active sites and the increased hydrophilicity of the surface to H_2O_2 dissolved in water. The stability of the MoO_3-SiO_2 aerogel catalyst was confirmed by successive oxidative adsorption desulfurization experiments.

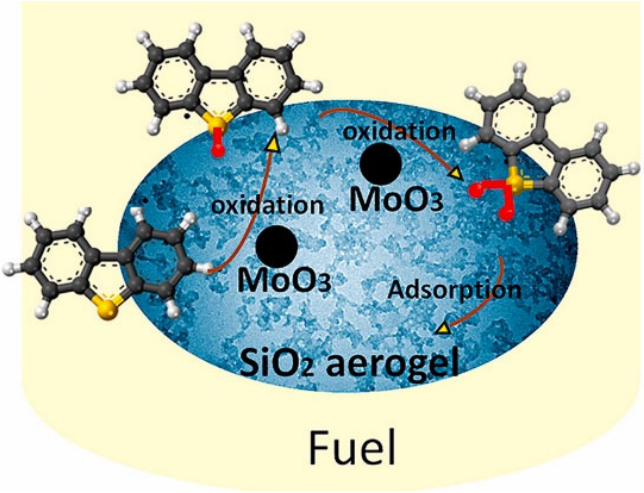

Fig. 1.17 MoO_3-SiO_2 aerogels.

Soubaihi reported the synthesis of silver/silica aerogel (Ag/SiO_2 AG) catalysts by a one-pot sol-gel method[68]. The obtained catalysts are highly stable and less prone to sintering, allowing easy diffusion of reactants to the active site. The catalytic activity for low-temperature CO oxidation was enhanced by preventing the agglomeration of silver nanoparticles in the pores and promoting the dispersion of the active sites to enhance the mass and heat transfer within the mesopores. The catalyst exhibited good thermal stability up to 450°C under repeated cycle times.

Li et al. synthesized spherical mesoporous PWA/SiO_2-Al_2O_3 catalysts based on sol-gel technique and dropwise addition method[69]. For 40wt% PWA/SiO_2-Al_2O_3 exhibited higher conversion (87.97%) and selectivity for diisopropylnaphthalenes (41.41%) and β,β-products (59.82%) than pure acids and active supports. The high conversion is believed to be related to its large number of Brönsted acid sites, high surface area, high dispersion of PWA on the support surface, acidity derived from the PWA anion and the Keggin structure of the active support.

Al Soubaihi et al. synthesized Pd/SiO_2 nanocomposite aerogels with well-dispersed palladium nanoparticles within silica aerogel pores using sol-gel synthesis under supercritical ethanol drying, as shown in Fig. 1.18[70]. The synthesized catalysts exhibited high catalytic activity at low operating temperatures (<200°C), and the enhanced activity towards CO oxidation was attributed to the small Pd particles, the interaction of Pd with the SiO_2 surface, and the good dispersion of Pd particles within the SiO_2 pores.

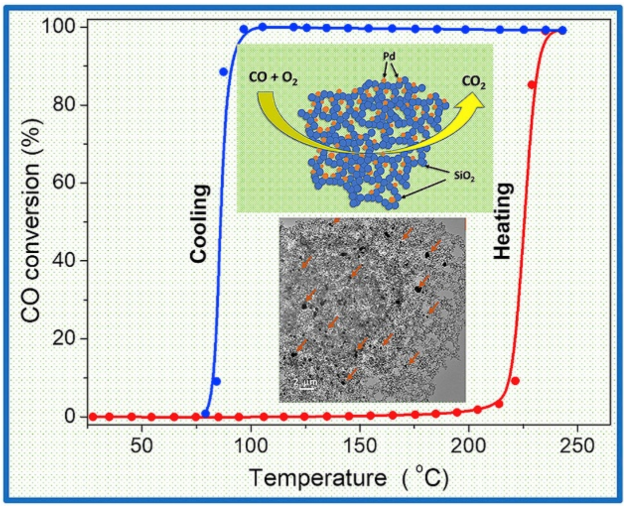

Fig. 1.18 Pd/SiO_2 nanocomposite aerogel.

1.4 Catalytic reactors

The usual procedure for carrying out gas-phase catalytic oxidation consists of mixing the reactants with oxygen and possibly other compounds (e.g. inert diluents) and feeding the mixture into the catalytic reactor. Here, the characteristics and advantages of several different types of reactors are described, including fixed bed reactors, fluidized bed reactors and two-zone fluidized bed reactors.

1.4.1 Fixed bed reactor

Although many of the heterogeneous catalysts have the advantage of being easily separable and regenerable, most of the research has been carried out in batch reactors and no true continuous production has been achieved. Fixed bed reactors are also called filled bed reactors, is a device in which solid catalyst or reactant feedstock particles are packed into a reactor to form a fixed bed for a multi-phase reaction. During the multi-phase reaction, the fixed bed remains stationary and the fluid reacts with it through the fixed bed. Fixed bed reactors offer several advantages when used for continuous reactions in gas-solid two-phase catalytic systems:

(1) The contact area between the fluid and the solid bed is relatively large and can be treated as an ideal replacement flow. As a result, the chemical reaction rate is generally faster in a fixed bed. The amount of catalyst required for the preparation of the same amount of product is usually less in fixed bed reactors.

(2) Low mechanical loss of solid catalyst particles in catalytic reactions, allowing for continuous use over a long period of time;

(3) The residence time of the gas in the fixed bed can be controlled by varying the gas flow rate and bed height, thus facilitating the conversion and product selectivity of the catalytic reaction;

(4) Fixed bed reactors are generally simpler in structure, more stable in reaction, easier to operate and easier to achieve continuous industrial production.

If the active component catalyst is filled directly into a continuous fixed bed reactor, it causes a large bed resistance and the catalyst is easily washed away by the flowing treatment fluid, thus affecting the catalytic effect. Therefore, a suitable support must be selected to load the catalyst.

1.4.2 Fluidized bed reactor

Chemical reactions are always accompanied by thermal effects. Temperature has a strong influence on the rate of reaction and the processes require the timely removal of heat. The main disadvantage of fixed bed reactors is the poor heat transfer performance. As catalyst supports tend to have poor thermal conductivity, the flow rate must not be too high, which causes difficulties in heat transfer and temperature control.

A fluidized bed reactor is a reactor that uses gas or liquid to pass through a layer of granular solids while the solids are in suspension and carry out a gas-solid phase reaction process or a liquid-solid phase reaction process. The basic concept of fluidization is to make a fluid pass through a static bed of solid particles with a surface velocity sufficient to make suspended particles work like a fluid. When fluid is introduced into a static bed at a low velocity, it only passes through the voids of the solid particles while the bed remains fixed. As the velocity increases, the bed expands until the particles are suspended as buoyancy balances resistance and gravity.

At a given velocity (minimum fluidization velocity), the bed is fully suspended[71]. Fluidization gives the system excellent features such as particle mixing, uniform temperature distribution and high mass transfer rates[72]. Various flow patterns can be obtained by controlling the fluidization velocity, such as particle/smooth fluidization, bubbling fluidization, agglomerate fluidization, turbulent fluidization and pneumatic conveying[73].

In a fluidized bed reactor, the fluid containing the adsorbent generally enters from the lower part of the reactor and flows from the bottom up. The adsorbent in the reactor is in a fluidized state and the purified fluid is discharged from the top of the reactor. In order for the adsorbent particles in the reactor to be fluidized, the velocity of the fluid must be higher than the minimum velocity required to fluidize the adsorbent particles, which is the U_{mf}. Depending on the operating process, fluidized bed reactors can be operated intermittently or continuously. When used for adsorption, and depending on the structure of the adsorber, it can be divided into single-stage (single chamber) or multi-stage (multi-chamber). The fluidized bed process has a number of advantages over the fixed bed process.

(1) Continuous and homogeneous mixing of the catalyst in the reactor;

(2) Deactivated or partially deactivated catalysts can be continuously removed, the reaction process is continuous;

(3) The fluidized bed reactor has a high mass and heat transfer rate. The catalyst bed temperature is evenly distributed so that catalyst deactivation due to overheating is reduced to a minimum and the catalyst life can be extended.

The fluidized bed process also has a number of disadvantages.

(1) The intense movement of the catalyst particles in the fluidized bed reactor causes the catalyst to wear out, requiring the use of wear resistant materials as supports;

(2) The use of small particles, the need for particle recovery devices at the reactor outlet and the dust carried by the gas all make post-treatment difficult;

(3) The gas in the bed passes through the bed as bubbles resulting in fluidized bed reactors often having lower yields than fixed beds for the same ratio of catalyst weight/feed flow.

1.4.3 Two-zone fluidized bed reactor

The CREG (Catalysis and Reaction Engineering Group) of the University of Zaragoza has developed an unconventional fluidized bed reactor: two-zone fluidized bed reactor (TZFBR). TZFBR is a device consisting of a fluidized bed in which two chemical reactions take place simultaneously[74]. The diagram of the installation scheme is shown in Fig. 1.19. Oxygen mixed with inert gas is fed into the lower part of the reactor and the hydrocarbons (or compounds that should normally be oxidized) are fed into the middle point of the bed. In this way, two zones are created in the reactor. In the lower zone, the catalyst is oxidized by gas-phase oxygen. This process results in the oxygen in the gas stream being depleted. When the gas stream reaches the hydrocarbon entry point, the oxygen concentration should be close to zero so that oxidation of the hydrocarbon can occur in the absence of gas phase oxygen. In the upper zone, the hydrocarbons are oxidized and reduced by the lattice oxygen in the catalyst. The reaction products, the unconverted reactants and the inert diluent leave the top of the bed together. The good solids circulation characteristics of the fluidized bed provide for solids transfer between the two zones. The system is easy to build on a laboratory scale and has been used for a variety of reactions[75].

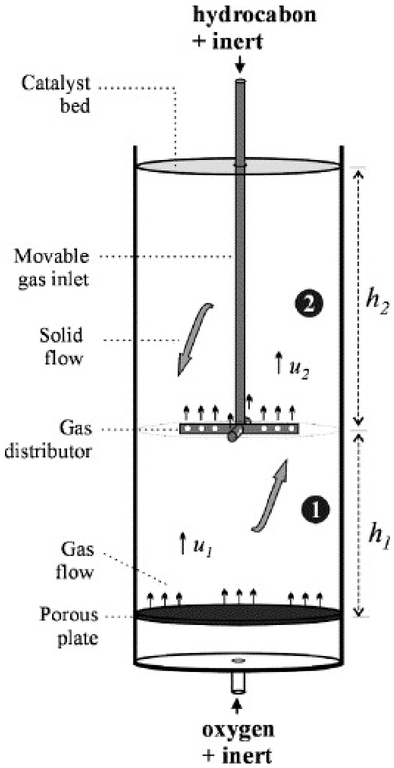

Fig. 1.19 Scheme of a two-zone fluidized bed reactor (TZFBR).

In some cases, for a given conversion rate, the TZFBR is more selective for the desired product than conventional reactors. However, not all catalysts tested achieved selective improvement in the TZFBR. The CREG of the University of Zaragoza has carried out some specific applied research for the TZFBR.

Methane steam reforming (MSR) processes have problems with coke formation when operating at low steam/carbon ratios, while operating at high steam/carbon ratios means high energy consumption. In the TZFBR, steady-state operation can be achieved[76]. The reaction takes place in the upper zone, using steam to fluidize the lower zone and act as a regenerant. In this process, the removal of coke is carried out by steam. Steam reforming of ethanol is possible in the TZFBR, whereas the same experimental operation in a conventional reactor would lead to the formation of coke[77]. This process is very similar to MSR. CO must be removed to achieve the required quality for PEM fuel cells and one of the existing procedures is the preferential oxidation (PROX) reaction. Oxygen can also react with hydrogen as the concentration of hydrogen is much higher than that of CO. The closer the amount of oxygen is to the stoichiometry required for CO combustion, the more selective the catalyst will be.

Selective oxidation of CO can be obtained by using TZFBR[78]. The increased selectivity may be due to the fact that part of the oxygen involved in the reaction is derived from oxygen carried by the catalyst rather than from gas phase oxygen. The catalyst is transferred between the upper and lower zones of the reactor as an oxygen support. CREG of the University of Zaragoza has also found that TZFBR can be used for the direct oxidation of benzene to phenol and that the product distribution changes dramatically depending on the operating conditions[79]. However, the conversion achieved is too low for the catalysts in this work and the industrial process does not appear to be feasible.

The use of TZFBR has been experimentally tested as a method for cleaning tar[80]. The gas from the gasification reactor is free of tar, which is deposited on the catalyst surface in the upper zone of the TZFBR, and tar removal is achieved in the lower zone of the TZFBR.

Based on the previous research on TZFBR, CREG of the University of Zaragoza has developed new reactor types, including Two-section TZFBR, TZFBR with membranes and ICFBR.

In the original design of the TZFBR, the bed sections had the same diameter. However, the airflow required to fluidize the bottom area is higher than that required to regenerate the catalyst. The modification to design the bed area as two sections of different diameters allows the bottom area of the reactor to be operated at lower flow rates which are sufficient for the oxidative regeneration of the catalyst[81, 82]. The reactor device is shown in Fig. 1.20 (b).

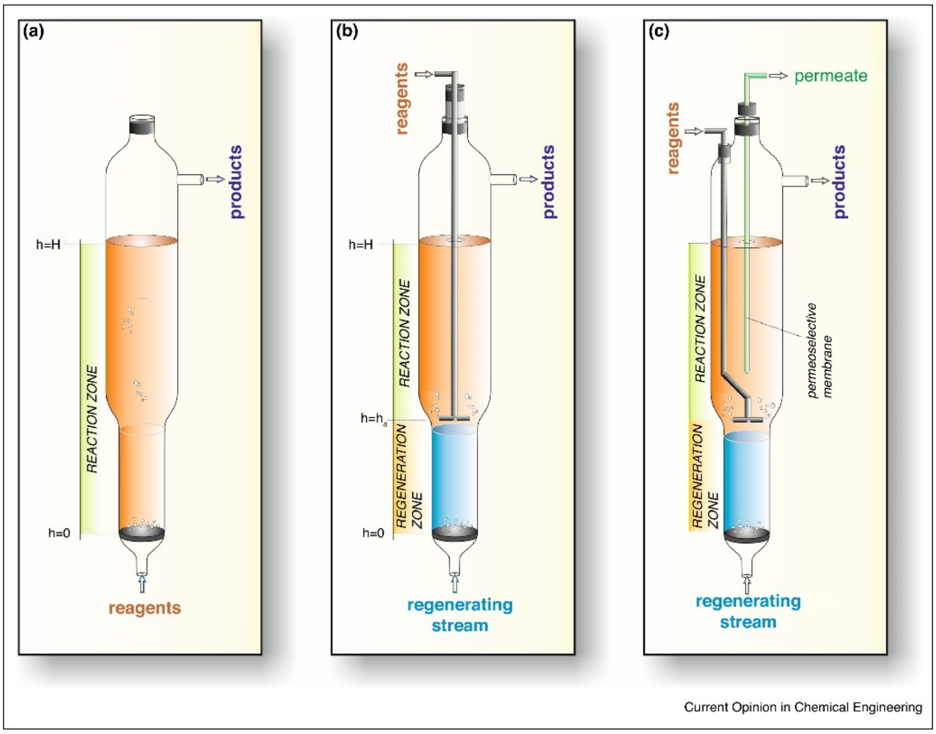

Fig. 1.20 (a) FBR, (b) TZFBR and (c) TZFBR + MB configurations.

The group also developed a reactor that combines TZFBR with a membrane (TZFBR + MB), as shown in Fig 1.20(c). The membrane removes a reaction product from the catalyst bed and helps to achieve higher conversion. This reactor allows three operations to be carried out simultaneously in a single device: (1) a catalytic reaction takes place to obtain the desired product, (2) the oxidative regeneration of the catalyst, (3) the membrane separates one of the reaction products. The latest results of a study on dry reforming of methane show a twofold increase in hydrogen production with TZFBR + MB compared to TZFBR[83]. The ability of TZFBR + MB to achieve steady-state operation under experimental conditions that are not possible in conventional fluidized bed reactors due to coke has been improved.

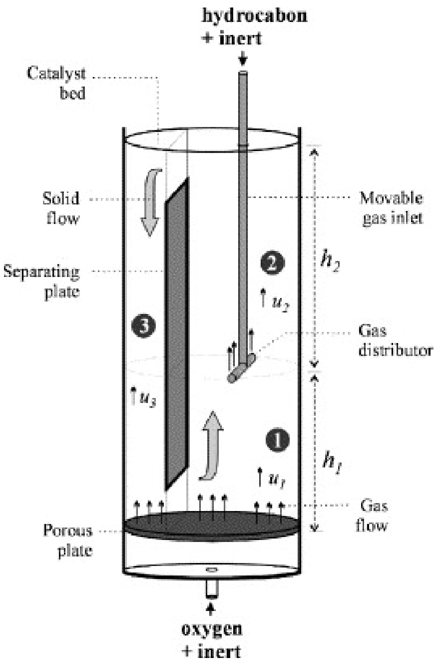

Fig. 1.21 Scheme of an internal circulating fluidized bed reactor (ICFBR).

There are two key issues in the operation of the TZFBR. On the one hand, the gas-phase oxygen must be consumed in the lower part of the reactor; on the other hand, gas back-mixing, especially of hydrocarbons, must be avoided. In a fluidized bed, remixing of the gas occurs in the mixing with the solids in the reactor. If the solids move downwards at a rate higher than the U_{mf}, the solids draw the gas downwards, resulting in unwanted gas remixing. In response to these problems, CREG has developed a system that allows better control of solids flow and avoids gas back-mixing: the Internal Circulating Fluidized Bed Reactor (ICFBR). The reactor scheme is shown in Fig. 1.21. The reactor is divided into two zones by vertical walls. The vertical walls allow solids to be transferred between the two zones via a connection between the lower and upper parts of the bed. A pressure gradient occurs due to the difference in gas velocity in each zone, resulting in the presence of solid flow between the two parts of the bed.

1.5 Thesis topic and the research project

In the face of depleting oil resources, more and more attention are being paid to the direct conversion of methane into liquid fuels such as formaldehyde (HCHO) that are easy to store and transport and have high added value. For the catalytic directly oxidation of methane to HCHO, we have tried to develop a series of SiO_2-based candidate catalyst materials, tested the reactions in different catalytic reactors and adjusted the experimental parameters during the reactions, aiming to improve the selectivity and yield of the catalytic reactions. The research project consists of the following three components:

(1) Using TEOS as the silicon source, $Fe(NO_3)_3 \cdot 9H_2O$ as the iron source, $NH_4H_2PO_4$ as the P source, and MoO_3 powder as the raw material for the synthesis, the SiO_2 aerogel (SA), Fe-MoO_x/SiO_2 aerogel (FMSA) and $FePO_x$/SiO_2 aerogel (FPSA) series of candidate catalyst materials were synthesized by heating reflux and sol-gel method combined with ethanol supercritical drying technology. The overall structure, composition and redox properties of the FMSA catalyst material were investigated by analyzing the microscopic morphology, physical phase, Fourier transform infrared spectroscopy (FTIR), specific surface area and pore structure, XPS and H_2-TPR tests of the composite. Meanwhile, $FePO_x$/SiO_2 particles (FPSP) candidate catalyst materials were obtained by impregnation using SiO_2 precipitation as a support for comparison with SiO_2 aerogel-based composite catalysts in a fixed bed reactor and for catalytic reaction testing in a fluidized bed reactor.

(2) The FMSA, FPSA and FPSP series catalysts were filled in the fixed bed reactor, the experimental parameters of the catalytic reaction were examined in terms of the experimental temperature of the reaction, the pre-oxidation reaction, the amount of

water introduced and the influence of the partial pressure of oxygen and the gas flow rate on the catalytic reaction. Also, the influence of catalyst size, catalyst support type and loading on the catalytic process were examined. The experimental results of different catalysts and different experimental parameters were analyzed for the conversion of CH_4, selectivity of HCHO and yield of HCHO. The optimum experimental parameters are discussed and the catalyst materials that perform better in the catalytic reactions are selected. The experimental results of different catalysts and different experimental parameters were analyzed for CH_4 conversion, HCHO selectivity and HCHO yield. The best experimental parameters were discussed and the catalyst materials that performed better in the catalytic reactions were screened.

The screened candidate catalysts were applied in FBR and TZFBR. The influence of U_{mf}, problems and improvements, catalyst size, oxygen partial pressure and flow rate on the catalytic reaction in the FBR. The influence of experimental process parameters such as catalyst support, CH_4 introduction point, introduction of inert dilution gas and flow rate on the catalytic reaction in TZFBR were discussed. The experimental results of catalytic reactions with different experimental parameters were analyzed for the conversion of CH_4, selectivity and yield of HCHO, comparing the performance of FBR and TZFBR in catalytic reactions.

Chapter 2 Experimental materials and test methods

The aerogel structure composite materials in this thesis were prepared by heating reflux and sol-gel process with TEOS as the silicon source and ethanol as the solvent. SiO_2 was acted as the support of the three-dimensional network skeleton structure in the composite materials. By introducing different components in the preparation process, SiO_2 aerogel (SA), Fe-MoO_x/SiO_2 aerogel (FMSA), $FePO_x/SiO_2$ aerogel (FPSA) structural materials were obtained, respectively. Through basic characterization of the prepared aerogel structure materials, such as density, phase, microstructure morphology, and pore structure, to investigate the morphology and structure characteristics of the aerogel materials. The XPS, H_2-TPR tests, and redox performance were used to analyze the elemental composition of the composite material. The material was applied in a fixed bed reactor to test its ability to directly catalyze the oxidation of methane (CH_4) and selectivity of formaldehyde (HCHO). At the same time, a series of silica based $FePO_x/SiO_2$ particles (FPSP) composite catalyst materials were prepared using SiO_2 precipitation as the raw material through impregnation method for catalytic reaction experiments in fixed bed reactors, FBR and TZFBR. This chapter introduces in detail the preparation experiments, basic characterization and experimental methods of catalytic reactions in catalytic reactors involved in the thesis.

2.1 Experimental materials

Table 2.1 Details of raw materials required for the experiment.

Reagents	Chemical Formula	Purity	Manufacturer
Tetraethyl orthosilicate	$(C_2H_5O)_4Si$	AR	Shanghai Lingfeng Chemical Reagent Co., Ltd.
Absolute ethanol	C_2H_6O	99.7%AR	Wuxi Yasheng Chemical Co., Ltd.

Urea	CH_4N_2O	AR, 99%	Shanghai Yuanye Biotechnology Co., Ltd.
Deionized water	H_2O	—	Nanjing Wanqing Chemical Glass Instrument Co., Ltd.
Nitric acid	HNO_3	68% AR	Sinopharm Chemical Reagent Co., Ltd.
$Fe(NO_3)_3\cdot 9H_2O$	$Fe(NO_3)_3\cdot 9H_2O$	99.99%	Aladdin
Ammonium dihydrogen phosphate	$NH_4H_2PO_4$	AR	Sinopharm Chemical Reagent Co., Ltd.
N, N-Dimethylformamide	C_3H_7NO	AR	Sinopharm Chemical Reagent Co., Ltd.
Molybdenum oxide	MoO_3	AR, 99.5%	Macklin
H-SiO_2 precipitation	SiO_2	—	University of Zaragoza
D-SiO_2 precipitation	SiO_2	—	University of Zaragoza

2.2 Experimental instruments

The basic instruments used in this experiment are shown in Table 2.2.

Table 2.2 Details of the instruments required for the experiment.

Equipment Name	Model Specifications	Manufacturer
Magnetic stirrer	HJ-4AS	Changzhou Guoyu Instrument Manufacturing Co., Ltd.
Magnetic stirring heating mantle	WZNCLT000250	Nanjing Wener Instrument
Water bath	HH-S1	Jiangsu Jinyi Instrument Technology Co., Ltd.

Electronic balance	BS224S	Sartorius Scientific Instruments (Beijing) Co., Ltd.
Electric constant temperature vacuum drying oven	DZF-6050 6051	Shanghai Yiheng Scientific Instrument Co., Ltd.
Ethanol supercritical drying device	HA400-50-012	Jiangsu Huaan Scientific Research Instrument Co., Ltd.
High temperature box resistance furnace	SXL-1700	Hefei Kejing Material Technology Co., Ltd.
Vacuum high temperature tube furnace	MTIGSL1600X	Hefei Kejing Material Technology Co., Ltd.

2.3 Preparation of candidate catalyst materials

2.3.1 Preparation of SiO_2 aerogel material

With TEOS as the silicon source, deionized water as the hydrolytic agent, nitric acid as the catalyst, and ethanol as the solvent, SA was obtained by heating reflux method and sol-gel process under high temperature and pressure through ethanol supercritical drying technique.

Preparation of sol: Mix deionized water, ethanol, and nitric acid were mixed in a volume ratio of 60:40:1 to obtain an acidic solution. A certain amount of TEOS was dissolved in 6 mL ethanol to stir evenly at room temperature, and 8 mL acidic solution was slowly added. Stirring continuously for 10 min and then stir at 50°C for heating and reflux for 30 min, which was recorded as solution A. A certain amount of urea was dissolved in the mixture of 10 mL deionized water and 24 mL ethanol to stir at room temperature for 30 min, which was recorded as solution B. Then, solution A was slowly added into solution B, and stirred at room temperature for 10 min, the mixed solution was removed and transferred into a heating reflux device for stirring, heating, and reflux at 80°C for a period of time until it become a viscous sol, then the composite sol was obtained.

Gel into spheres: The coagulation bath was heated to a certain temperature. After the temperature was stable, a dropper was used to take a certain amount of composite sol and slowly dropped into the coagulation bath. After a period of time, the sol dropped in the coagulation bath gradually formed spherical gel. The spherical gel was taken out and placed in the deionized water, and the deionized water was replaced many times to clean and remove the coagulation bath residue on the surface of the material. Then the cleaned spherical gel was put into the ethanol solution, aged at 50℃ and the ethanol solution was replaced regularly for solvent replacement, three times a day for 4 d, so that the solvent in the gel holes can be fully replaced. Then the spherical gel was taken out and subjected to ethanol supercritical drying treatment.

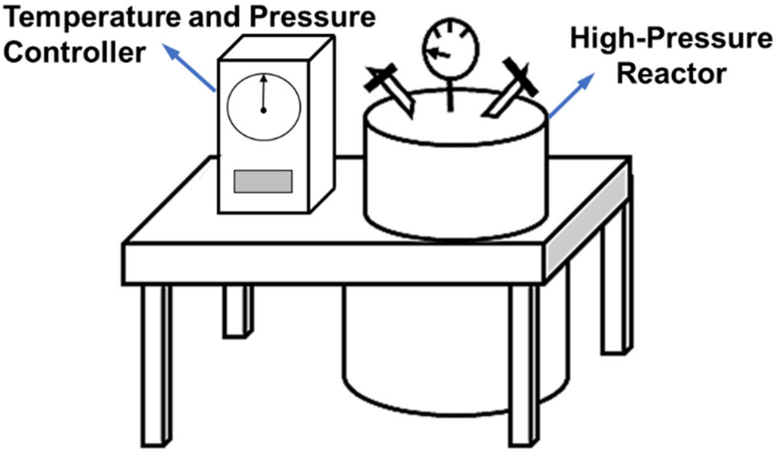

Fig. 2.1 Ethanol supercritical drying device.

The drying process of aerogel materials were mainly carried out by ethanol supercritical drying, and the device is shown in Fig. 2.1. The blocky/spherical gel was placed in a glass dish, and appropriate amount of ethanol was added to submerge the gel. The glass dish containing gel was carefully put into the ethanol supercritical reactor, and enough ethanol solution was poured into the reactor until all samples were submerged. The reactor cover was tightened to ensure that the reactor body was closed and the thermocouple was inserted. Then, N_2 was introduced to make the pressure in the reactor reach 4 MP, so as to prevent excessive volatilization of ethanol during the heating process at the initial stage of supercritical drying. After the pressure stabilized, the temperature was raised by 270℃ at a rate of 2.5 ℃/min within 2 h. During this time, the pressure inside the reactor raised to 10 MPa, and the venting was manually adjusted to stabilize the pressure at 10 MPa for 2 h. After the drying was completed, the vent valve was opened slightly and vent evenly for 30 min until the pressure in the reactor reaches normal pressure, and then the heating was closed. After the temperature of the reactor was reduced to room temperature, the reactor body was opened to take out the sample. Finally, the SiO_2 aerogel material was obtained.

2.3.2 Preparation of Fe-MoO_x/SiO_2 aerogel material

FMSA was obtained by ethanol supercritical drying under high temperature and pressure, heating reflux method, and the sol-gel process. Using TEOS as the silicon source, deionized water as the hydrolysis agent, nitric acid as the catalyst, ethanol as the solvent, $Fe(NO_3)_3 \cdot 9H_2O$ as the Fe source, and mixed with MoO_3.

Preparation of sol: Deionized water, ethanol, and nitric acid were mixed in a volume ratio of 60:40:1 to obtain an acidic solution. A certain amount of TEOS was dissolved in 6 mL ethanol, to stir evenly at room temperature, and 8 mL acidic solution was slowly added and stirred for 10 min, then heated and refluxed at 50 ℃ for 30 min, and recorded it as solution A. A certain amount of urea was dissolved in the mixture of 10 mL deionized water and 18 mL ethanol, and stirred at room temperature for 30 min to record as solution B. A certain amount of $Fe(NO_3)_3 \cdot 9H_2O$ and MoO_3 in a molar ratio of Fe: Mo=1:1 was dissolved in 6 mL anhydrous ethanol solution, a certain amount of N, N-dimethylformamide was also added, stirred evenly at room temperature, and recorded it as solution C. solution A was slowly added into solution C to mix and stir at room temperature for 30 min, then solution B was slowly added, and stirred at room temperature for 10 min, then the mixed solution was removed and transferred to a heating reflux device. The mixed solution was stirred and heated at a certain temperature and refluxed for a period of time to a viscous sol, thus obtaining a composite sol.

Gel into spheres: Polydimethylsiloxane (PDMS) was heated to 80℃. After the temperature was stable, a dropper was used to take a certain amount of composite sol and slowly dropped it into PDMS. After a period of time, the sol dropped in PDMS gradually become spherical gel. The spherical gel was taken out and placed in deionized water, and the deionized water was replaced for many times to clean the PDMS on the surface of the removed material. Put the cleaned spherical gel into ethanol solution and age it at 50℃. The ethanol solution was replaced regularly for solvent replacement, 3 times a day for 4 d. The spherical gel was taken out, and the spherical aerogel was obtained by ethanol supercritical drying. Then calcine at 650℃ for 6 h to obtain FMSA. The samples were named 7-FMSA (3 wt.% Fe_2O_3-4 wt.% MoO_3/SiO_2 aerogel), 13-FMSA (5 wt.% Fe_2O_3-8 wt.% MoO_3/SiO_2 aerogel), 19-FMSA (7 wt.% Fe_2O_3-12 wt.% MoO_3/SiO_2 aerogel) and 25-FMSA (9 wt.% Fe_2O_3-16 wt.% MoO_3/SiO_2 aerogel) depending on the Fe-MoO_x loading.

2.3.3 Preparation of $FePO_x/SiO_2$ aerogel material

With TEOS as the silicon source, deionized water as the hydrolytic agent, nitric acid as the catalyst, ethanol as the solvent, $Fe(NO_3)_3 \cdot 9H_2O$ as the Fe source, and $NH_4H_2PO_4$ as the P source, FPSA was obtained by heating reflux method and sol-gel process through ethanol supercritical drying under high temperature and pressure.

Preparation of sol: Deionized water, ethanol, and nitric acid were mixed in a volume ratio of 60:40:1 to obtain an acidic solution. A certain amount of TEOS was dissolved in 12 mL ethanol, to stir evenly at room temperature, and slowly 8 mL acidic solution was added. Stirred for 10 min, then the mixture was heated and refluxed at 50℃ for 30 min, and it was recorded as solution A. A certain amount of urea was dissolved in the mixture of 6 mL deionized water and 18 mL ethanol, and stirred at room temperature for 30 min to record as solution B. $Fe(NO_3)_3 \cdot 9H_2O$ and $NH_4H_2PO_4$ were dissolved with a molar ratio of Fe: P=1:1 in 8 mL deionized water, to stir evenly at room temperature, and recorded as solution C. Solution A was slowly added into solution C in the stirring process, to mix and stir at room temperature for 30 min, then solution B was slowly added, and stirred at room temperature for 10 min, then the mixed solution was removed and transferred to a heating reflux device. The mixed solution was stirred and heated at 80°C and refluxed for a period of time to a viscous sol, thus obtaining a composite sol.

Gel into spheres: The PDMS was heated to 80°C. After the temperature was stable, a dropper was used to take a certain amount of composite sol and slowly dropped it into the PDMS. After a period of time, the sol dropped in PDMS gradually become spherical gel. The spherical gel was taken out and placed in deionized water, and the deionized water was replaced for many times to clean the PDMS on the surface of the removed material. The cleaned spherical gel was put into ethanol solution and aged at 50°C. The ethanol solution was replaced regularly for solvent replacement, 3 times a day for 4 d. The spherical gel was taken out, and the spherical aerogel was obtained by ethanol supercritical drying. Then calcine at 650°C for 6 h to obtain FPSA. The samples were named 4-FPSA (4 wt.% $FePO_x/SiO_2$ aerogel), 8-FPSA (8 wt.%$FePO_x/SiO_2$ aerogel) and 16-FPSA (16 wt.%$FePO_x/SiO_2$ aerogel) depending on the $FePO_x$ loading.

2.3.4 Preparation of $FePO_x/SiO_2$ particle material

FPSP was obtained by using SiO_2 precipitation as the support, $Fe(NO_3)_3{\cdot}9H_2O$ as the Fe source, and $NH_4H_2PO_4$ as the P source through impregnation method, stirring heating, evaporation drying, and high-temperature calcination.

$Fe(NO_3)_3{\cdot}9H_2O$ and $NH_4H_2PO_4$ were mixed in an aqueous solution at a molar ratio of Fe/P=1/1, stirring evenly to obtain a mixed solution. SiO_2 precipitation was added into the mixed solution and stirred at room temperature for 5 h to mix evenly. Turn on the heating and evaporate the mixed solution in a continuous stirring state until a solid substance was obtained. Calcine the solid obtained from drying at 650°C for 6 h to obtain FPSP. The samples were named 2-FPSP (2 wt.% $FePO_x/SiO_2$ particle) and 4-FPSP (4 wt.%$FePO_x/SiO_2$ particle) depending on the $FePO_x$ loading.

2.4 Material composition and structural characterization methods

2.4.1 Density analysis

Apparent density of aerogel materials (ρ_m) was determined based on the mass volume method, and calculated by the ratio of the mass (m) of the sample to the volume (V_m) of the sample, as shown in formula (2-1):

$$\rho_m = m / V_m \tag{2-1}$$

ρ_m – Apparent density of materials (g/cm^3);

m – Mass of materials (g);

V_m – Volume of materials (cm^3)

2.4.2 Phase analysis

The crystal forms of aerogel materials were determined by Japanese Rigaku Ultimate IV type X-ray diffractometer (XRD). The tested sample was grinded into powder to eliminate the influence of crystal orientation. The Cu Kα radiation was used in the testing process, the X-ray tube voltage was 15kV, tube current was 40mA, scanning rate was 10 °/min, and range was set to $2\theta = 10° \sim 80°$. The results were analyzed using Search Match and Origin software.

2.4.3 Microstructure and morphology analysis

The microstructure and morphology of aerogel materials were observed and analyzed by Japanese JEOL JSM-7600F, JEOL JEM 2100F and German ZEISS Gemini SEM300. The EDS testing analyzer equipped with Japanese electronic JEOL JSM-7600F and JEOL JEM 2100F was used to analyze the element distribution in specific areas on the sample surface using X-ray emitted from the sample surface through scanning electron microscopy (SEM). In the ZEISS Gemini SEM 300 test, a small number of bulk samples were directly adhered to the conductive adhesive and sprayed with gold using a Quorum SC7620 sputtering coating instrument for 45 s at a rate of 10 mA. Subsequently, the sample morphology was captured using a SEM, and the accelerated voltage during the morphology capture was 3 kV.

2.4.4 Fourier transform infrared spectroscopy analysis

The Thermo Scientific Nicolet iS20 was used to test the aerogel material by Fourier transform infrared spectroscopy (FTIR) to obtain the information of the relative vibration and molecular rotation between the atoms in the material molecule, so as to understand the functional groups and chemical bond on the sample surface, and carry out qualitative and quantitative analysis on the composition of the sample. A small amount of sample and an appropriate amount of dried potassium bromide powder were taken in a dry environment and added them to a mortar. Then, grind thoroughly multiple times and press them into transparent thin sheets on a tablet press. The test was carried out by collecting the background first and then the infrared spectrum of the sample. The resolution parameter was 4 cm^{-1}, scanning number was 32 times, and the wavenumber range was 400-2000cm^{-1}.

2.4.5 Specific surface area and pore structure analysis

As a typical mesoporous material, the pore structure of SiO_2 based aerogel is an important aspect of investigation. The N_2 adsorption/desorption testing method is commonly used to obtain pore structure information, such as the adsorption/desorption curve, specific surface area, and pore size distribution of the sample. The V-Sorb 2800P specific surface area and pore size analyzer from Gold APP Instruments Co., Ltd. and the Quantachrome specific surface area and pore size analyzer from the United States were used for testing. Nitrogen was used as the adsorption gas, liquid nitrogen was used to create a low-temperature environment. The specific surface area was calculated using the Brunauer-Emmett-Teller (BET) equation. The pore size distribution curve was obtained by the Barret-Joyner-Helenda (BJH) method, and the pore size distribution was based on desorption data.

2.4.6 X-ray photoelectron spectroscopy analysis

X-ray photoelectron spectroscopy (XPS) can qualitatively and quantitatively analyze the surface elements of materials, and understand the atomic oxidation state, atomic charge, and functional groups of materials through chemical shifts. An ESCALAB 250Xi X-ray photoelectron spectrometer from ThermoFisher Scientific in the United States was used to record spectra and characterize the composition of the material. The voltage of the X-ray source was 16 kV, the current was 14.9 mA, and the beam spot diameter was 650 μm. The energy of the full spectrum was 100 eV, and the energy of the high-resolution spectrum of elements was 30 eV. To avoid instrument errors, charge calibration was carried out by the standard of C1s = 284.8 eV.

2.4.7 Hydrogen temperature programmed reduction test

Hydrogen temperature programmed reduction (H_2-TPR) is commonly used in the field of heterogeneous catalysis, and the reduction of catalytic materials at different temperatures can be observed. H_2-TPR testing was conducted using Micromeritics AutoChem II 2920 instrument and TCD detector to test the reducing activity of the material at different temperatures. 0.1 g of the test sample was put into the instrument, and high-purity nitrogen gas was injected, to raise the temperature to 200°C, and hold for 1 hour for pre-treatment. Cooling down to room temperature in a high-purity nitrogen atmosphere. The atmosphere was adjusted to 5% H_2/N_2, and then the temperature was raised to the target temperature at a rate of 10 °C/min. The consumption of H_2 during this process was recorded as a curve graph by a thermal conductivity detector (TCD).

2.5 Testing methods for reactors

2.5.1 Performance testing of fixed bed reactor

(1) Experimental device system

The experimental device used in the fixed bed reactor experimental system can be divided into three areas: the gas and liquid feed area, the experimental reaction area, and the product analysis area. The experimental device system was shown in Fig. 2.2.

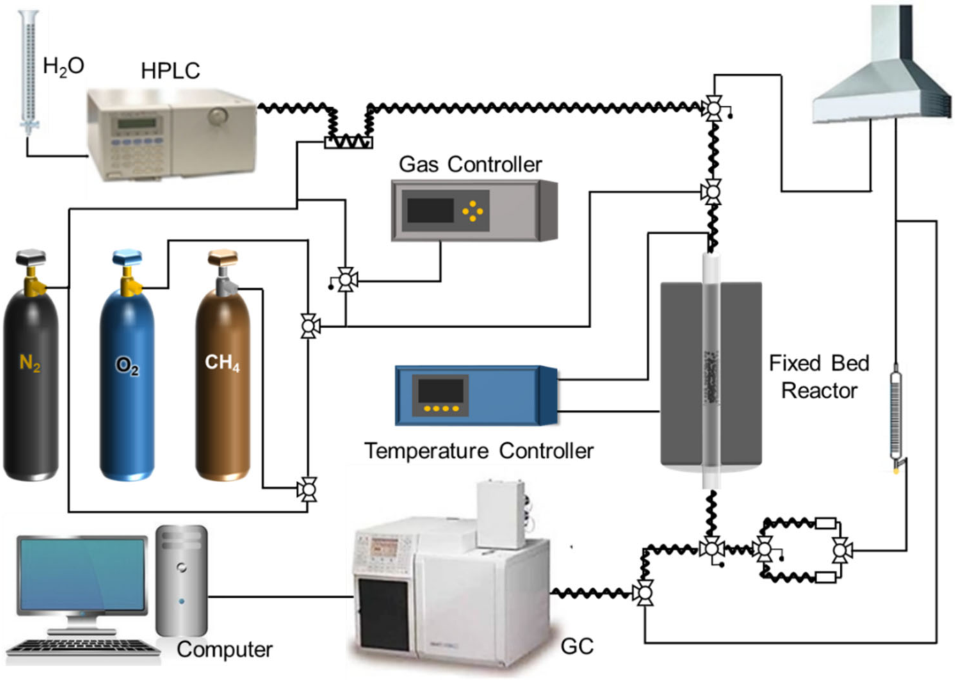

Fig. 2.2 Fixed bed reactor test experimental device system.

Feed zone: Equipped with three Brooks5850 TR type gas flow controllers to adjust the flow of N_2, O_2, and CH_4; A DINKO pump controls the amount and speed of introduced water.

Reaction zone: Composed of a controllable temperature electric furnace and a quartz tube fixed bed reactor. The catalyst was loaded into a fixed bed reactor, where the thermocouple contacted the catalyst bed in the reactor and was connected to the electric furnace to control the temperature environment of the catalytic reaction process. The reaction products were transported to the analytical instrument through insulated metal pipes.

Analysis zone: The non condensable products generated by the reaction were analyzed in a gas chromatograph (GC-CP3800 Varian with TCD detector). The condensed products were analyzed in a gas chromatograph coupled with a mass spectrometer (GCMS-QP 2010 Shimadzu).

(2) Experimental process steps

There were some differences in the experimental testing methods. One was whether the catalyst was pre-oxidized before the experiment began, and the other was whether water was introduced into the reaction airflow during the experiment.

If the catalyst required pre-oxidation reaction, it was necessary to conduct a pre-oxidation reaction experiment on the catalyst before the experiment began. Firstly, 6g of catalyst was placed into the fixed bed reactor and the inert gas N_2 was introduced into the reactor to create a constant protective atmosphere to prevent the catalyst from reacting with air during the heating process. The reaction temperature and heating rate (5~10 °C/min), and the controllable temperature electric furnace was heated up. After the pre-oxidation temperature was reached and stabilized, the flow rate of the incoming gas flow was adjusted to 100 mL/min, the gas flow composition was 10% O_2 and 90% N_2, and continued to supply the gas flow for 30 min to pre-oxidize the catalyst. After 30 min, stop introducing O_2, leaving only the inert gas N_2. Set the temperature to the subsequent catalytic reaction experiment temperature and adjust the temperature at a rate of 5~10 °C/min. If there was no need for pre-oxidation reaction of the catalyst, set the temperature of the controlled temperature furnace directly to the catalytic reaction temperature during the initial setting, and heated the controlled temperature electric furnace at a heating rate of 5~10 °C/min to the working temperature. After stabilization, proceeded with the catalytic reaction experiment directly.

In the catalytic reaction experiment without introducing water, the fixed bed reactor was heated to operating temperature at a heating rate of 5~10 °C/min in a protected atmosphere of inert gas N_2. When the temperature of the catalytic area transmitted by the thermocouple in the reaction bed reached the working temperature, prepared an ice bath with liquid nitrogen and salt, and placed the condenser in an ice bath environment for pre-cooling. When the temperature of the reactor and bed reached the working temperature and was stable, and the condenser had completed pre-cooling in the ice bath, the reaction flow CH_4 and O_2 were introduced in a certain proportion, and the introduction of inert gas N_2 was stopped. After the reaction experiment began, real-time online analysis was conducted on the gas at the outlet of the reactor to determine the composition of gaseous reaction products at different time points during the experiment process. At the same time, a bubble meter was used to monitor the flow rate at the outlet in real-time. The flow rate and corresponding gas product composition were tested and recorded at intervals of 15 min. After the experiment, the condenser was removed and its surface was carefully cleaned. Weighing the condenser together with the liquid and condensate collected inside and recorded it as W_1. After carefully collecting the products in the condenser, cleaned the condenser and weighed it again, recording it as W_2. The difference between W_1 and W_2 was the mass of the product collected in the condenser.

If water needs to be introduced into the reaction airflow during the experiment, it was necessary to turn on the heating instrument in advance before the experiment started, which was when the temperature of the controlled furnace was raised. After the temperature of the heating instrument stabilized, turned on the water introduction pump to introduce water into the heating instrument. It was worth noting that before the experiment began, it was necessary to ensure that the water vapor can maintain a stable speed and pass into the reactor together with the reaction gas.

(3) Calculation of experimental results

The main calculation components in the experimental results included the conversion of CH_4 and O_2, the selectivity and yield of HCHO. The results related to conversion and selectivity were calculated based on the results of online monitoring of gas products and the identification and quantification of products in the condenser. The calculation of yield was obtained by multiplying the CH_4 conversion and the average selectivity of HCHO.

The calculation formula for the conversion of CH_4.

$$\chi_{CH_4} = \frac{nCH_2O + nCO_2 + nHCHO + 2nEtOH + nCO + nHCHO(liq) + 2nEtOH(liq) + nCH_2O(liq)}{nCH_4\ \ totals}$$

$$n_{CH_4}\ \ totals = \frac{nCH_4}{min} \bullet \text{ experiment time}$$

The calculation formula for HCHO selectivity.

$$S_{CH_4 \rightarrow HCHO} = \frac{nHCHO + nHCHO(liq)}{nCO_2 + nCO + nCH_2O + 2nEtOH + nCH_2O(liq) + 2nEtOH(liq)}$$

The calculation formula for HCHO yield.

$$Y_{CH_4 \rightarrow HCHO} = S_{CH_4 \rightarrow HCHO} \bullet \chi_{CH_4}$$

2.5.2 Performance testing of conventional fluidized bed reactor

For FBR, determining the appropriate reaction gas flow rate is an important step in FBR experiments. Firstly, it was necessary to determine the U_{mf} and set the flow rate for the FBR catalytic experiment with reference to U_{mf}.

(1) Calculation method of U_{mf}

Fluidization is the process of a small-sized (<1 cm) solid reaching a fluid like state through contact with a gas or liquid. This fluid like state is characterized by the ability of the bed surface to remain horizontal even when the container is tilted. If a hole is made in the wall of the container, the solid will flow out. If two fluidized beds are connected, the solid can reach the same horizontal plane in both fluidized beds. When a fluid passes through a fine-grained bed, there will be different situations with the surface passing speed of the gas. When the speed is zero, the particles remain static, which is the fixed bed. Increasing the flow rate (u_0) to a point where particles begin to move due to the upward flow of gas (or liquid), and at this point, the bed is at U_{mf}.

Continuing to increase the flow rate on the basis of U_{mf}, the bed begins to produce bubbles, and the stirring and movement of solid particles increase. When the entire bed is in motion, it is called a fully fluidized state.

The device used to test U_{mf} was a quartz tube. The top of the tube was opened, and there was a porous plate at the bottom that allows gas to pass through while also preventing the descent of solid particles. The airflow can be adjusted by turning the valve. A pressure measuring instrument can measure the pressure loss experienced by gas passing through the bed.

To determine U_{mf}, the initial bed should be in a loose state. Therefore, the air stream is opened to fluidize the bed and then the valve is gradually closed while measuring the pressure drop in the bed. The surface velocity of the gas at each flow rate can be calculated from the known cross section of the tube.

The determination of U_{mf} is based on the Ergun equation, and the gas pressure loss passing through the particle bed is given by the following expression:

$$\frac{\Delta P}{L} = 150\frac{(1-\varepsilon)^2 \mu u_0}{\varepsilon^3 (\phi_S d_P)^2} + 1.75\frac{1-\varepsilon}{\varepsilon^3}\frac{u_0^2 \rho_s}{\phi_S d_P} \qquad (1)$$

ΔP = Pressure loss of gas in the bed

L = Bed length

ε = Porosity of the bed (fraction of gaps)

Φ = Sphericity of particles

d_p = Particle size

ρ_s = Particle density

Rep = dp u_0 ρ_s / μ

u_0 = Surface velocity of gas

As u_0 increases, ΔP will reach its maximum value. With a slight increase in apparent gas velocity, the bed layer "fractures", meaning that the porosity changes from ε_f Increase to ε_{mf}, causing ΔP decreases (Fig. 2.3).

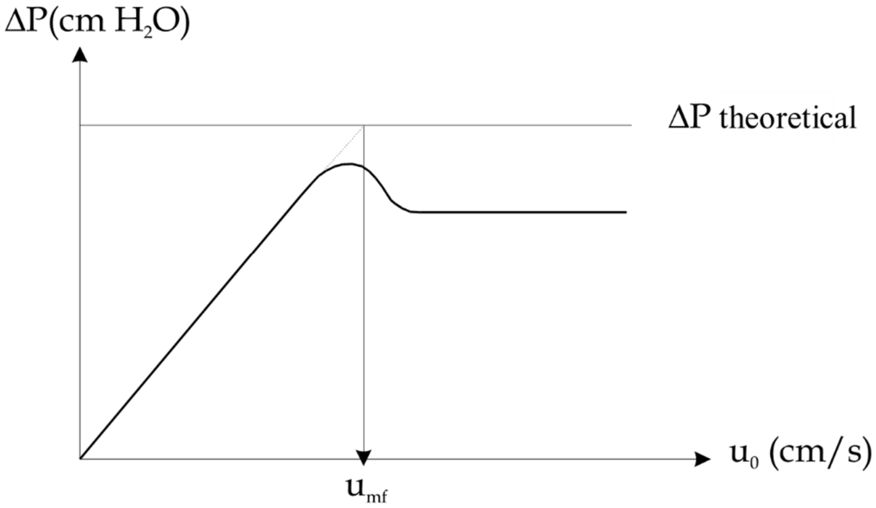

Fig. 2.3 Change curve of pressure loss with flow rate.

In the ΔP versus u_0 plots of Fig. 2.3, U_{mf} is defined as the flow rate at the intersection of the ΔP-u0 line (obtained when the fixed bed is initially loosened) and the given maximum theoretical pressure loss line in the bed. The formula is as follows：

$$\Delta P \ theory \ (\text{cm } H_2O) = \frac{W(g)}{S(cm^2)} \quad (2)$$

W(g)= Weight of solids in the bed(g)

S(cm^2)= Bed cross section

For porosity calculations, one starts with easily measurable magnitudes. Therefore, the weight (W) of solids contained in the bed is:

$$W = SL(1-\varepsilon)\rho_s \quad (3)$$

S (cm^2) = Cross section of the bed

L (cm) = Bed length

ρ_s (g/cm^3) = Particle density

ε= Bed porosity

Since the mass of solids does not change in the bed whether it is a fixed bed or a fluidized bed, therefore:

$$SL_1\,(1-\varepsilon_1)\rho_S = SL_2\,(1-\varepsilon_2)\,\rho_S \qquad (4)$$

Subscripts 1 and 2 mean loose and fixed states, respectively. From Equation 4 we get:

$$\varepsilon_2 = 1 - \frac{L_1}{L_2}(1-\varepsilon_1) \qquad (5)$$

On the other hand, according to the Ergun equation for the laminar flow regime, the pressure loss per unit length of the bed is given by:

$$\frac{\Delta P}{L} = 150\frac{(1-\varepsilon)^2\mu u_0}{\varepsilon^3(\phi_S d_P)^2} \qquad (6)$$

For loose and fixed states:

$$\frac{(1-\varepsilon_1)^2}{\varepsilon_1^3} = \frac{\Delta P_1}{L_1}\frac{(\phi_S d_P)^2}{\mu u_0}\frac{1}{150} \qquad (7)$$

$$\frac{(1-\varepsilon_2)^2}{\varepsilon_2^3} = \frac{\Delta P_2}{L_2}\frac{(\phi_S d_P)^2}{\mu u_0}\frac{1}{150} \qquad (8)$$

Equation 7 and Equation 8 are divided:

$$\frac{(1-\varepsilon_1)^2}{(1-\varepsilon_2)^2}\frac{\varepsilon_2^3}{\varepsilon_1^3} = \frac{\Delta P_1}{\Delta P_2}\frac{L_2}{L_1} \qquad (9)$$

Substituting Equation 5 into Equation 9 and clearing:

$$\varepsilon_1 = \frac{1-\dfrac{L_1}{L_2}}{\sqrt[3]{\dfrac{\Delta P_1}{\Delta P_2}\dfrac{L_1}{L_2}} - \dfrac{L_1}{L_2}} \qquad (10)$$

Using this equation, we can calculate ε_1. When ε_1 is known, the calculation of ε_2 can directly use Equation 5. The density ρ_S of the solid is calculated by applying Equation 3 with sphericity Φ_s and Equation 6.

To calculate ΔP_1 and ΔP_2, once the flow rate data and the pressure loss in the bed (ΔP) are obtained, plot ΔP-u_0. At the same fluid velocity, ΔP is higher in a fixed bed than in a loose bed due to the smaller porosity in the fixed bed.

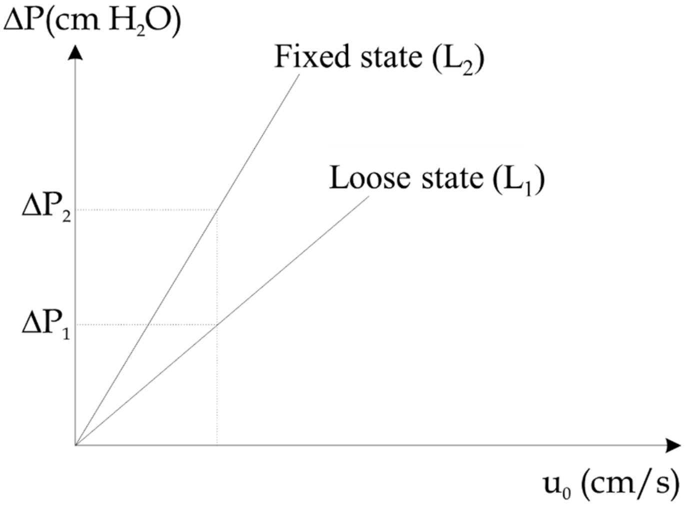

Fig. 2.4 Pressure loss curve of loose bed (L_1) and fixed bed (L_2) with flow rate

For the same u_0 value, measure ΔP_1 and ΔP_2. L_1 and L_2 can also be measured directly from the system.

Use equation 10 and equation 5 to calculate ε_1 and ε_2. Afterwards, the density of the solid can be calculated.

$$\rho_S = \frac{W}{SL_1(1-\varepsilon_1)} \tag{11}$$

The density of the bed can also be calculated using the following methods (ρ_1 fluidized bed and ρ_2 fixed bed):

$$\rho_1 = \frac{W}{SL_1} \qquad \rho_2 = \frac{W}{SL_2} \tag{12}$$

The sphericity is given by the Ergun equation:

$$\phi_S = \frac{1-\varepsilon}{d_P}\sqrt{150\frac{L}{\Delta P}\frac{\mu \cdot u_0}{\varepsilon^3}} \tag{13}$$

The theoretical calculation of U_{mf} can use the following two expressions:

$$u_{mf} = \frac{(\phi \cdot d_p)^2 \cdot (\rho_s - \rho) \cdot g}{1650 \cdot \mu} \tag{14}$$

The ρ is the fluid density.

$$A_r = \frac{\rho \cdot (\rho_s - \rho) \cdot g \cdot d_p^3}{\mu^2} \tag{15}$$

$$\mathrm{Re}_{mf} = \sqrt{27.2^2 + 0.0408 \cdot A_r} - 27.2 \tag{16}$$

$$u_{mf} = \frac{\mathrm{Re}_{mf} \cdot \mu}{d_p \cdot \rho} \tag{17}$$

In summary, after obtaining the values of ΔP and u_0:

1. Calculating the U_{mf} of a given solid sample from Fig. 7.1.

2. Use the relational diagram Fig. 7.2 of ΔP versus u_0 for the sparse and fixed beds to calculate the porosity, solid particle density, bulk density, and sphericity of loose and fixed beds.

3. Calculating U_{mf} by theoretical calculation equations. Comparing the experimental U_{mf} with the theoretical predicted U_{mf}.

(2) Experimental methods for catalytic reactions in conventional FBR

The conventional FBR was a 2.66 cm diameter quartz tube into which 7.5 g of catalyst was placed. The reaction gas was introduced from the bottom to come into contact with the catalyst and undergo catalytic reactions. The reaction products, unconverted reactants, and possibly introduced inert dilution gases were discharged from the upper outlet of the reactor. An example of a conventional fluidized bed reactor was shown in Fig. 2.5.

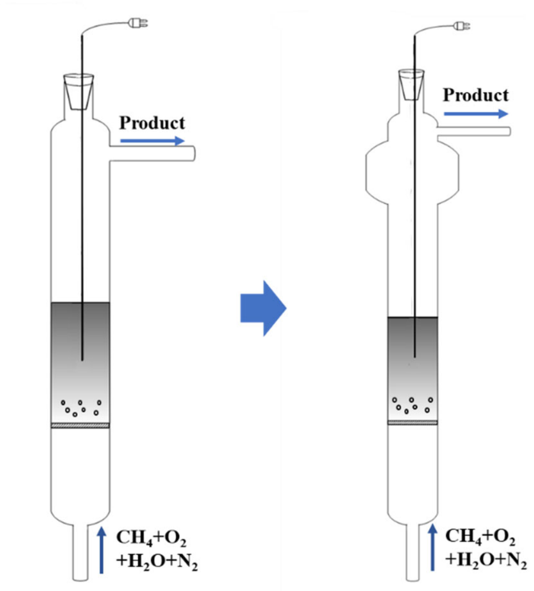

Fig. 2.5. Conventional fluidized bed reactor (FBR).

The previous section introduced the calculation method of U_{mf}. By setting an appropriate reaction gas flow rate based on U_{mf}, the catalytic reaction experiment can begin. The experimental process was similar to the catalytic reaction experiment in a fixed bed reactor. The difference is that in a fixed bed reactor, the gases involved in the reaction are passed in from the upper part of the reactor and the reaction products, unconverted reactants and possibly introduced inert dilution gases flow out from the lower part, whereas in a FBR, the gases are passed in from the lower part and exit from the upper part (and the gas velocity is higher than U_{mf}). The calculation of experimental results, including the conversion of CH_4 and O_2, as well as the selectivity and yield of HCHO, was of the same as for fixed bed reactor.

2.5.3 Performance testing of a two-zone fluidized bed reactor

The performance test parameters of the TZFBR were similar to those of the FBR, while there are significant differences in terms of reactor construction. Compared to conventional FBR, the biggest feature of a TZFBR was the presence of separate two zones in the same container. In the two zones, the catalyst reacted with gaseous hydrocarbon combination reaction to produce reduction, and then reacted with oxygen containing gas to be oxidized. Catalysts can store oxygen and also serve as supports for supplying oxygen.

The structure of TZFBR was shown in Fig. 2.6, where oxygen was mixed with possible inert gases and fed into the lower part of the reactor. The hydrocarbons that should be oxidized, such as CH_4 in this work, were fed into the middle point of the bed. In the lower zone (regeneration zone), the catalyst reacted with gas-phase oxygen and was oxidized. During the fluidization process of the catalyst, a large amount of gas-phase oxygen was consumed. When the airflow reached the introduction point of CH_4, the concentration of gas-phase oxygen decreased, which can cause CH_4 reactions to occur in an environment with less gas-phase oxygen.

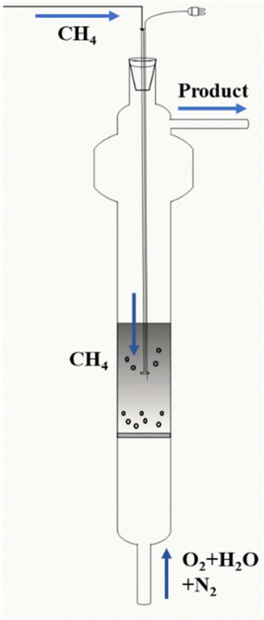

Fig. 2.6 Two-zone fluidized bed reactor (TZFBR).

In the upper zone (reaction zone), the catalyst carried a large amount of lattice oxygen, and CH_4 were oxidized by lattice oxygen in the catalyst. The reaction products, unconverted reactants, and Inert dilution gases left the bed together and exited from the outlet. The good solid circulation of the fluidized bed provided good solid transport between the two zones. There were two key issues in the experiment of TZFBR. On the one hand, the gas phase oxygen in the lower zone (regeneration zone) of the reactor needed to be consumed as much as possible; On the other hand, it was necessary to avoid back mixing of gases, especially hydrocarbons. Therefore, determining the gas flow rate in the TZFBR catalytic experiment was a crucial step.

Chapter 3 Process and characterization of SA preparation

SiO_2 aerogel material exhibits a wide range of application values in insulation, adsorption, catalysis, and drug delivery fields due to its low density, high porosity, and high specific surface area[84, 85]. As a candidate catalyst material support, SiO_2 aerogel may obtain catalyst materials with larger specific surface area and stronger dispersion of active components. This chapter introduces the process control and basic characterization of SiO_2 aerogel materials as candidate catalyst material supports during preparation. SiO_2 aerogel materials were prepared using tetraethyl orthosilicate (TEOS) as the silicon source through heating reflux, sol-gel method, and ethanol supercritical drying process. The addition amount of each component, heating reflux time and temperature, and other parameters during the preparation process were controlled to investigate the influence of the preparation process on the material structure. The influence of the type and temperature of the coagulation bath on the effectiveness of dropping during the sol dropping process was studied. The more excellent preparation process was selected to obtain SiO_2 aerogel materials with a more complete structure and more uniform composition. The micro-morphology, phase, specific surface area, and pore structure of SiO_2 aerogel materials were tested and analyzed for overall structural and compositional characterization.

3.1 Process of SiO_2 aerogel preparation

3.1.1 SiO_2 sol-gel process

(1) The influence of addition of urea on sol-gel reaction

Urea, as an organic compound, can hydrolyze into carbon dioxide and ammonia at a certain temperature. During the heating reflux experiment stage of SiO_2 sol preparation, urea can act as a base catalyst to accelerate gelation by increasing the pH value of the mixed solution [86]. Different amounts of urea added directly affect the time required for heating reflux during sol preparation. The influence of urea addition (TEOS: urea =

8:1, 4:1, 2:1 mL/g) on the experimental process was investigated.

Table 3.1 The influence of urea on the experimental process.

Item	TEOS/ Urea (mL/g)	Heating and reflux temperature (°C)	Gelation time	Note
3-1-1	8/1	80	2 h 30 min	Uncertainty
3-1-2	8/1	79	2 h 55 min	start to gel
3-1-3	4/1	79	1 h 25 min	start to gel
3-1-4	2/1	79	40 min	start to gel

When the urea-to-TEOS ratio was set to 8:1 mL/g, the heating reflux temperature was set to 80°C, and the precursor was continuously stirred during the heating reflux process to form a mixed sol. However, during the experiment, it was difficult to reach 80°C, and boiling occurred, indicating that 80°C was close to the sol boiling point. When the heating reflux time was 2 h 30 min, the sol began to gel, and the time was recorded in experiment 3-1-1. The heating reflux device was immediately turned off, and the semi-solid gel was taken out. Based on the experimental experience, the heating reflux temperature was adjusted to 79°C and experiment 3-1-2 was carried out. Some small bubbles appeared during the experiment, but no boiling occurred. When the heating reflux time was 2 h 55 min, the sol began to gel, and the time was recorded. The heating reflux device was immediately turned off, and the semi-solid gel was taken out. According to experiments 3-1-1 and 3-1-2, when the urea-to-TEOS ratio was 8:1 mL/g, the heating reflux temperature should be set to 79°C, and the gelation time was 2 h 55 min. Then, the ratio of TEOS to urea was adjusted to 4:1, and the heating reflux time remained at 79°C for experiment 3-1-3. The experimental process was similar to that of experiment 3-1-2, with no boiling occurring and only some bubbles appearing. When the heating reflux time was 1 h 25 min, gelation occurred and the time was recorded. The heating reflux device was turned off, and the gel was taken out. Experiment 3-1-4 was conducted to examine the TEOS-to-urea ratio of 2:1, and gelation occurred when the heating reflux time was 40 min. The time was recorded, and the heating reflux device was turned off. This group of experiments showed that as the amount of urea added increased, the gelation time gradually decreased. This was because the higher the amount of urea added as a basic catalyst, the faster the pH value of the heating process increased, which accelerated the gelation of the SiO_2 sol. In order to avoid adding too little or too much urea and causing the heating reflux time or gelation time to be too long or too short, respectively, we chose the ratio of TEOS to urea of 8:1 mL/g as the experimental formula for subsequent experiments.

(2) The influence of TEOS addition on sol-gel reaction

In this group of experiments, the amount of other reagents such as urea (2 g) was fixed to investigate the influence of TEOS addition on the sol-gel process and aerogel density. 4 mL, 6 mL, 8 mL, 10 mL, and 12 mL of TEOS were added to the initial mixed solution, respectively. The gels were obtained after refluxing at 79°C for 1 h 5 min, followed by aging and drying to obtain SiO_2 aerogel materials. The experimental process and results are shown in Table 3.2. As the amount of TEOS added increased, the sol viscosity increased in the later stage of heating and refluxing. When the amount of TEOS added was 4 mL, the sol had a relatively large fluidity after heating and refluxing for 1 h 5 min; as the amount of TEOS added increased, when the amount of TEOS added was 12 mL, the sol was relatively viscous at the end of heating and refluxing. After obtaining the silica sol-gel, solvent replacement, aging, and drying were carried out, and the density of the aerogel material was measured by the mass-volume method. It can be seen from the data in Table 3.2 that the greater the amount of TEOS added, the higher the density of the obtained samples. This is because the increase in the amount of TEOS directly leads to an increase in the amount of SiO_2 in the sample, resulting in a higher density and an increase in the density of the sample. Considering the completeness of the sample structure, the density of the sample, and the experimental cost, 8 mL of TEOS was selected as the formulation parameter for subsequent experiments.

Table 3.2 The influence of TEOS addition amount on sol-gel reaction.

Item	TEOS (mL)	Density (g/cm^3)
3-1-5	4	0.0996
3-1-6	6	0.1234
3-1-7	8	0.1638
3-1-8	10	0.1846
3-1-9	12	0.2147

(3) The influence of heating and refluxing time on sol-gel reaction.

During the preparation process, the duration of sol-gel process directly and the density and internal structure crosslinking of the material were impacted by the heating and reflux time. In this experiment, the amount of TEOS (8 mL) and urea (2 g) were fixed, and 79°C was used as the heating and reflux temperature to investigate the influence of heating and reflux time on the sol-gel process.

Table 3.3 The influence of heating and reflux time on sol-gel process.

Item	Heat reflux time	Sol consistency	Density (g/cm^3)
3-1-10	55 min	Slightly low	0.1850
3-1-11	1 h 05 min	Low	0.1807
3-1-12	1 h 15 min	High	0.1781
3-1-13	1 h 25 min	Very high	0.1752

During the experiment, samples were taken starting at 55 min of heating reflux time, and were quantitatively sampled every 10 min. At the initial sampling, the sol presented a highly fluid state. As the heating reflux time increased, the sol gradually became viscous. When the heating reflux time reached 1 h 25 min, the sol became very viscous. After the sol-gel was taken out, the samples underwent solvent substitution, aging, and drying treatments. Comparing the dried aerogels, it was found that the samples taken out earlier showed more severe shrinkage during the later stages of gelation and aging. This was mainly due to insufficient internal crosslinking of the SiO_2 sol taken out earlier, and crosslinking reactions continued to occur in the material during the subsequent gelation and aging processes, leading to the shrinkage of the samples. The density data obtained from the tests in Table 3.3 show that the density decreases as the heating reflux time increases, which is consistent with the above phenomena. Taking out the sol-gel too early will cause the structure of the sol-gel material to shrink and increase in density, leading to an increase in material density. Since we subsequently used the SiO_2 sol to form spherical gels by dropping, it was necessary to ensure that the SiO_2 sol-gel as quickly as possible in the coagulating bath to avoid the stacking and merging of SiO_2 sol at the bottom of the coagulating bath, which would prevent the formation of spheres. Therefore, it was necessary for the sol to approach the gelation point before dropping. The sample with a heating reflux time of 1 h 20 min was choose as the sol for the dropping experiment.

3.1.2 Types of coagulating bath

The process of transforming SiO_2 sol into spherical gel involves the steps of sol dropping and gel forming. The " Ball drop" method follows the characteristic of sol and coagulating bath being incompatible and is simple and easy to operate. The sol is dripped into the coagulating bath, and the spherical sol gradually gels during the falling process and after sinking to the bottom of the coagulating bath, and then further forms to obtain a spherical gel. In the experiment, the type of coagulating bath can affect the state of the sol after dropping, thereby affecting the sol-gel process. Here, we investigated the performance of two different coagulating baths, rapeseed oil and polydimethylsiloxane (PDMS), in the dropping sphere process.

Firstly, the rapeseed oil was poured into a beaker and then placed in a water bath. The temperature was heat to 80°C and wait for it to stabilize. Take out the solution that has undergone the heating and reflux process, add it dropwise to the rapeseed oil coagulating bath using a dropper. The experimental process is shown in Fig. 3.1.

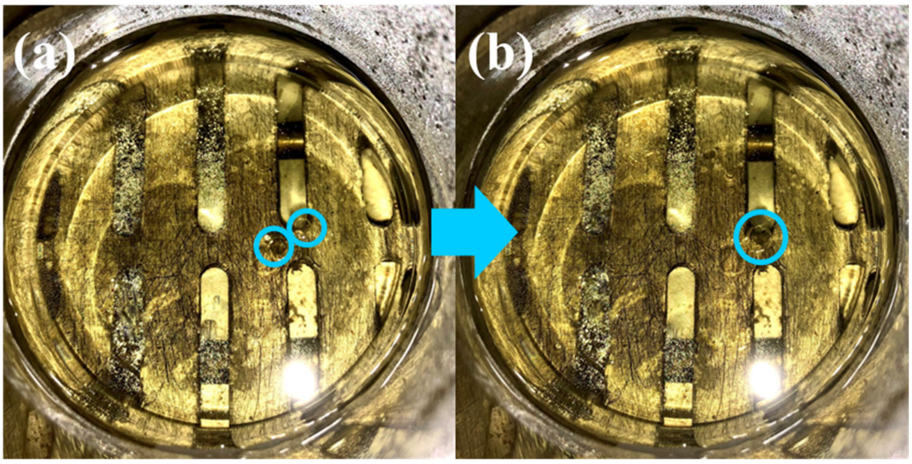

Fig. 3.1 SiO_2 sols spherical in rapeseed oil at 80°C.

Upon dropping the sol into the rapeseed oil, the SiO_2 sol and rapeseed oil were immiscible, causing the sol droplets to aggregate and float on the surface of the rapeseed oil, as shown in Fig. 3.1. As observed during the standing process, the sol droplets gradually approached and aggregated into a larger sol droplet but remained floating on the surface of the rapeseed oil. After further standing, the sol droplets did not form complete spherical sol droplets nor show a tendency to sink.

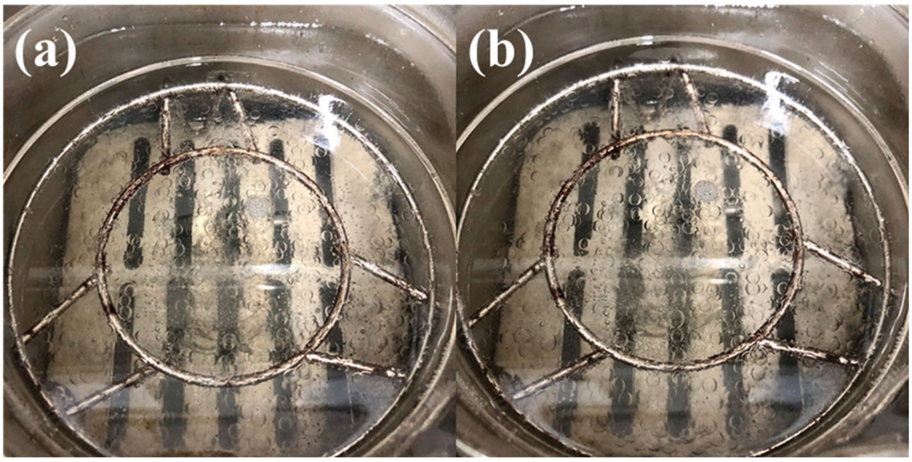

Fig. 3.2 SiO_2 sols spherical in PDMS at 80°C.

Subsequently, the dropping sphere in another type of coagulating bath, PDMS, was examined. PDMS was poured into a beaker and placed in a water bath. The temperature was raised to 80°C and allowed to stabilize. Using a dropper, SiO_2 sol, which had been subjected to a heating reflux process, was gradually added dropwise into the PDMS, and the state of the sol in the PDMS was observed, as shown in Fig. 3.2.

Upon initial contact of the SiO_2 sol with PDMS, the sol immediately formed into spherical shapes and began to slowly fall through the PDMS. As additional sol was added, the resulting spherical sols remained independent from each other and did not easily coalesce or collide. With continued heating of the PDMS, the heat flow caused the sol spheres to move up and down within the PDMS, and after approximately 3 min, they gradually sank to the bottom of the beaker. After all the sol had sunk to the bottom and formed into spherical gels, the mixture was left to stand for 10 min before carefully filtering out the PDMS. The resulting spherical gels were structurally complete and independent from each other. Thus, PDMS was chosen as the coagulating bath for subsequent experiments.

3.1.3 Temperature of the coagulation bath

The temperature of the coagulating bath is one of the important process parameters during the dropping sphere experiment. It not only determines the speed of sol-gel transition and the degree of gel shrinkage, but also affects the apparent size and internal structure of the resulting spherical aerogels. After confirming PDMS as the coagulating bath, we investigated the influence of coagulating bath temperature on the process of spherical gel formation.

After increasing the PDMS coagulating bath temperature to 60°C and stabilizing the temperature, the SiO_2 sol that was just taken out after heating reflux was added dropwise into the PDMS using a dropper, and the state of the sol in the PDMS was observed, as shown in Fig. 3.3. The figure shows that a small amount of sol was dropped into the PDMS and dispersed into spherical and relatively independent droplets. After a period of static observation, the spherical sol droplets began to aggregate and merge, and smaller droplets merged to form larger droplets. According to observations, gelation did not occur in a short period of time, and the larger sol droplets floated on the upper layer of the PDMS and did not move up and down with the thermal flow.

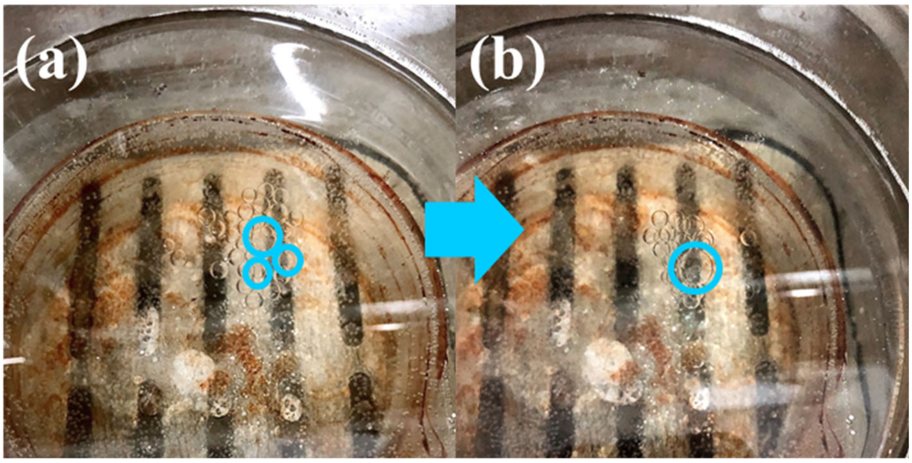

Fig. 3.3 SiO_2 sol dropping spheres in PDMS at 60°C.

As compared to the phenomena observed in the PDMS coagulating bath at 60°C, we investigated the influence of setting the PDMS coagulating bath temperature to 70°C. After the temperature stabilized, SiO_2 sol was dripped into the PDMS using a dropper, and the state of the sol in the PDMS was observed, as shown in Fig. 3.4.

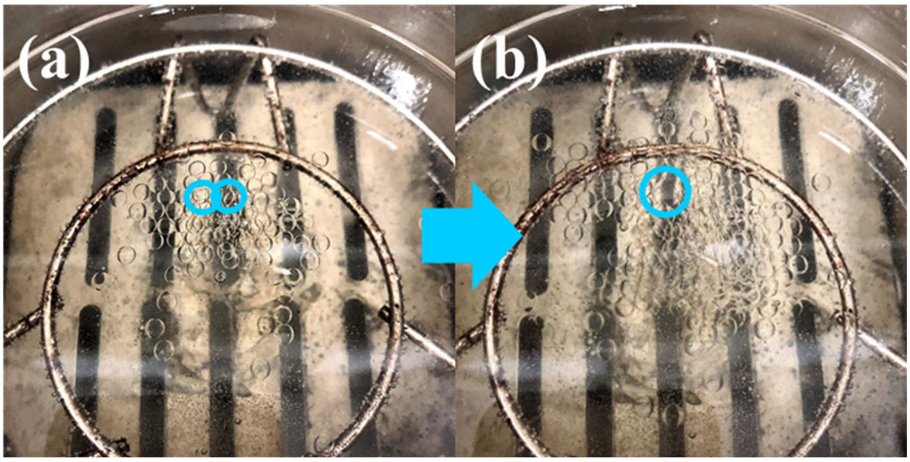

Fig. 3.4 SiO_2 sol dropping spheres in PDMS at 70°C.

Initially, the sol droplets were relatively independent in the PDMS. As more sol droplets were added, the spherical sol droplets did not disperse and move with the heat flow, but instead gathered below the surface of the PDMS. After a period of static time, some of the spherical sol droplets began to merge, and with increasing static time, the number of merged droplets gradually increased. However, compared with the PDMS coagulating bath at 60°C, the sol merging phenomenon was reduced in the coagulating bath at 70°C.

After increasing the PDMS coagulation bath temperature to 80°C and stabilizing it, the heated and refluxed SiO_2 sol was slowly dropped into the PDMS using a dropper, as shown in Fig. 3.5. The sol droplets were initially dispersed and independent in the PDMS, and moved up and down with the heat flow without agglomerating or merging into each other. After a period of time, they gradually settled to the bottom of the cup while simultaneously gelling in the PDMS. The settled materials were in a gel state and were mutually independent. After allowing all the materials to settle to the bottom of the cup and standing for 10 min, the spherical gel was separated from the PDMS using a filter, resulting in complete spherical gels. Subsequently, the influence of dropping sphere in 90°C PDMS curing bath was investigated, which was similar to that of dropping sphere in 80°C PDMS. The spherical gels were independent and structurally intact, but the resulting gels and dried aerogel samples had a higher shrinkage rate compared to those formed at lower temperatures.

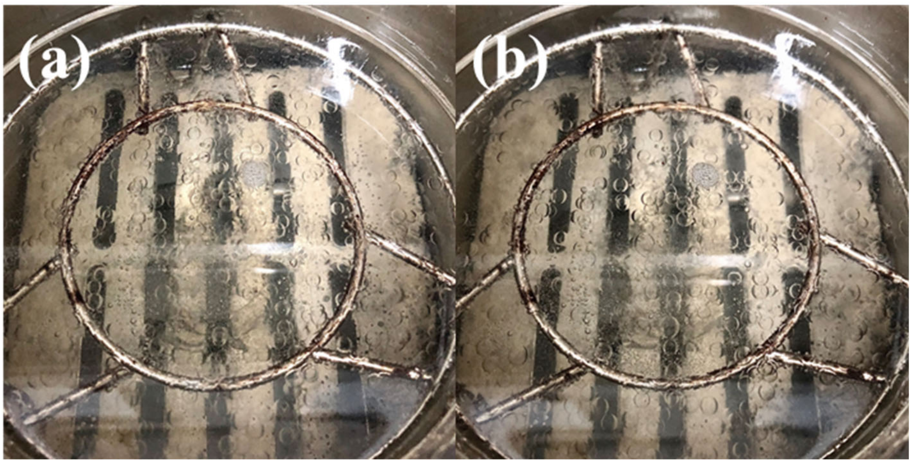

Fig. 3.5 SiO_2 sol dropping spheres in PDMS at 80°C.

In summary, the experiments in this section investigated the performance of dropping spheres in two different coagulation baths and at different PDMS coagulation bath temperatures. Based on the observed phenomena, it was found that dropping the spheres in PDMS was more favorable compared to rapeseed oil, with the ability to form spherical gels successfully. Spherical gels obtained by dropping spheres at a PDMS temperature of 80°C are structurally intact and independent of each other and are a more preferred dropping sphere process.

3.2 Characterization of the structure of SiO_2 aerogel materials

3.2.1 Microscopic morphology analysis

In order to observe and study the microstructure and morphology of SiO_2 aerogel materials, SEM analysis was conducted and tested for mapping and elemental distribution.

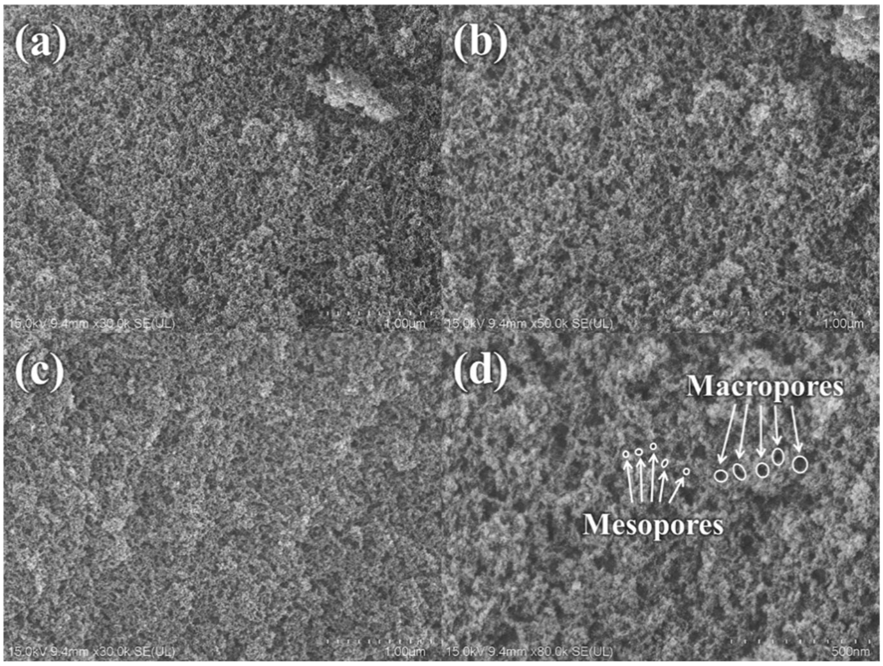

Fig. 3.6 SEM image of SiO_2 aerogel.

Fig. 3.6 shows the SEM images of SiO_2 aerogel material obtained by ethanol supercritical drying at different magnifications. The dried SiO_2 aerogel is a three-dimensional network structure material composed of SiO_2 particles, with various sizes of nano-scale pores distributed throughout the structure. Most of the pores are mesopores with diameters of 10-50 nm, and some macropores larger than 50 nm are also present. The overall pore structure is dominated by mesopores. The heating reflux step in the preparation process promotes solution dissolution and cross-linking, resulting in a relatively uniform material structure. The abundant pore structure and uniformly distributed SiO_2 particles provide the material with a large specific surface area. As a support material, it can provide a good dispersing bed for the active component of the catalyst, which is the outstanding advantage of SiO_2 aerogel material.

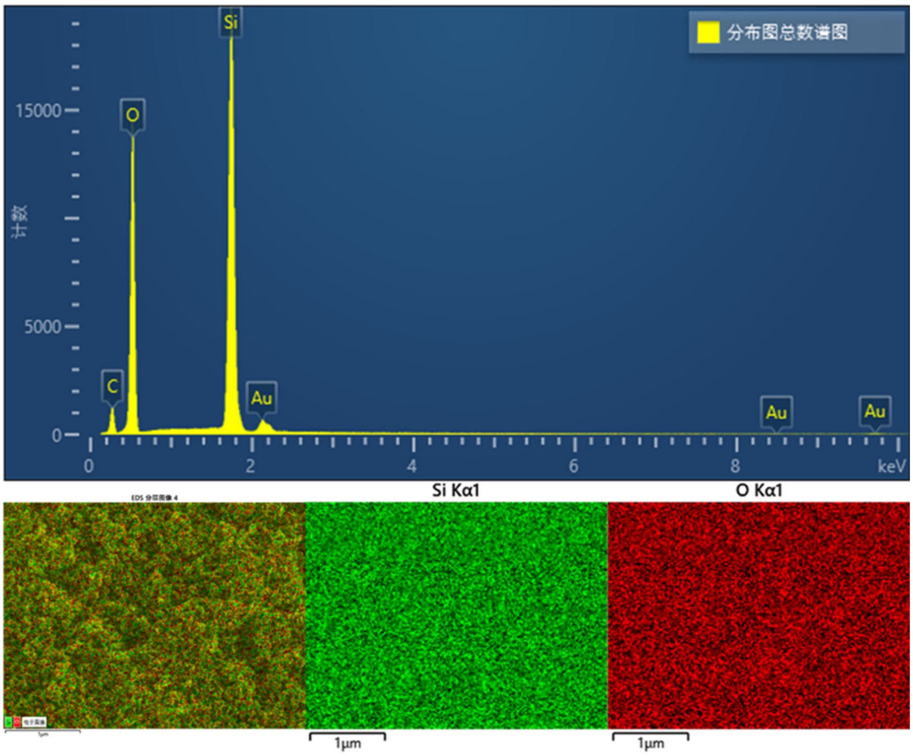

Fig. 3.7 Mapping and element distribution of SiO_2 aerogel.

In order to investigate the elemental distribution in SiO_2 aerogel materials, mapping and elemental distribution tests were conducted. Fig. 3.7 shows that Si and O constitute the vast majority of the elements detected on the surface of SiO_2 aerogel material, and some C atoms originate from the alkali catalyst urea added during the preparation process and its products from heating and decomposition during the ethanol supercritical high-temperature drying. The elemental distribution in the mapping showed that Si and O signals were evenly distributed over the area. As a catalyst material support, the SiO_2 aerogel material prepared by the method described in this thesis has a uniform elemental distribution, and has the potential to uniformly load active components, making it a promising candidate as a catalyst support.

3.2.2 XRD analysis

X-ray diffraction (XRD) was conducted to investigate the crystalline structure of SiO_2 aerogel, and the XRD pattern is shown in Fig. 3.8. The broad amorphous peak at 2θ of 20~30° corresponds to amorphous SiO_2[87]. This unique peak shape is due to the random arrangement of SiO_2 atoms or molecules in the amorphous material, which lacks the normal crystallographic symmetry and long-range periodic structure found in crystals, resulting in a disrupted diffraction signal and a glass-like appearance [88, 89]. Amorphous SiO_2 is typically prepared by high-temperature melting followed by rapid cooling or sol-gel methods, which is the process used in the preparation of the aerogel material in this study. Compared to other forms of SiO_2, amorphous SiO_2 has higher surface area and better catalytic properties, making it suitable as an excellent catalyst support.

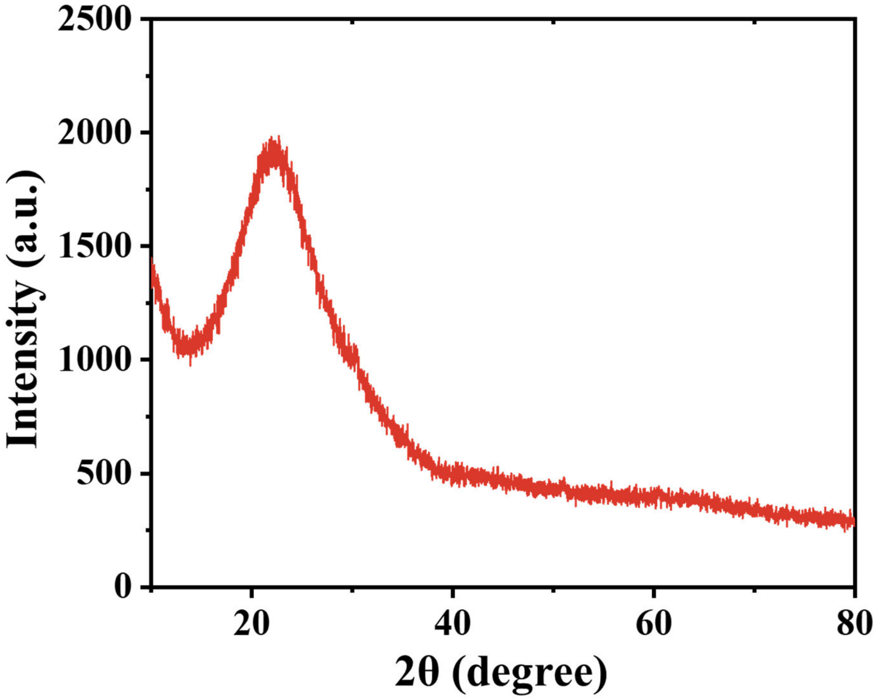

Fig. 3.8 XRD pattern of SiO_2 aerogel.

3.2.3 Specific surface area and pore structure analysis

As a catalyst support, the specific surface area and pore structure of a material are important characterization parameters, which are usually evaluated by the Brunauer-Emmett-Teller (BET) method based on N_2 adsorption-desorption isotherms. According to the classification of the International Union of Pure and Applied Chemistry (IUPAC), there are six main types of adsorption isotherm, as shown in Fig. 3.9 (a)[90]. Among them, Type IV and Type V exhibit hysteresis loops caused by capillary condensation and evaporation. Hysteresis loops are generated due to capillary condensation phenomena. As the adsorption volume increases with equilibrium pressure, the measured adsorption branches and the measured desorption branches when the pressure decreases do not coincide over a range of relative pressures and separate to form a ring. This phenomenon is widely observed in the isotherms of mesoporous solids. IUPAC has classified these hysteresis loops into four types, as shown in Fig. 3.9 (b)[90].

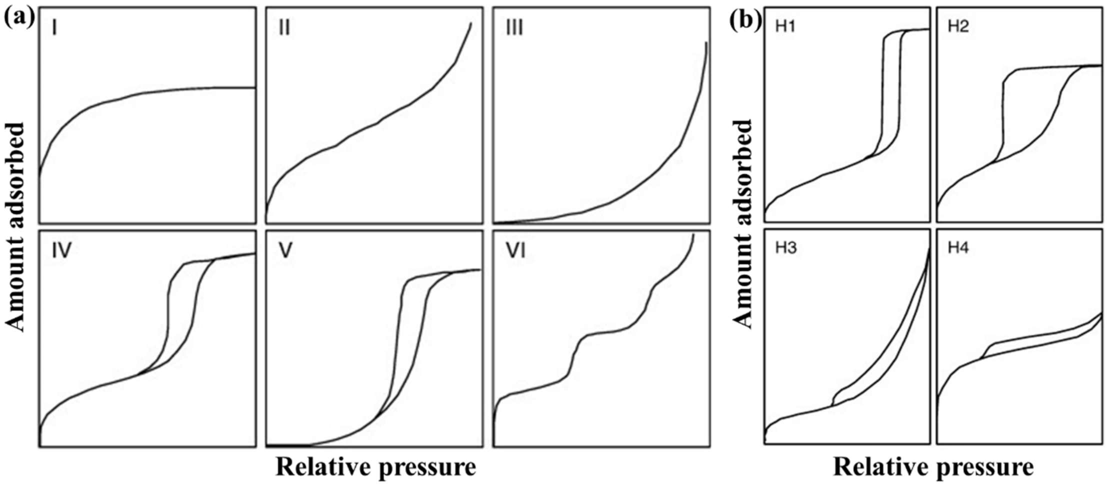

Fig. 3.9 (a) Isotherm type of N_2 adsorption-desorption and (b) adsorption isotherm type with desorption hysteresis behavior.[90]

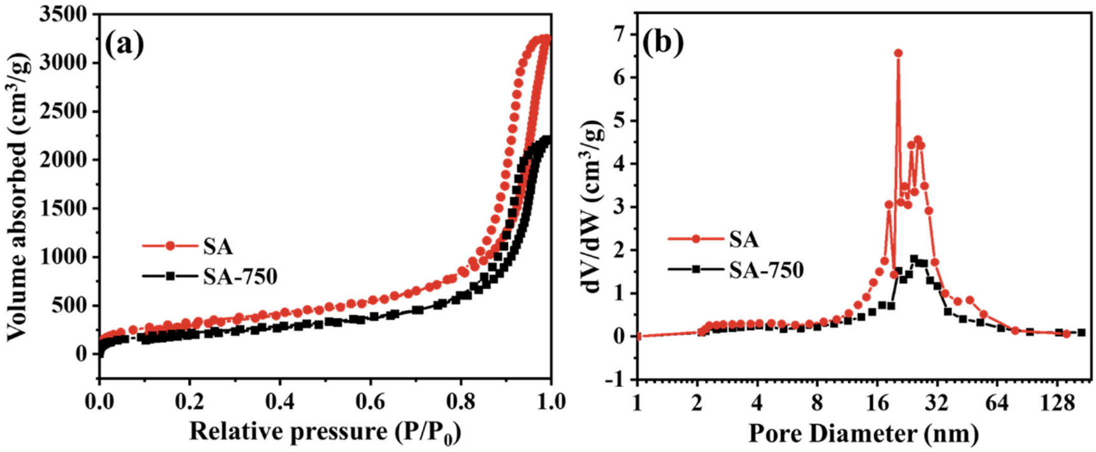

Fig. 3.10 (a) N_2 adsorption-desorption isotherm and (b) pore size distribution of SA and SA-750.

Table 3.4 Specific surface area and average pore diameter of SA and SA-750.

Sample	Specific surface area (m^2/g)	Average pore size (nm)
SA	1208.4	15.2
SA-750	810.4	15.1

As a mesoporous material, SiO_2 aerogel has a pore size distribution mainly within the mesoporous range. Fig. 3.10 shows the N_2 adsorption-desorption isotherms and pore size distribution curves of SiO_2 aerogel and SiO_2 aerogel treated at 750°C. The specific surface area and average pore size are shown in Table 3.4. As shown in Fig. 3.10 (a), the isotherms of both untreated and treated SiO_2 aerogel belong to the typical type IV, with an H1-type hysteresis loop, indicating that SiO_2 aerogel materials have a mesoporous structure with a narrow pore size distribution range, which is composed of spherical particles of relatively uniform size. It is consistent with the microstructure of SiO_2 aerogel observed in section 3.2.1. The specific surface area of untreated SiO_2 aerogel is 1208.4 m^2/g, while that of SiO_2 aerogel treated at 750°C is 810.4 m^2/g, which is due to the partial destruction of the structure and the collapse of the framework to varying degrees under high-temperature treatment, resulting in a decrease in specific surface area. As a candidate catalyst support, the extremely high specific surface area of SiO_2 aerogel can provide a good dispersing bed for the active component, provide a porous structure and high specific surface area for the catalyst, increase the contact area between the catalyst and the reaction gas, and thus promote the catalytic reaction.

3.3 Chapter summary

This chapter presents the preparation process control and basic characterization of SiO_2 aerogels prepared by sol-gel method. The summary of the experimental raw materials, microstructure, phase, specific surface area, and pore structure analysis is as follows:

(1) The sol with TEOS: urea=8:1 mL/g and heating reflux time of 1 h 20 min is more suitable for SiO_2 sol dropping sphere experiment. The spherical gels obtained in the PDMS coagulating bath at 80°C are independent of each other and structurally intact.

(2) The microstructure shows that SiO_2 aerogels are three-dimensional skeletal network materials composed of stacked oxide particles, with a mesoporous structure inside and uniform distribution of Si and O elements.

(3) Compared with other forms of SiO_2, the amorphous SiO_2 in SiO_2 aerogels usually has higher surface area and better catalytic performance, making it suitable as an excellent catalyst support material.

(4) BET analysis shows that the material has a mesoporous structure with a narrow pore size distribution range. The specific surface area of untreated SiO_2 aerogel can reach 1208.4 m^2/g, providing a good dispersing bed for the active component and increasing the contact area between the catalyst and the reaction gas, making it an ideal catalyst support material.

Chapter 4 Process and characterization of FMSA material preparation

According to literature records, doping Fe^{3+}into silica can increase the formation of HCHO[91, 92], and the dispersion of Fe sites can achieve high selectivity for oxygen-containing product HCHO[93]. MoO_3 can improve the selectivity of HCHO production by helping to eliminate harmful iron sites on the catalyst surface for selective oxidation of CH_4, maintaining high selectivity while extending the catalyst life[94-97].

Loading of iron-molybdenum oxides onto SiO_2 aerogel supports, composites with CH_4 catalytic activity and selectivity for HCHO. The high specific surface area of the aerogel support allows the active components to be highly dispersed in the catalyst, increasing the contact area between the reactant gas and the catalyst, facilitating the catalytic reaction. This chapter introduces the process control of the preparation of Fe-MoO_x/SiO_2 aerogel (FMSA) as a candidate catalyst material. The FMSA catalyst material was successfully prepared by heating reflux, sol-gel process and ethanol supercritical drying technique using TEOS as the silicon source, $Fe(NO_3)_3 \cdot 9H_2O$ as the iron source and doped MoO_3 composite. The influence of the active component loading and the heating and reflux process time on the preparation process is examined. A suitable preparation process was chosen to obtain structurally complete and homogeneous FMSA catalyst materials. The overall structure, composition and redox performance of the FMSA catalyst material were investigated by analyzing the microscopic morphology, physical phase, Fourier transform infrared spectroscopy, specific surface area and pore structure, XPS and H_2-TPR tests of FMSA.

4.1 Process of FMSA materials preparation

4.1.1 Sol-gel process

(1) The influence of urea addition on the sol-gel reaction

The amount of alkali catalyst added during the catalyst preparation process will directly affect the sol-gel process. During the preparation of SA, it can be found that the higher the amount of urea addition, the faster the sol gelation rate and the shorter the heating reflux time. In this chapter, the influence of different urea additions (TEOS: urea = 16:5, 16:7, 16:9 mL/g) on the 7-FMSA sol-gel process is continued to be investigated.

The heating reflux temperature was set at a uniform 80°C to observe the experimental process and the gelling of the sols. When TEOS: urea=16:5 mL/g and the heating reflux time was 2 h 40 min, the sol was gradually viscous and the MoO_3 oxide was evenly distributed in the mixed sol during the stirring process. After 5 min, the mixing speed decreases and the sol starts to gradually appear in a gelatinous state. The heating reflux device was turned off and the semi-solid gel was removed. Adjust the urea addition amount so that TEOS: urea=16:7 mL/g, and repeat the heating reflux experimental steps. When the heating reflux time reached 2 h, the sol began to gradually viscous, and the sol began to gel at 2 h 5 min. The experimental device was turned off, the semi-solid gels were removed and the experimental phenomena and gelling time were recorded. The sol-gel process was continued to investigate when the ratio of TEOS: urea=16:9 mL/g in the heating reflux experiment. When the heating reflux time was 1 h 35 min, the stirring speed was reduced and the sol started to gel. The heating reflux device was turned off and the samples were removed.

Table 4.1 The influence of urea addition on the experimental process.

Experiment	TEOS/ urea (mL/g)	Gel point time	Experimental phenomena
4-1-1	16/5	2 h 45 min	Start gelation
4-1-2	16/7	2 h 5 min	Start gelation
4-1-3	16/9	1 h 35 min	Start gelation

From this group of experiments, it can be seen that, similar to the heating reflux experimental process of SA in 3.1.1, the increase of urea addition will accelerate the sol-gel and shorten the sol-gel experimental process. Different from SA, the homogeneity of the sol is more strictly required in the experimental process of 7-FMSA due to the addition of MoO_3 powder oxide. Low sol consistency and long sol-gel times have led to a gradual precipitation of oxides during the gelling process, resulting in composites with an uneven distribution of MoO_3 oxides. It is easier to obtain uniform gel material by removing the sol as close to the gelling time as possible. In order to avoid too long heating reflux times and too rapid gelation due to excessive urea additions, the formulation TEOS: urea = 16:7 mL/g was chosen as the preparation process and applied in subsequent experiments.

(2) The influence of heating reflux temperature on the sol-gel reaction

The temperature of the heating reflux step determines the evaporation rate of the sol during the heating process, which in turn affects the rate of sol gelation. Here, the influence of heating reflux at different temperatures (82°C, 80°C and 78°C) on the sol-gel process was investigated. When the heating reflux temperature was set to higher than 82°C, it was found that the sol-gel temperature could not continue to rise after reaching 82°C. A large number of bubbles were generated on the surface of the sol-gel and the solvent evaporated rapidly, judging 82°C to be the boiling point of the sol-gel. The heating reflux temperature was set to 80°C and the heating reflux experiment was repeated without generating a large number of bubbles. When the heating reflux time was 2 h, the sol gradually viscous, and after 5 min the gelling phenomenon started to appear. The semi-solid gel was removed and placed in the mould, the heating reflux device was turned off, the time and experimental phenomena were recorded. The heating reflux temperature was continued to be reduced and set at 78°C. The heating reflux experiment was observed. Compared to the sols heated at 80°C, the colour of the sols gradually deepened during the heating and stirring process, which was due to the higher solvent evaporation caused by the longer heating and stirring time. The sol started to gel at 2 h 50 min. The samples were quickly removed, the heating and stirring device was turned off and recorded.

The results of this group of experiments show that for FMSA materials, the heating reflux temperature should not be higher than 82°C. A heating reflux temperature of 78°C will take longer to reach the gel point and will lead to a large amount of solvent evaporation, resulting in the densest sample and an overly dense structure. Therefore, a heating reflux temperature of 80°C was chosen as the preferred preparation process for subsequent experiments.

Table 4.2 The influence of heating reflux temperature on sol-gel reaction.

Experiment	Heating reflux temperature (°C)	Gel point time	Density (g/cm^3)
4-2-1	82	—	—
4-2-2	80	2 h 5 min	0.227
4-2-3	78	2 h 50 min	0.268

(3) The influence of heating reflux time on the sol-gel reaction

The length of the heating reflux time directly affects the gel state, which in turn affects the density and overall internal structure of the aerogel. In this group, 80°C was used as the heating reflux temperature to investigate the influence of different heating reflux times on the sol-gel process.

Table 4.3 The influence of heating reflux time on sol-gel reaction.

Experiment	Heating reflux time	Experimental procedure	密度 Density (g/cm^3)
4-3-1	1 h 30 min	Liquid sols	0.204
4-3-2	1 h 40 min	Liquid sols	0.209
4-3-3	1 h 50 min	Gradually viscous	0.219
4-3-4	2 h	Gradually viscous	0.224
4-3-5	2 h 10 min	Approaching gels	0.231

During the heating and reflux experiments, according to the previous experimental experience, a group of sol samples were taken in the mould every 10 min starting from the heating reflux time of 1h 30min. When the heating reflux time was 1h 30min, the sol showed a liquid shape with high fluidity, and the MoO_3 oxide was rotated in the mixed sol with the magnet, and the sol showed a non-uniform shape as a whole. When the heating reflux time was 1h 40min, the state of the sol was similar to that when the heating reflux time was 1h 30min. After the first two sol samples were taken out, there was obvious precipitation at the bottom of the mould, which was caused by the weak gelation of MoO_3 oxide in the liquidized sol. When the heating reflux time was 1h 50min, the sol gradually viscous, and the precipitation at the bottom of the mould after the removed sol samples were left to stand was mildly reduced compared with the first two samples, but there was still some precipitation at the bottom of the mould. When the heating reflux time was 2 h, the sol started to viscous gradually, and the sol was placed in the mould. After resting, it was found that the precipitation at the bottom of the mould was significantly reduced, which was due to the phenomenon that the sol started to gelatinize and prevented the accumulation of oxide precipitation. Continue to extend the heating reflux time to 2 h 10 min, the rotational speed of the magnet in the sol slowed down, the sol gradually began to appear gelling phenomenon. When the sample was removed and placed in the mould, no significant precipitation was observed at the bottom of the mould after resting.

Fig. 4.1 shows sample images of Fe-MoO_x/SiO_2 gels and 7-FMSA that has been supercritical dried in ethanol and heat treated at different heating reflux times. It can be seen in the sample images that the gel phase gradually decreases the precipitation at the bottom of the mould as the heating reflux time increases. The gradual gelation of the sol is also the process that encapsulates the oxide in it, preventing the deposition of MoO_3 oxide. As some of the organic matter in the material will be carbonized to different degrees during the ethanol supercritical drying process, the samples after drying appear carbon black, and the uniformity of the oxide distribution cannot be observed. The images of the samples after high temperature heat treatment shows that the first four groups of samples can be seen to be inhomogeneous, with obvious oxide precipitation at the bottom. In contrast, the fifth group of samples had good overall homogeneity and no obvious oxide precipitation was observed at the bottom.

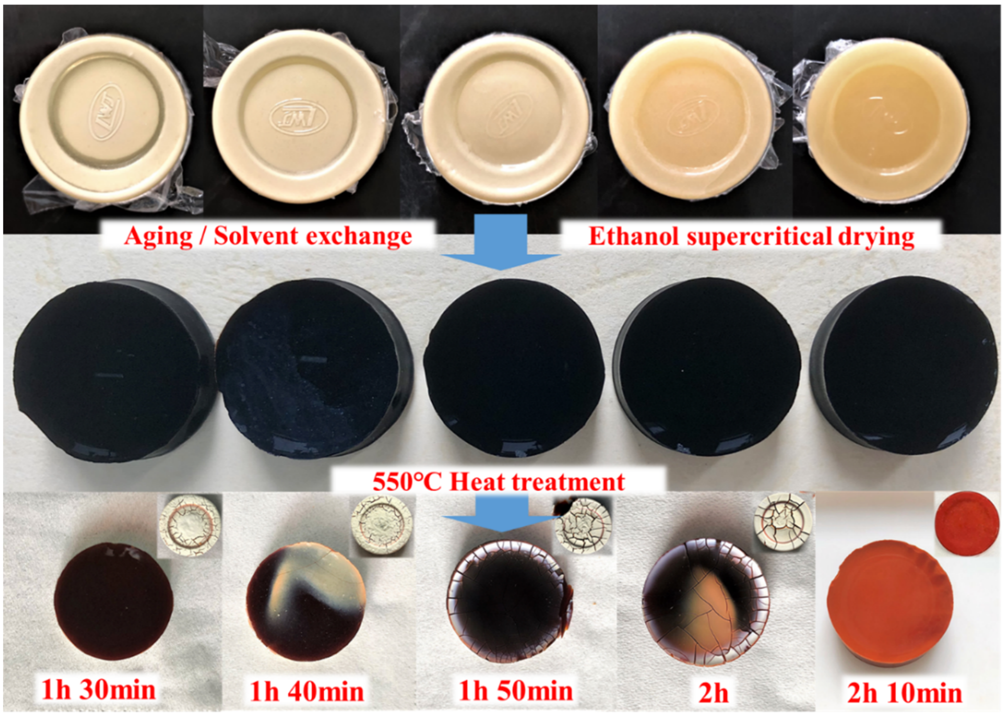

Fig. 4.1 Fe-MoO_x/SiO_2 gels and aerogels with different heating reflux times.

The results of this group of experiments show that the homogeneity of the samples is better with the increase of heating reflux time. As a block aerogel composite, a heating reflux time of 2h 10min might be more appropriate. If subsequent dropping sphere experiments are conducted, the heating reflux process time as a drop sphere backup sol is still to be investigated subsequently, considering that the process from taking out the sol to dropping sphere and then to gel takes some time.

4.1.2 Drop sphere process

In Chapter 3, the performance of the dropping sphere in different coagulating baths as well as coagulating bath temperatures was examined. In this chapter, PDMS was followed as the coagulating bath as well as the temperature environment of 80°C for the dropping sphere experiments. The influence of heating reflux time on the sol-gel process was investigated in section 4.1.1, and the experimental phenomena and the samples obtained from the preparation showed that a more uniform sol-gel could be obtained after a heating reflux time of 2 h. We took the sol-gels obtained with heating reflux time of 2 h and 2h 10min for subsequent dropping sphere experiments to observe the experimental phenomena and the state of the obtained spherical gels and aerogels.

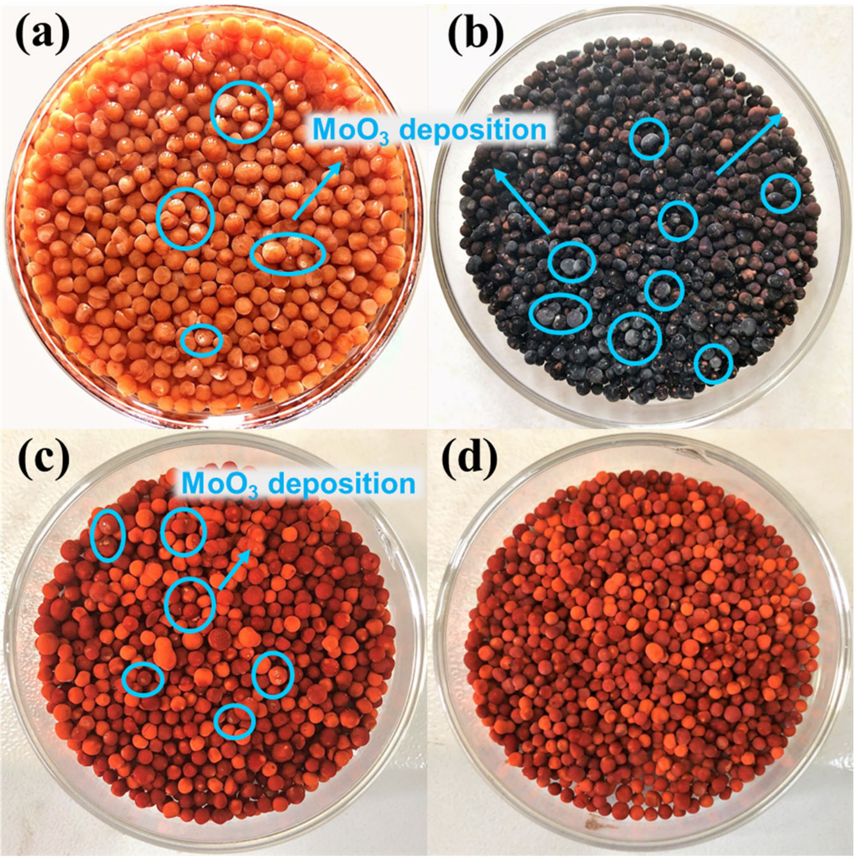

Fig. 4.2 Heating reflux time of 2h for (a) Fe-MoO$_x$/SiO$_2$ gel spheres, (b) 7-FMSA, (c) 7-FMSA after heat treatment at 550°C and (d) 7-FMSA after heat treatment at 750°C.

The PDMS coagulating bath was placed in a water bath, and the temperature of the water bath was set at 80°C. After the temperature of the water bath and the coagulating bath reached 80°C and stabilized, the sol with a heating reflux time of 2 h was taken for the dropping sphere experiment. The Fe-MoO$_x$/SiO$_2$ sol was taken with a dropper and slowly put into the PDMS coagulating bath. The sol formed into spheres rapidly in the

PDMS and then moved up and down in the coagulating bath with the heat flow in the PDMS coagulating bath. After about 2 min, the gel spheres sink and do not float anymore, and sit in a spherical state at the bottom of the PDMS coagulating bath. After 10 min, the gel spheres were removed and the spherical 7-FMSA was obtained after deionized water washing, ethanol solvent replacement, ethanol supercritical drying and heat treatment. The sample images during the experiment are shown in Fig. 4.2. During the gel phase of the sample, the deposited oxides are visible on the surface of the gel. This is due to the slow gelation of the sol in the coagulating bath. During the spherical sol sinking process and while sinking at the bottom of the coagulating bath, the oxides were gradually deposited at the bottom of the spherical sol by gravity, followed by slow gelation. This phenomenon indicates that the heating reflux time of the sol dropped into the coagulating bath is insufficient to reach the gelation point.

Subsequently, the performance of sol droplet spheres with a heating reflux time of 2h 10min was examined. The sol was dropped into the PDMS with a dropper, and the sol drops formed a spherical shape moving up and down with the heat flow. Similar to the previous set of experimental phenomena, the sphere of sol sank into the bottom of the cup containing the PDMS after a period of time. After resting, the gel was removed. The sample images of the spherical gel and aerogel are shown in Fig. 4.3. It can be seen that no significant oxide precipitation was observed on the surface of the gel and aerogel. This phenomenon indicates that the sol-gel quickly in the PDMS, and the oxide precipitation is cross-linked in the gel before it has time to precipitate by gravity, thus making the overall gel uniformity good.

This group of experiments examined the performance of sols with different heating reflux times in the dropping sphere experiment. Compared to the sols with a heating reflux time of 2h, the sols with a heating reflux time of 2h 10min dropped into gel spheres with better overall homogeneity and no significant oxide precipitation was observed. The sol-gel heating reflux time of 2h 10min was chosen as the spherical gel preparation process and continued with the preparation of the material.

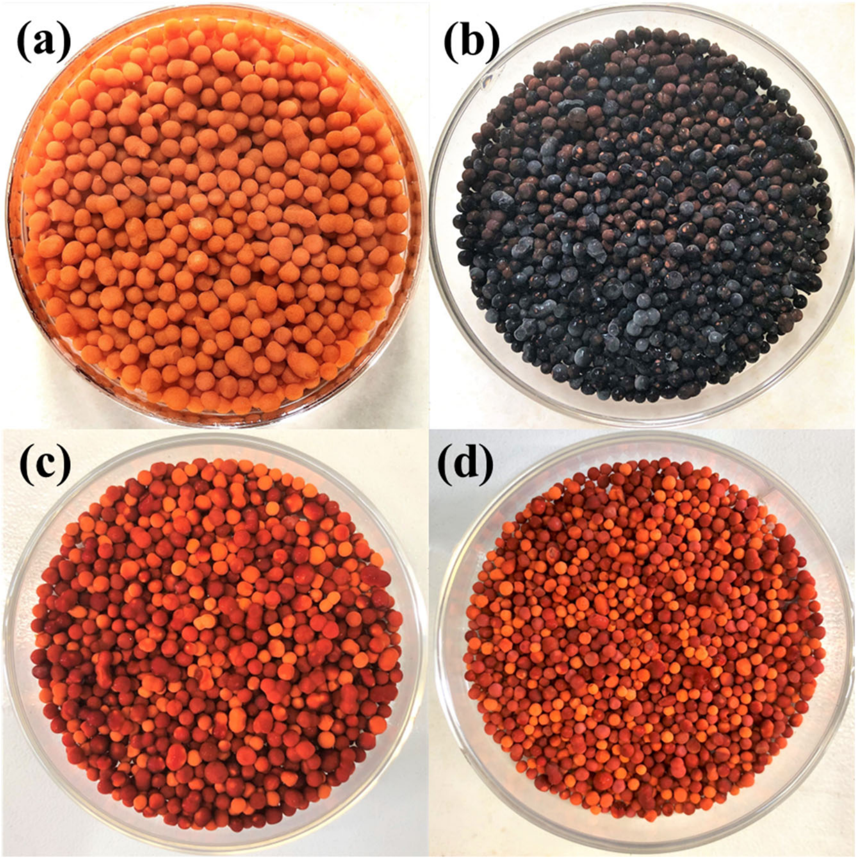

Fig. 4.3 Heating reflux time of 2h 10min for (a) Fe-MoO_x/SiO_2 gel spheres, (b) 7-FMSA, (c) 7-FMSA after heat treatment at 550°C and (d) 7-FMSA after heat treatment at 750°C.

4.2 Structural and property of FMSA materials

4.2.1 Micromorphological analysis

The structure and morphology of 7-FMSA were characterized by SEM, and the elemental distribution on the surface of the material was observed by mapping and elemental analysis at the microscopic level.

Fig. 4.4 shows the SEM microscopic morphology of 7-FMSA. Similar to the microscopic morphology of SA, the 7-FMSA sample has a three-dimensional network skeleton structure with nanoscale particles linked together and an abundance of nanoscale pores, mainly mesopores. Comparing with the SEM image of SA material, the SEM of 7-FMSA shows that the loading of Fe-MoO_x does not change the 3D network structure of SiO_2-based aerogel, and the mesopores and macropores can be seen distributed among the 7-FMSA material in Fig. 4.4 (d).

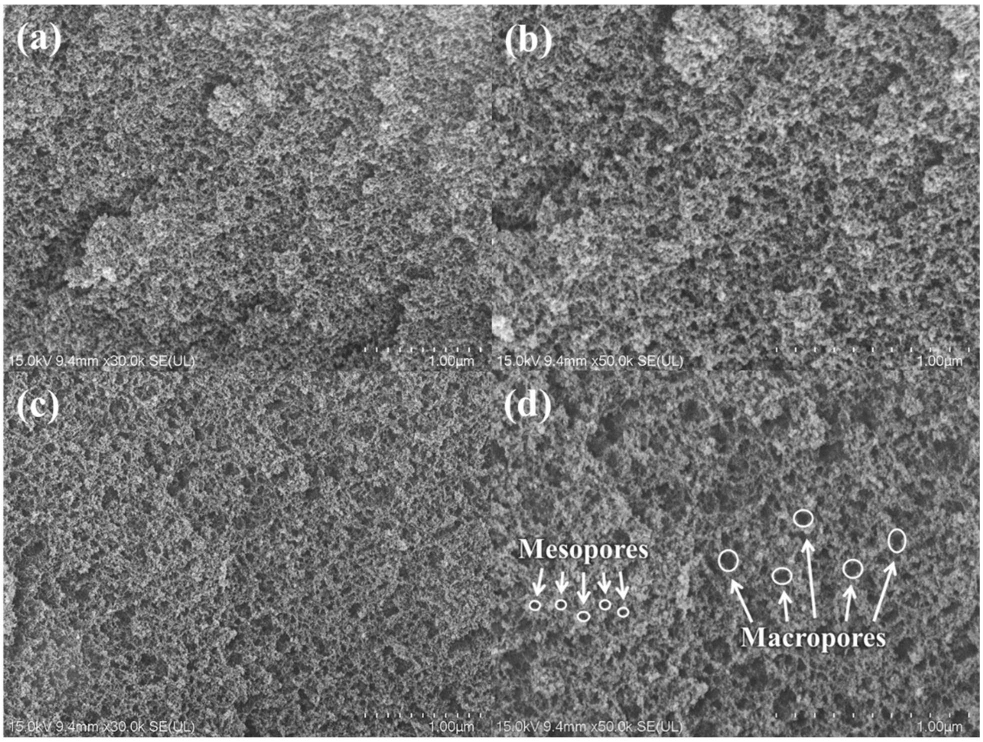

Fig. 4.4 SEM images of 7-FMSA.

Fig. 4.5 shows the elemental distribution of Fe, Mo, Si and O in the 7-FMSA samples, which shows that the total number of elemental distributions of Si and O is higher than that of Fe and Mo due to the low additions of Fe and Mo. The elemental signal distribution image shows that several elements are evenly dispersed in the test area and there is no significant build-up of elements. This indicates a homogeneous mixing of the sol during preparation and a good crosslinking of the Fe and Mo precursors with the Si-based sol. The homogeneous dispersion of active elements can improve the reaction efficiency of the reaction gas with the active components in the catalyst, thus improving the catalytic reaction efficiency.

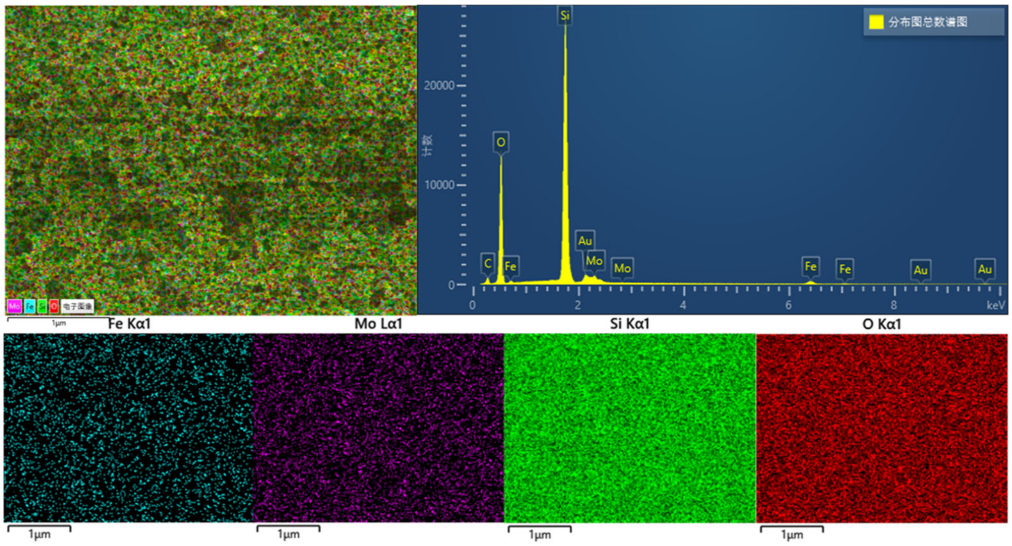

Fig. 4.5 Mapping and elemental distribution of 7-FMSA.

4.2.2 XRD analysis

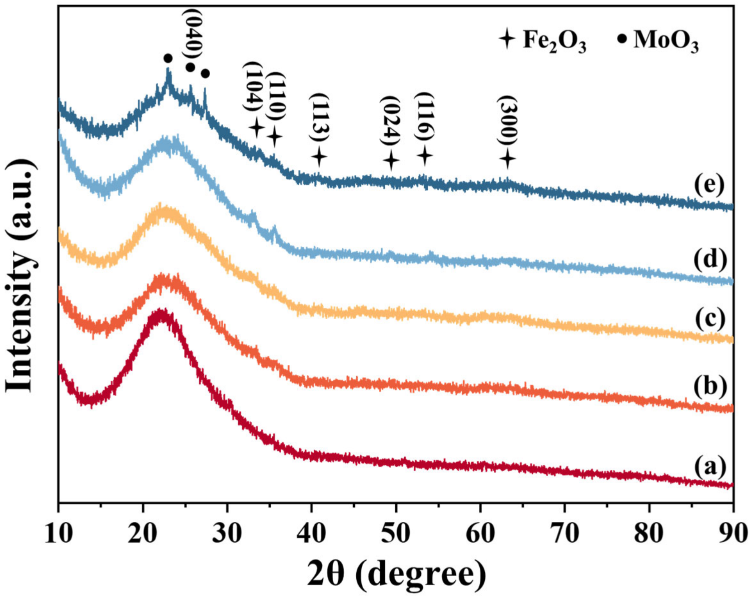

Fig. 4.6 XRD patterns of samples with different loadings of (a) SA, (b) 7-FMSA, (c) 13-FMSA, (d) 19-FMSA and (e) 25-FMSA.

To further observe the physical phases of the FMSA samples, XRD tests were performed on the materials. Fig. 4.6 show the XRD patterns of SA as well as FMSA with different loadings. No obvious characteristic peaks of Fe-Mo oxides were observed in the lower loading FMSA, and broad peaks of amorphous amorphous SiO_2 were present at 20~25°. This is due to the low content of Fe-Mo oxides in the lower loaded samples and their high dispersion in the pores of the SiO_2 aerogel structure, which makes Fe-Mo oxides difficult to be detected. With increasing loading, a faint characteristic peak of oxide appears. The characteristic peaks of Fe_2O_3 corresponding to (104), (110), (113), (024), (116) and (300) crystal planes and MoO_3 corresponding to (040) crystal planes can be seen at 25-FMSA[98-100].

4.2.3 FTIR analysis

The structure and chemical composition of the materials were investigated by FTIR, and Fig. 4.7 show the FTIR spectra of SA as well as FMSA with different loading amounts. The spectrum Fig. 4.7 (a) is the FTIR spectrum of pure SA with two distinctive characteristic peaks[101]. The characteristic peak at 470.63 cm^{-1} is attributed to the Si-O-Si bond angle vibration peak, which is related to the angle of the bond formed between different Si atoms in the SiO_2 molecule and the variation of the bond length, reflecting the conformation and angle of the Si-O-Si bond in the SiO_2 molecule. The characteristic peak at 1097.64 cm^{-1} is attributed to the Si-O stretching vibration band, and the generation of the peak is related to the vibration of the bonds formed between O atoms and adjacent Si atoms in the SiO_2 molecule. In Fig. 4.7 (b~c), the characteristic peaks of the active oxide component Fe-MoO_x cannot be observed clearly in the plots of 7-FMSA with lower loading, and the characteristic peaks of the active component appear gradually with increasing loading. The characteristic peaks appearing at 916.08 cm^{-1} and 910.45 cm^{-1} in Fig. 4-7 (d~e) are attributed to specific frequency infrared absorption peaks caused by vibrations of the Mo-O-Mo bond angles. This stems from the vibration of the chemical bond between molybdenum (Mo) and oxygen (O) oscillating or bending at an angle in the molecule [102, 103]. The Fe component is difficult to observe in FTIR due to its low loading and high dispersion in the SiO_2 pores.

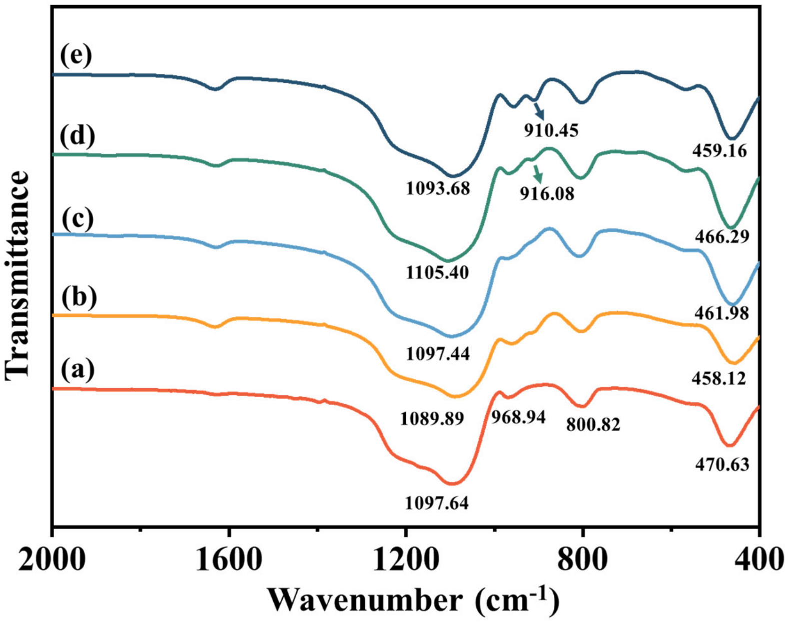

Fig. 4.7 FTIR spectra of samples with different loadings of (a) SA, (b)7-FMSA, (c) 13-FMSA, (d) 19-FMSA and (e) 25-FMSA

4.2.4 Specific surface area and pore structure analysis

To evaluate the pore structure and specific surface area of the 7-FMSA material, BET tests were performed on the 7-FMSA samples calcined at different temperatures. The N_2 adsorption-desorption isotherms and pore size distribution of the 7-FMSA samples are shown in Fig. 4.8. The specific surface area and average pore size are shown in Table 4.4. The isotherms in Fig. 4.8 (a) show that the samples heat-treated at different temperatures show type IV isotherms with H1-type hysteresis loops. The spherical particles in the material are uniform in size, which are typical of mesoporous materials[104]. At the same relative pressure, the adsorption of N_2 was higher for the 7-FMSA sample calcined at 550°C than that of the sample calcined at 750°C. The specific surface area of the 7-FMSA sample calcined at 550°C was 1049.9 m^2/g, which was higher than that of the sample calcined at 750°C (710.1 m^2/g). The average pore size of the 7-FMSA samples calcined at 750°C (19.8 nm) was higher than that of the samples calcined at 750°C (15.2 nm) due to the change in pore structure brought about by the increased calcination temperature. From the results, it is clear that the loading of

Fe-MoO_x reduces the specific surface area of the composites to a certain extent compared to the specific surface area of 1208.4 m^2/g of the untreated pure SA. The specific surface area of the 7-FMSA composites remained at a high level due to the relatively stable overall structure of the SA support.

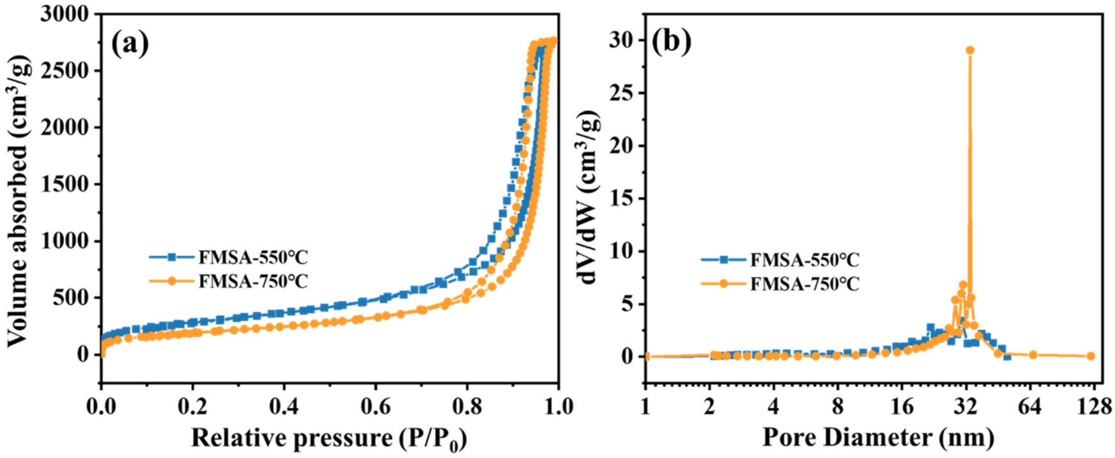

Fig. 4.8 (a) N_2 adsorption-desorption isotherm and (b) pore size distribution of 7-FMSA.

Table 4.4 Specific surface area and average pore size of FMSA and FMSA-750.

Sample Name	Specific surface area (m^2/g)	Average pore size (nm)
FMSA	1049.9	15.2
FMSA-750	710.1	19.8

4.2.5 XPS analysis

In order to characterize the information on the chemical composition, the chemical bonding state, and the electronic valence state of the elements, the XPS spectra of the materials were tested. Fig. 4.9 shows the total spectrum of 7-FMSA as well as the high-resolution spectrum of each element. The characteristic peaks of the contained elements can be seen in the full spectrum of 7-FMSA in Fig. 4.9 (a), which have low intensity due to the low loading of Fe and Mo. The high-resolution spectrum of Fe 2p in Fig. 4.9 (b) shows the XPS characteristic peaks of Fe $2p_{3/2}$ and Fe $2p_{1/2}$ at two different energy levels. Fe 2$p_{3/2}$, with its lower energy and stronger electron binding energy, is relatively more susceptible to the chemical environment of the sample surface, while Fe 2$p_{1/2}$, with its higher energy and lower electron binding energy, may have a stronger signal for the more reactive iron atoms or ions in the sample. The Mo 3$d_{5/2}$ and Mo 3$d_{3/2}$ peaks in the high-resolution spectrum of Mo 3d (Fig. 4-9 (c)) can be resolved as two peaks of different energy levels within the molybdenum atom, located at 232.8 eV and 235.8 eV, respectively. The Mo 3$d_{5/2}$ peak is stronger and sharper than the Mo 3$d_{3/2}$ peak[105].

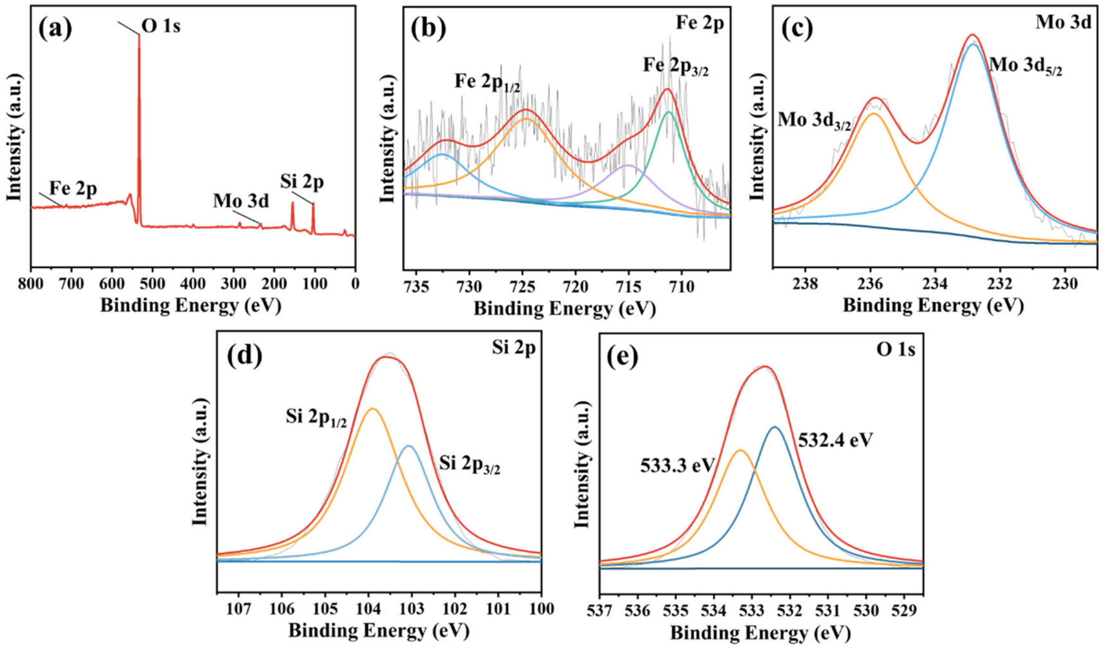

Fig. 4.9 XPS spectra of (a) 7-FMSA; High-resolution XPS spectra of (b) Fe 2p, (c) Mo 3d, (d) Si 2p and (e) O 1s of 7-FMSA.

4.2.6 H_2-TPR analysis

Examining the reduction ability of the samples by H_2-TPR is an important characterization to judge the catalyst activity. Fig. 4.10 show the H_2-TPR profiles of FMSA with different loadings. The reduction peaks regarding Fe_2O_3 mainly appeared in two intervals, the reduction peaks in the 200~300°C interval were mainly generated by the reduction of Fe^{3+} to Fe^{2+}, the reduction peaks in the high temperature range 550~700°C were attributed to the further reduction of the reduced Fe^{2+} to metallic iron[91, 106]. A distinct reduction peak is present in the temperature range 350~500°C, which corresponds to the reduction reaction due to the presence of oxygen vacancy defects in the MoO_3 lattice structure [107]. The profiles of the different loadings of FMSA show that the intensity of the reduction signal is more significant in the lower temperature range for the samples with lower loadings. In the higher temperature range, the intensity of the reduction signal is more obvious for the sample with higher loading.

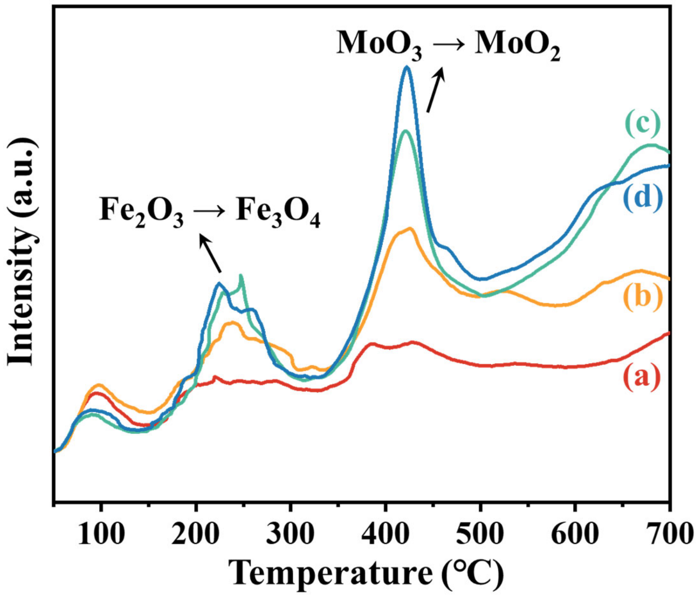

Fig. 4.10 H_2-TPR profiles of (a) 7-FMSA, (b) 13-FMSA, (c) 19-FMSA and (d) 25-FMSA.

4.3 Chapter summary

This chapter introduces the process control of the preparation of FMSA synthesized by heating reflux and sol-gel methods and the characterization of the material structure and basic properties. By investigating the influence of urea addition, heating reflux temperature and time on the sol-gel process, a suitable preparation process was selected to produce mixed sol-gel and drop sphere experiments were performed. The internal structure and redox properties of the materials were characterized by testing and analyzing the microscopic morphology, XRD, FTIR, BET, XPS, and H_2-TPR of the FMSA samples, which are summarized as follows:

(1) TEOS: urea = 16:7 mL/g, a heating reflux temperature of 80°C and a heating reflux time of 2h 10min were used as the preferred sol-gel preparation process and a PDMS coagulation bath at 80°C was used for drop sphere experiments.

(2) Similar to SA, FMSA has a three-dimensional network skeleton structure with nanoscale particles connected, and the pore structure is mainly mesoporous. The active component Fe-MoO_x is uniformly dispersed in the composite without obvious aggregation.

(3) XRD, FTIR and XPS analysis proved the successful doping of the Fe-MoO_x active component.

(4) The specific surface area of the 7-FMSA sample calcined at 550°C was 1049.9 m^2/g, higher than the specific surface area of 710.1 m^2/g for the sample calcined at 750°C.

(5) The H_2-TPR test showed that the FMSA samples with low loading showed a high reduction signal in the low temperature range.

The composite FMSA can be used as a candidate catalyst material for subsequent testing of CH_4 catalytic conversion experiments due to its highly dispersed active component, high specific surface area and redox capacity.

Chapter 5 Process and characterization of FPSA material preparation

It has been demonstrated that iron phosphate ($FePO_x$) catalysts exhibit high selectivity in the partial oxidation of CH_4 or C_2H_6 with O_2-H_2 or N_2O[108]. The partial oxidation of CH_4 using O_2 over $FePO_x$ catalysts is capable of selective formation of HCHO. The researcher mentioned that loading $FePO_x$ onto SiO_2 can improve the conversion of CH_4 to HCHO [109]. Compared to ordinary SiO_2 powders, the high specific surface area of SiO_2 aerogels and the three-dimensional network structure with abundant pores provide a more suitable bed for the active components and have more obvious advantages as catalyst supports. Thus, the loading of $FePO_x$ into silica aerogel can be used as a candidate catalyst material for the selective direct catalytic conversion of CH_4 to HCHO. FPSA candidate catalyst materials were synthesized using TEOS as the silicon source, $Fe(NO_3)_3{\cdot}9H_2O$ and $NH_4H_2PO_4$ as the raw materials for the synthesis of $FePO_x$ components by heating reflux and sol-gel methods combined with ethanol supercritical drying technology. This chapter describes the process control of FPSA composites during preparation, microscopic morphological analysis, XRD, FTIR, BET, XPS and H_2-TPR testing of the material, analysis and discussion of the structural and performance of the material.

5.1 Process of FPSA materials preparation

5.1.1 Sol-gel process

(1) The influence of urea addition on the sol-gel reaction

Urea is still used as an alkali catalyst to promote sol-gel cross-linking during the heated reflux process for the preparation of FMSA materials. The amount of urea added affects the cross-linking rate of the sol during the sol-gel process. The influence of urea addition (TEOS: urea = 16:7, 16:9, 16:11 mL/g) on the heating reflux process was investigated in the preparation process of 4-FPSA materials.

The heating reflux temperature was set to 80°C for the mixed sols with different urea additions. The data and experimental phenomena are recorded in Table 5.1. When urea was added at TEOS: urea = 16:7 mL/g, a gradual increase in the vicosity of the sol began to occur at a heating reflux time of 2 h 50 min. The heating stirrer was turned off, the sol was removed and the time recorded. The mixed sol was prepared by setting the urea addition to TEOS: urea = 16:9 mL/g and subjected to heating reflux experiments. The solution became viscous at a heating reflux time of 2 h 10 min. The sol became gradually viscous at a heating reflux time of 2 h 10 min when urea was added at TEOS: urea = 16:9 mL/g. Based on the experimental results, a solution with a moderate heating reflux time was taken and the urea addition of TEOS: urea = 16:9 mL/g was applied to the subsequent experimental preparation.

Table 5.1 The influence of urea addition on the experimental process of 4-FPSA.

Experiment	TEOS/Urea (mL/g)	Gel point Time	Experimental phenomena
5-1-1	16/7	2 h 50 min	Start of gelling
5-1-2	16/9	2 h 10 min	Start of gelling
5-1-3	16/11	1 h 40 min	Start of gelling

(2) The influence of heating reflux time on the sol-gel reaction

During the experimental preparation, the heating reflux time affects the time for the sol to become a gel and the structure of the material. It is important to avoid difficulties in solidifying the sol due to short heating reflux times and to avoid gelation during the preparation of the sol due to long heating reflux times. Starting with a heating reflux time of 1h 35min, a set of sol-gel samples were taken every 10 min and placed in the moulds. After gelation in the mould, ageing, solvent replacement and supercritical drying in ethanol, the aerogel samples were obtained. Fig. 5.1 shows sample images of the wet gel after different reflux times and the aerogel after supercritical drying. It can be seen that the homogeneity of both the wet gel state and the aerogel state differs for samples that have undergone different heating reflux times. As the heating reflux time increases, the overall homogeneity of the sample is better. When the heating reflux time exceeds 2h15min, the sol starts to gel, at which point the sol appears semi-solid.

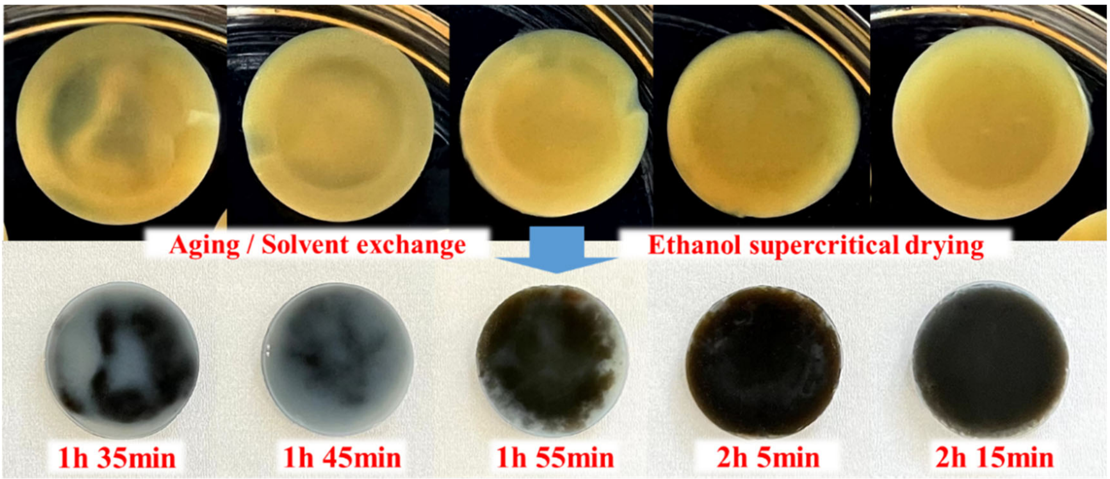

Fig. 5.1 Images of gel and aerogel samples with different reflux times.

Table 5.2 The influence of heating reflux time on the sol-gel reaction of 4-FPSA.

Experiment	Heating reflux time	Experimental procedure	Density (g/cm^3)
5-2-1	1h 35min	Uneven gelation	0.252
5-2-2	1h 45min	Uneven gelation	0.263
5-2-3	1h 55min	Uneven gelation	0.286
5-2-4	2h 5min	Uniform gelation	0.293
5-2-5	2h 15min	Uniform gelation	0.301

When the heated reflux time was 1h 35min, the sol takes on a liquid state and inhomogeneity can be seen in the gels obtained after sol-gel and ageing in a 50°C environment. The sols obtained with a heating reflux time of 1h 45min still appear liquid and are not homogeneous after gelation. After 1h 55min heating the refluxed sol started to be viscous and the homogeneity of the gels obtained was significantly improved. After 2h 5min heating reflux the gel appears more homogeneous, while the gels obtained after 2h 15min heating and refluxing time were basically homogeneous and had a better overall structure. As subsequent dropping sphere experiments were required, it was more beneficial to remove the sol at a heating reflux time of 2h10min for subsequent experiments.

5.1.2 Drop sphere process

The PDMS was still chosen as the coagulation bath based on the previous drop sphere experiments. The temperature of the water bath was set to 80°C and the coagulation bath was placed in the water bath. After the water bath and the coagulation bath had both been raised to 80°C and stabilized, the sol was removed after 2h10min of heating reflux for the drop sphere experiments. The drops were placed drop by drop into the PDMS using a dropper, with the drops spaced some distance apart to avoid merging before they gel. Due to surface tension, the sol took a spherical shape immediately after being dropped into PDMS. As the heat flow occurs during the heating process, the spherical sol droplets began to move up and down in the coagulating bath. Due to the 80°C temperature that PDMS had to accelerate the gelation of the sol, the process of spherical sol swimming in PDMS is also the process of gelation. After 2 min, the spherical sol gradually landed on the bottom of the PDMS. During this process, the sol spheres were not completely gelled, and all the sol spheres gradually sank to the bottom of the container. After 10 min, the sol gradually gelled and the gel spheres were separated from the PDMS using a strainer. The gel spheres were washed several times in deionized water and the spheres were transferred to the solvent displacement solution ethanol. The replacement solution and gel spheres were placed in an oven at 50°C for ageing and solvent replacement. During this period, the internal structure of the spherical gel was gradually glued intact and the gel sphere was gradually made transparent. Spherical aerogel FPSA was obtained by supercritical drying with ethanol and calcination, the size of the spherical aerogel can be controlled by the amount of sol in a single drop.

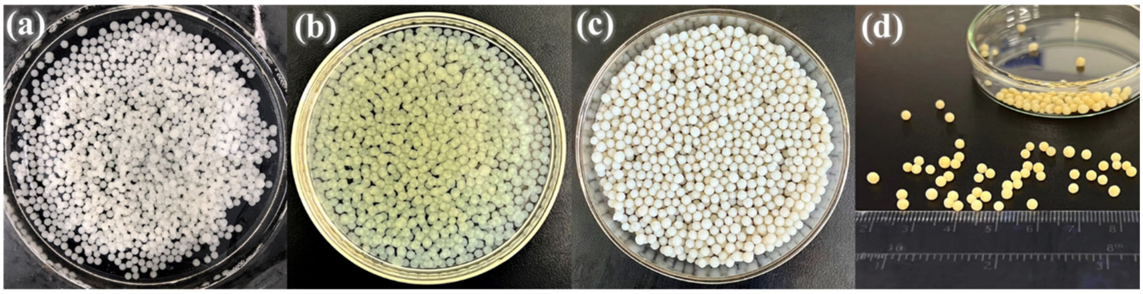

Fig. 5.2 Spherical 4-FPSA preparation process of (a) gel in PDMS, (b) gel after solvent replacement, (c) spherical aerogel and (d) spherical aerogel after calcination.

Fig. 5.2 illustrates the morphology of the spherical 4-FPSA in different states during preparation. Fig. 5.2 (a) shows a sample after the sol has been dropped in PDMS for a period of time, during which the sol gradually gels. After the gel was removed and aged in ethanol and solvent replacement, the gel gradually became transparent, as shown in Fig. 5.2 (b). Subsequently, after supercritical drying in ethanol (Fig. 5.2 (c)) and high temperature heat treatment, spherical 4-FPSA composites were obtained as shown in Fig. 5-2 (d).

5.2 Structural and property of FPSA materials

5.2.1 Micromorphological analysis

Fig. 5.3 shows the SEM images of the 4-FPSA and the distribution of the different elements in the 4-FPSA as observed by mapping.

The sol-gel preparation process combined with the ethanol supercritical drying technology makes it easier to obtain porous materials. Fig. 5-3 (a~b) shows that the internal structure of the 4-FPSA is honeycomb-type and has an abundance of pore structures. As can be seen in Fig. 5.3 (c~d), the silica nanoparticles are connected in a typical "pearl-like" skeleton to form a continuous pore structure with mainly mesopores. In the composites, the doping of the $FePO_x$ component does not have a significant effect on the morphology. The overall morphology of the 4-FPSA is similar to that of the SA, and the internal pores of the composites are mainly mesoporous.

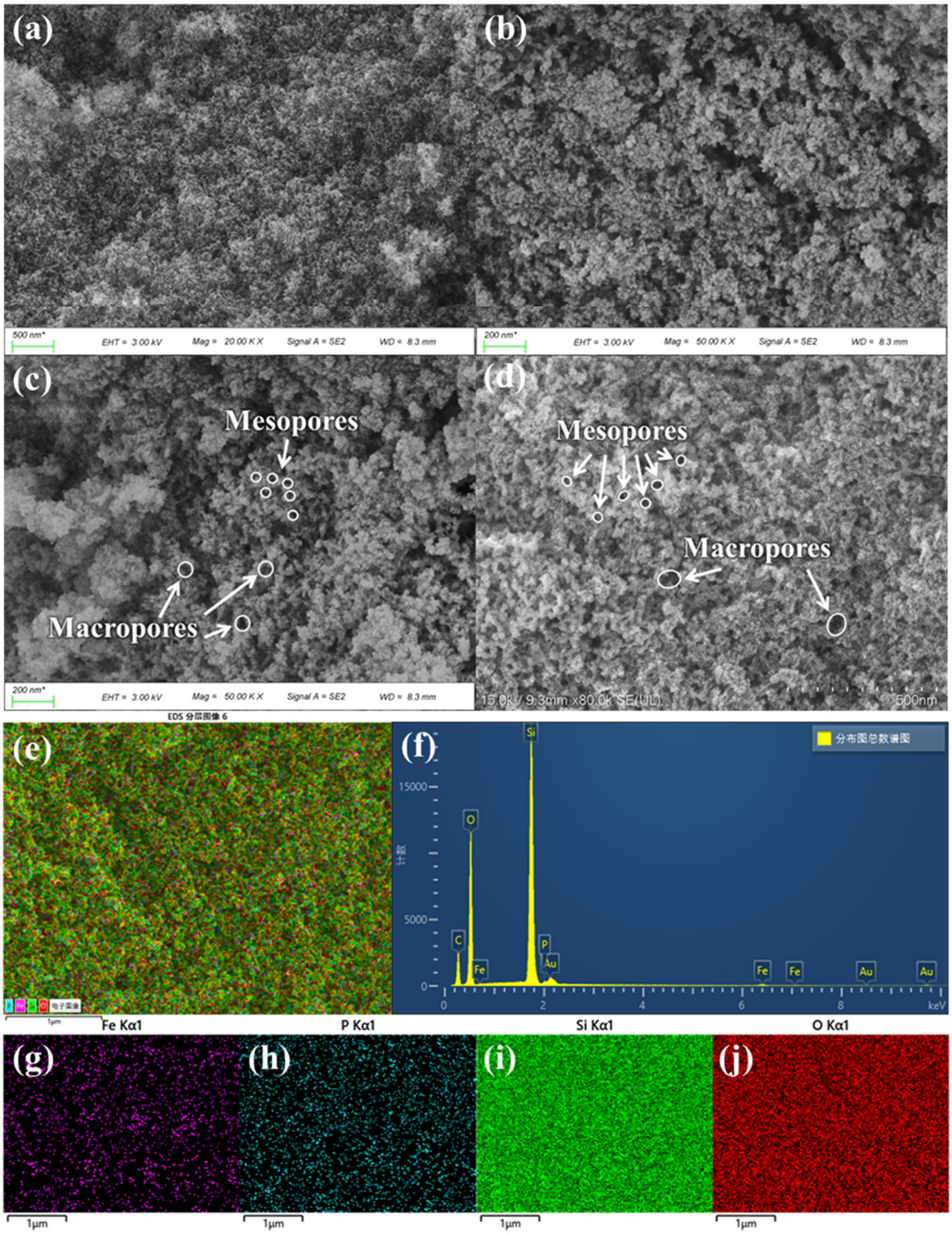

Fig. 5.3 (a~d) Surface morphology and (e~j) mapping and EDS images of 4-FPSA.

In order to further understand the distribution of elements in the composite, a local mapping analysis was performed on the composite 4-FPSA. The number of major elements and the distribution of elemental signals were shown in Fig. 5.3 (e~j). Fig. 5.3 (f) shows that the amount of Fe and P was low due to the low addition of the $FePO_x$ component. The sol-gel preparation process allows for homogeneous mixing of the raw materials and uniform dispersion of the active components in the sol during the preparation stage. Fig. 5.3 (g~j) shows a high degree of dispersion on the SiO_2 support, although the amounts of Fe and P are small. As a catalyst material, the high dispersion of the active component on the surface contributes to the catalytic efficiency and improves the selectivity of HCHO.

5.2.2 XRD analysis

In order to further understand the physical phase of the FPSA, XRD tests were carried out on the composite FPSA. Fig. 5.4 shows the XRD patterns of SA and FPSA with different $FePO_x$ loadings. In the XRD pattern of SA, a broad diffraction peak can be observed at a 2θ of 22°, indicating that the silica is present in an amorphous form. This was mainly attributed to the fact that the sol-gel preparation process made the atoms or molecules in the composite materials in a random arrangement state without periodicity. the 2θ of the characteristic peaks of silica shifted to higher values with increasing $FePO_x$ loading[110]. No obvious $FePO_x$ characteristic peaks were observed in the XRD patterns of FPSA with different loadings. This may be due to the fact that $FePO_x$ is highly dispersed on the mesoporous channels or pore walls of silica aerogels, making it difficult to detect by XRD.

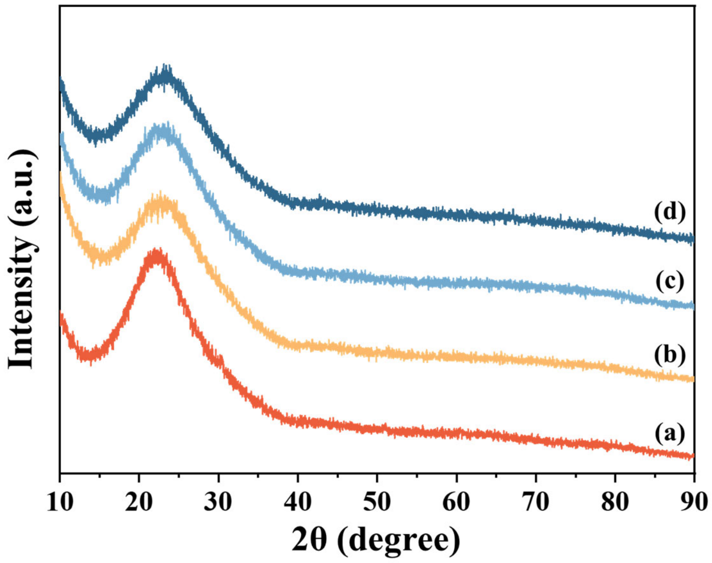

Fig. 5.4 XRD patterns of (a) SA, (b) 4-FPSA, (c) 8-FPSA and (d) 16-FPSA.

5.2.3 FTIR analysis

In order to investigate the structure and chemical composition of the composite FPSA, FTIR tests were carried out to analyze it. Fig. 5.5 show the FTIR profiles of SA and FPSA with different loadings in the range of 400~2000 cm^{-1}. The characteristic vibrational range around 458.41~470.63 cm^{-1} was attributed to Si-O symmetric bending vibration and the absorption band around 1089.60~1097.64 cm^{-1} was attributed to Si-O-Si asymmetric stretching due to the interaction between multiple Si atoms[101, 111]. Due to the low content of Fe and P elements, no significant absorption bands associated with them were found in the FTIR. The effective loading of the active components is corroborated by a certain degree of displacement of the characteristic vibrational regions in the FTIR spectra of the samples with different loading amounts.

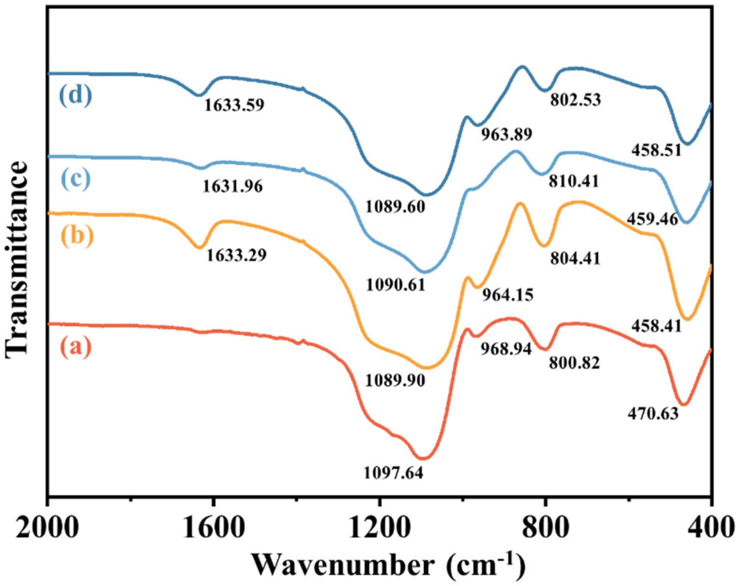

Fig. 5.5 FTIR spectra of (a) SA, (b) 4-FPSA, (c) 8-FPSA and (d) 16-FPSA.

5.2.4 Specific surface area and pore structure analysis

In order to investigate the specific surface area and pore structure of the samples, BET-BJH analysis was carried out on samples 4-FPSA at different heat treatment temperatures FPSA-550°C, FPSA-650°C and FPSA-750°C[112]. Fig. 5.6 shows the N_2-sorption and desorption isotherms and pore size distribution curves for 4-FPSA obtained at different heat treatment temperatures and the data are shown in Table 5.1. All isotherms in Fig. 5.6 (a) showed H1-type hysteresis loops, which were type IV isotherms, and this was attributed to the typical capillary condensation mechanism that occurs in mesoporous materials[104]. The saturated adsorption platform on the adsorption isotherm reflected the uniform pore size distribution of the material, consisting of spherical particles of uniform size[113]. As the heat treatment temperature increased, the amount of nitrogen adsorbed at the same relative pressure decreased, and the corresponding specific surface area also decreased, due to the fact that the high temperature destroyed the pore structure of the aerogel to a certain extent. The specific surface area of 4-FPSA heat-treated at 550°C was as high as 1174.71 m^2/g. As the heat treatment temperature increased, the specific surface area of the composites heat treated at 650°C was 925.31 m^2/g and that of the composites heat treated at 750°C was 829.99 m^2/g.

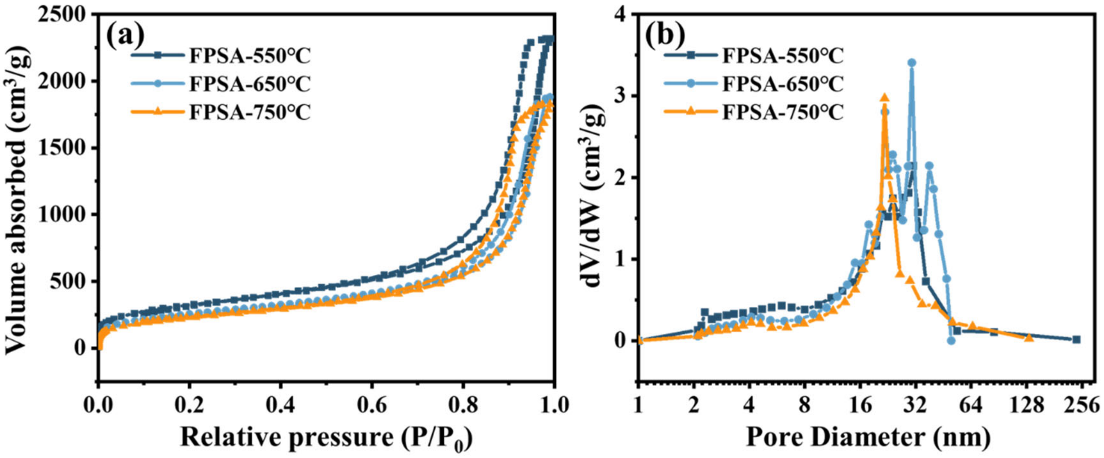

Fig. 5.6 (a) Nitrogen adsorption/desorption isotherms and (b) pore size distribution curves of FPSA-550°C, FPSA-650°C, FPSA-750°C.

Combined with the pore size distributions in Fig. 5-6 (b), the average pore sizes of the 4-FPSA samples at different heat treatment temperatures were all in the range of 12~16 nm, further proving that 4-FPSA was a mesoporous material consisting of homogeneous spherical particles. The high specific surface area of the catalyst material was able to increase the degree of dispersion of the active component in the catalyst, thus improving the selectivity for the target product HCHO in the catalytic reaction.

Table 5.3 Pore structure of FPSA-550℃, FPSA-650℃, FPSA-750℃.

Sample	BET surface area (m^2/g)	Average pore size (nm)
FPSA-550℃	1174.71	12.53
FPSA-650℃	925.31	15.16
FPSA-750℃	829.99	13.31

5.2.5 XPS analysis

Information on the elemental composition of the 4-FPSA surface was investigated by XPS analysis. Fig. 5.7 show the full XPS spectrum of 4-FPSA, as well as the high-resolution XPS spectra of Fe 2P, P 2P, Si 2P and O 1s. Fig. 5.7 (a) shows the full XPS spectrum of 4-FPSA, where the characteristic peaks of each constituent element can be seen. The peak intensities of Fe 2P and P 2P are relatively low due to the low doping of Fe and P. Fig. 5.7 (b) shows two characteristic peaks of the Fe 2P spectrum, attributed to Fe $2p_{1/2}$ and Fe $2p_{3/2}$[114]. At 712.0 eV was the Fe $2p_{3/2}$ peak, reflecting mainly the vacancy left by the ionization of an electron in the 2p orbital of the iron atom, pointing to the Fe^{3+} oxidation state, proving the presence of Fe^{3+} in the material [115, 116] . The Fe $2p_{1/2}$ peak was more sensitive to the response of the Fe chemical environment compared to the Fe $2p_{3/2}$ peak. The P 2p peak in Fig. 5.7 (c) was located at 133.4 eV, with two peaks at 134.0 eV and 133.3 eV attributed to P $2p_{1/2}$ and P $2p_{3/2}$, respectively[114]. The O 1s spectrum of Fig. 5.7 (e) could be fitted to two peaks, the one at 532.9 eV attributed to surface hydroxyl oxygen and the one at 533.7 eV attributed to lattice oxygen[117]. Surface hydroxyl oxygen refers to surface adsorbed oxygen molecules or ions connected to atoms or molecules on the surface by chemical bonding, which has high chemical reactivity and plays an important role in catalytic reactions, redox [118, 119].

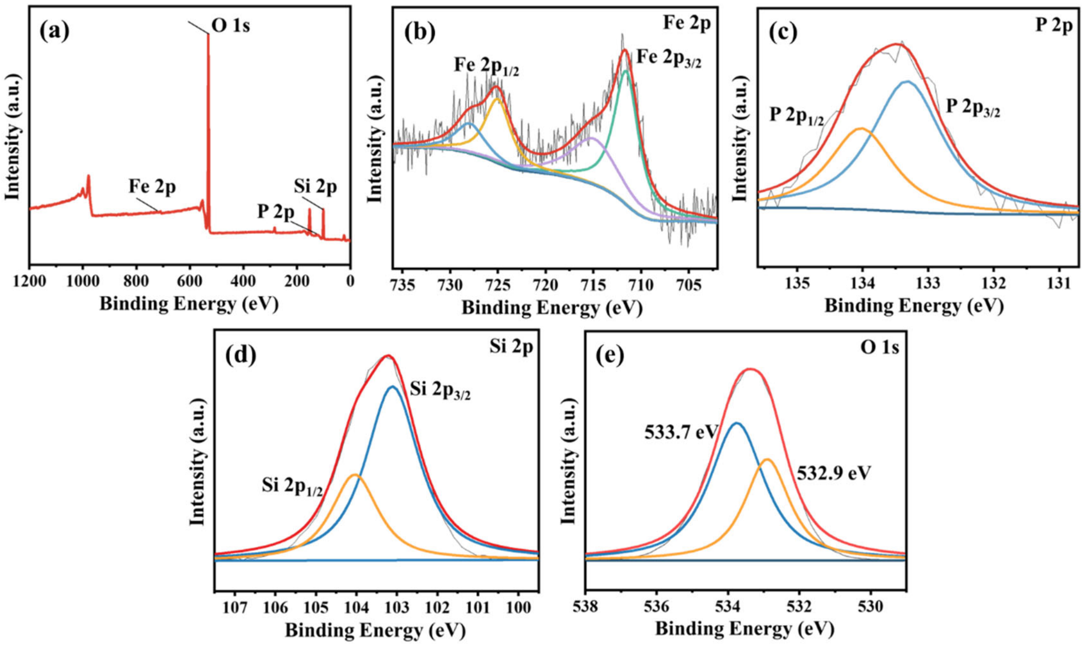

Fig. 5.7 XPS spectra of (a) 4-FPSA; High-resolution XPS spectra of (b) Fe 2p, (c) P 2p, (d)Si 2P and (e) O1s of 4-FPSA.

5.2.6 H_2-TPR analysis

The catalytic activity of catalyst materials is related to their redox properties, which were investigated using the H_2-TPR test.

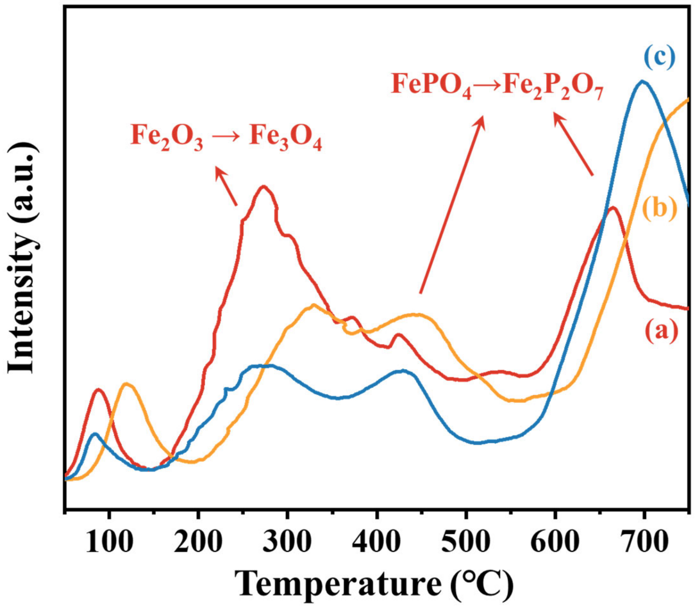

Fig. 5.8 H_2-TPR profiles of (a) 4-FPSA, (b) 8-FPSA and (c) 16-FPSA.

Fig. 5.8 show the H_2-TPR profiles of the FPSA for different loads. The reduction peaks appearing at 200~350°C were attributed to the reduction reaction of Fe^{3+} to Fe^{2+} due to the presence of oxygen vacancy defects in the Fe_2O_3 lattice structure[120]. The reduction peaks appearing at 350~550°C and after were mainly attributed to the conversion of $FePO_x$ to $Fe_2P_2O_7$[43, 121]. The reduction peaks appear at different locations for different loadings of FPSA, with the least loaded 4-FPSA samples appearing in the lower temperature range. 4-FPSA showed a strong reduction peak for the reduction of Fe^{3+} to Fe^{2+}. The reduction signal decreased in the lower temperature range as the loading increased. The results of the H_2-TPR test showed that the reduction signal of the lower loaded 4-FPSA appeared at a lower temperature with a stronger signal. This trend is like previous reports in the literature, the lower loading contributed to the increased dispersion of the active substance, which led to materials that could undergo reduction reactions at lower temperatures.

5.3 Chapter summary

This chapter described the preparation of FPSA candidate catalyst materials by a heated reflux sol-gel method in combination with ethanol supercritical drying technology. The sol-gel preparation process of FPSA and the control of the dropping sphere process were examined, and the structural and performance of the material was discussed through microscopic morphological analysis, XRD, FTIR, BET, XPS and H_2-TPR tests.

(1) The sol-gel preparation formulation was prepared with urea addition of TEOS: Urea = 16: 9 mL/g and a heating reflux time of 130 min.

(2) SEM images showed that the internal structure of FPSA exhibited a honeycomb-like structure with abundant pores dominated by mesopores. The active components were uniformly dispersed on the SiO_2 support.

(3) The 4-FPSA obtained at different heat treatment temperatures showed H1-type hysteresis loops, reflecting that the 4-FPSA is a nanocomposite with uniform pore size

distribution composed of uniformly sized spherical particles. The specific surface area of 4-FPSA with heat treatment at 550°C was as high as 1174.71 m^2/g.

(4) The reduction peaks of Fe_2O_3 and $FePO_x$ were observed for all the H_2-TPR profiles of FPSA with different loadings. The reduction signals of the lower loaded 4-FPSA appeared at a lower temperature with stronger signals due to the lower loading which was beneficial to improve the dispersion of active substances.

After analysis and discussion, the high specific surface area and highly dispersed active components of spherical FPSA contribute to the catalytic reaction by contact between the reactant gas and catalytic active components in the catalytic reaction. The composite material had redox capabilities that contributed to the catalytic reactions that occurred. After testing and analysis, FPSA can be used as a candidate catalyst for catalytic oxidation of CH_4 to HCHO.

Chapter 6 Performance of catalyst selective catalytic oxidation of methane in fixed bed reactor

Methane (CH_4) is a non-polar molecule, and its activation is challenging due to the high C-H bond energy [122]. However, the oxidation products of CH_4 are much more active than CH_4. To avoid the deep oxidation of the target product HCHO to CO or CO_2, high selectivity of HCHO is crucial for the direct catalytic conversion of CH_4[123]. Previous studies have shown that highly dispersed Fe sites on SiO_2 are beneficial for the production of the target product HCHO, while also improving selectivity of HCHO. MoO_3 can improve the selectivity of HCHO by eliminating Fe sites on the catalyst surface that are harmful to selective oxidation of CH_4. $FePO_x/SiO_2$ catalyst can increase the conversion rate of CH_4 to HCHO and selectivity towards HCHO. Based on previous literature studies, FMSA, FPSA and FPSP were prepared as candidate catalysts for the selective direct catalytic conversion of CH_4 to HCHO.

A fixed bed reactor is a type of chemical reactor where the reaction takes place on a fixed bed of catalyst particles[124, 125]. The bed consists of a packed bed of solid catalyst particles with a certain height. Gas or liquid reactants pass through the bed of particles, and the reaction occurs on the catalyst surface, generating products, thus realizing the process of heterogeneous catalytic reaction[18, 126]. The fixed bed reactor is one of the reactors used in the catalytic reaction experiments in this thesis and is used for initial screening of candidate catalysts.

This chapter mainly describes the performance evaluation of FMSA, FPSA, and FPSP catalysts in a fixed bed reactor. The influence of reaction temperature, pre-oxidation reaction, the amount of water introduced, oxygen partial pressure, and gas flow rate on the catalytic reaction were investigated. Additionally, the influence of catalyst size, catalyst support type, and loading amount on the catalytic process were examined. The experimental results of different catalysts and experimental parameters were analyzed in terms of CH_4 conversion, HCHO selectivity, and HCHO yield. The optimal experimental parameters were discussed, and catalyst materials with superior performance in the catalytic reaction were screened.

6.1 The influence of experimental parameters on the catalytic reaction

6.1.1 The influence of reaction temperature on the reaction

Due to the direct impact of reaction temperature on the redox activity of the catalyst, the performance of the catalyst varies at different temperatures. By increasing the experimental temperature of the catalytic reaction and examining the conversion of O_2 and CH_4 as well as the selectivity and yield of HCHO, the influence of experimental temperature on the catalytic reaction was observed. The performance of 13-FMSA and 8-FPSA catalysts at different catalytic reaction temperatures was shown in Table 6.1.

Table 6.1 The performance of catalysts at different reaction temperatures.

Experiment	Cat.	Temperature (°C)	Conversion (%)		Selectivity (%)	Yield (%)
			O_2	CH_4	HCHO	HCHO
6-1-1	13-FMSA	650	18.4	2.08	0.78	0.016
6-1-2		700	29.6	3.03	0.34	0.010
6-1-3	8-FPSA	600	0.32	0.04	29.9	0.012
6-1-4		650	4.16	0.76	6.88	0.053
6-1-5		700	21.48	3.88	1.27	0.049

0.6 g of 13-FMSA spherical catalyst was loaded into a fixed bed reactor with a diameter of 1 cm and a height of 8.5 cm. Other experimental parameters were kept constant, and the experiment was conducted at the same flow rate of 100 mL/min and the same CH_4/O_2 ratio of 10/1. When the reaction temperature was 350ºC and the reaction time was 90 min, no liquid was produced in the condenser, and the gas composition discharged as shown by GC indicated no significant gas conversion occurred throughout the experiment. Prior to the reaction experiment, the catalyst was subjected to a pre-oxidation reaction experiment, and no gas conversion was observed during the reaction experiment. When the reaction temperature was increased to 450°C and 550°C, some liquid was produced, but no CO_2 and CO signals were observed in GC. Partial liquid and CO_2 and CO were observed in GC when the experimental temperature was adjusted to 650°C and 700°C. The experimental results are shown in Table 6.1 and Fig. 6.1. The results showed that a higher HCHO selectivity and yield were obtained at 650°C, which was the preferred reaction temperature compared to 700°C for the two catalysts tested.

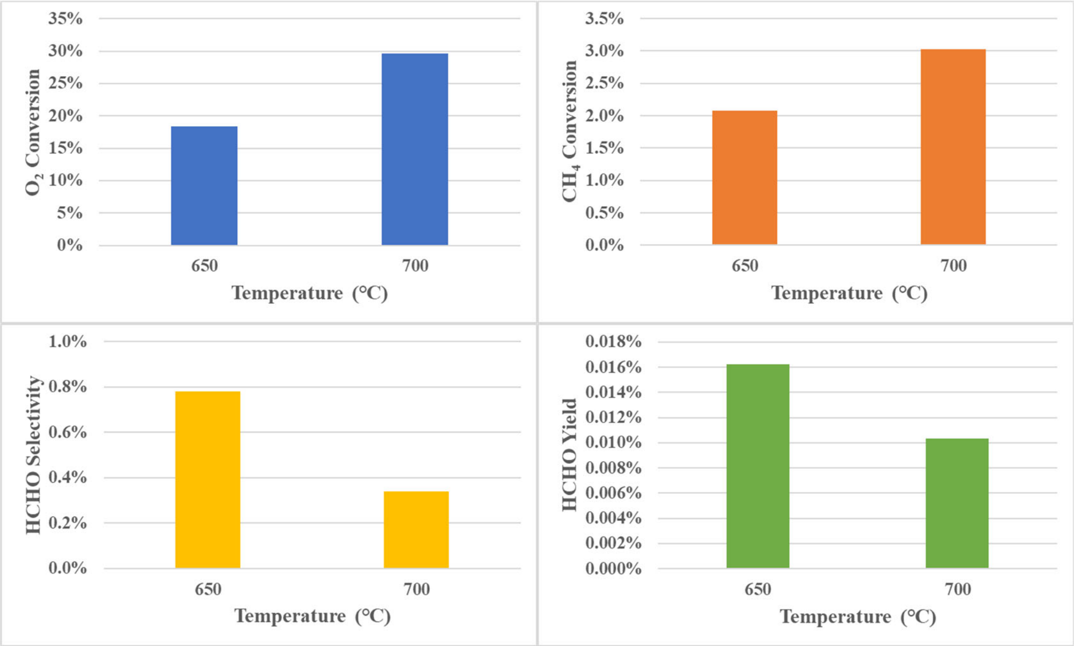

Fig. 6.1 The performance of the 13-FMSA catalyst at different temperatures.

Similarly, catalytic reaction tests were performed on the candidate catalyst material 8-FPSA. Keeping other experimental parameters constant, the experiments were carried out at the same flow rate of 130 mL/min and CH_4/O_2 ratio of 5/1, and the performance of spherical 8-FPSA catalyst material in direct catalytic oxidation of CH_4 to HCHO at temperatures of 600°C, 650°C, and 700°C was examined. The experimental results are presented in Table 6.1 and Fig. 6.2.

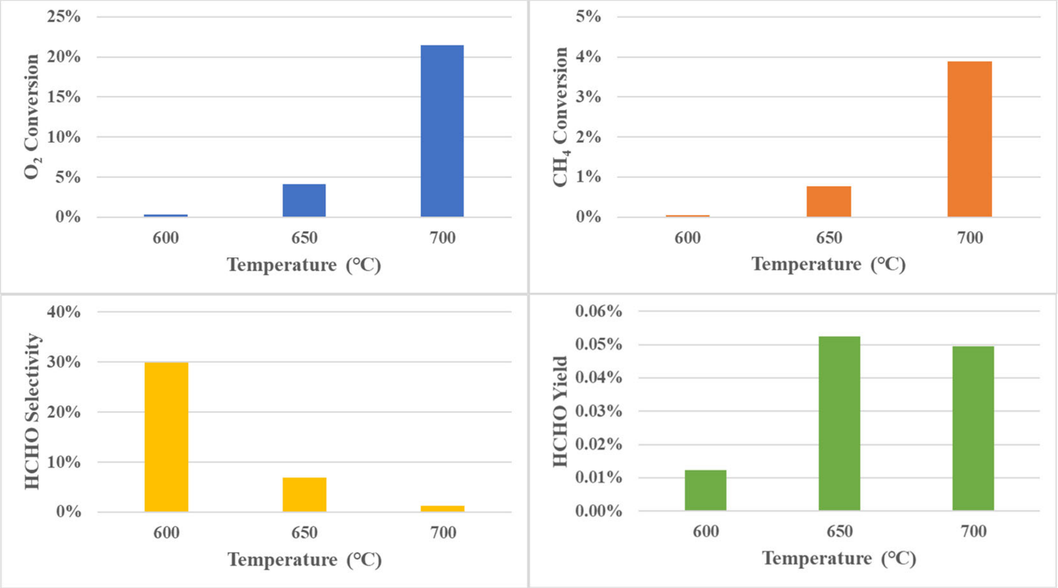

Fig. 6.2 The performance of the 8-FPSA catalyst at different temperatures.

The experimental results showed that as the temperature increased, the conversion of O_2 and CH_4 increased, while the selectivity of HCHO decreased. This was due to the acceleration of O_2 and CH_4 conversion at higher temperatures, which led to deeper oxidation of CH_4 and the generation of more CO_2 and CO. Both catalyst materials achieved the highest HCHO yield at 650°C. Therefore, in the examination of three catalytic reaction temperatures of 600°C, 650°C, and 700°C, the optimal reaction temperature was found to be 650°C. As a lower-loaded candidate catalyst, 8-FPSA had a much higher HCHO yield (0.053%) than 13-FMSA (0.016%) at a catalytic reaction temperature of 650°C. Thus, 650°C was chosen as the catalytic reaction temperature for subsequent catalytic reaction experiments with $FePO_x$ series catalysts.

6.1.2 The influence of pre-oxidation reaction on the reactions

In the catalytic reaction process, the role of the catalyst is to promote the oxidation reaction between CH_4 and O_2. Pre-oxidation reaction of the catalyst can increase the oxygen atom content on the catalyst surface. During the reaction experiment, the surface oxide of the catalyst interacts more with the reactants, promoting the occurrence of CH_4 oxidation reaction. Therefore, the pre-oxidation reaction step of the catalyst is an important factor that affects the performance of the catalyst in the catalytic reaction.

Based on the previous experimental results, 0.6 g of 8-FPSA catalyst was placed in a fixed bed reactor with a diameter of 1 cm. The reaction temperature was set at 650°C, and the heating rate during the experiment was 10 °C/min. The experiment was conducted with a flow rate of 130 mL/min and a CH_4/O_2 ratio of 10/1. The experiment variables were controlled for pre-oxidation reaction, and the influence of the pre-oxidation reaction step on the catalytic reaction was investigated. The results are presented in Table 6.2 and Fig. 6.3.

Table 6.2 The influence of pre-oxidation reaction of the 8-FPSA catalyst on the reaction experiments.

Experiment	Cat.	Pre-oxidation	Conversion (%)		Selectivity (%)	Yield (%)
			O_2	CH_4	HCHO	HCHO
6-2-1	8-FPSA	no	11.0	1.305	5.13	0.07
6-2-2		yes	13.1	1.567	5.28	0.08

Table 6.2 shows that after pre-oxidation reaction, the conversion of CH_4 increased, and the selectivity and yield of HCHO also increased to varying degrees. The experimental results are visually displayed in Fig. 6.3, which shows that pre-oxidation reaction of the catalyst before the start of the reaction not only improves the conversion of CH_4 in the catalytic reaction, but also enhances the selectivity and yield of HCHO. Therefore, it is recommended to perform pre-oxidation reaction of the candidate catalysts before the start of the subsequent catalytic reaction experiments, in order to improve the CH_4 conversion and HCHO yield of the catalytic reaction.

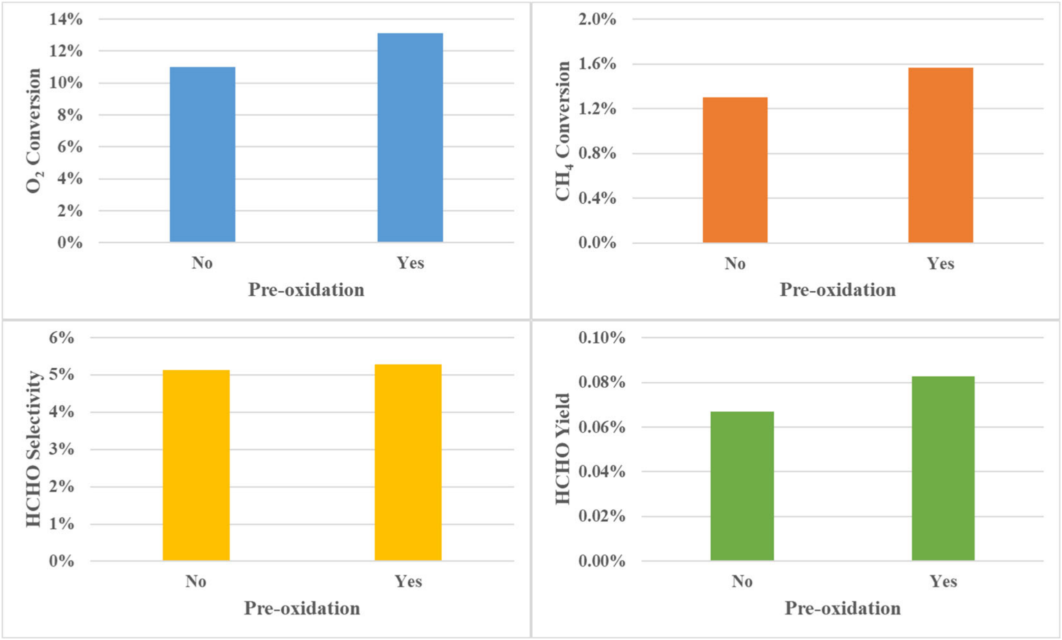

Fig. 6.3 The influence of pre-oxidation reaction of the 8-FPSA catalyst on the reaction experiments.

6.1.3 The influence of introduced water on the reactions

In 2020, Ping Liu et al. from Brookhaven National Laboratory (BNL) in the United States reported on a highly selective catalyst that converts CH_4 to methanol (~70%) and introduced the role of water in the reaction process[127]. The study demonstrated that introducing water is critical to achieving high selectivity for methanol production and that water primarily serves three functions. (1) Activation of CH_4 by breaking a C-H bond and converting CH_3 to methanol by providing an -OH group; (2) blocking reaction sites that could convert CH_4 and methanol to CO and CO_2; (3) promoting the transfer of methanol formed on the surface to the gas phase. The study showed that introducing water in direct catalytic oxidation of CH_4 can improve the selectivity for the target product and to reduce the deep oxidation of CH_4. Therefore, this chapter investigated the influence of the amount of water introduced during the catalytic reaction experiment on the reaction.

In this group of experiments, 8-FPSA was used as the catalyst, and the catalyst material was pre-oxidized for 30 min before the start of the catalytic reaction. The reaction temperature was set at 650°C with a heating rate of 10 °C/min. The experiments were conducted at a flow rate of 130 mL/min and a CH_4/O_2 ratio of 5/1, with the controlled variable being the amount of water introduced. Due to the limitations of the experimental apparatus, the highest amount of water molar fraction in the feed was 62%. Three different levels of water molar fraction in the feed were set at 15.5%, 31%, and 62%. The results are presented in Table 6.3 and Fig. 6.4.

Table 6.3 The influence of different water molar fraction in the feed on the 8-FPSA catalytic reaction experiments.

Experiment	Cat.	Water (%)	Conversion (%)		Selectivity (%)	Yield (%)
			O_2	CH_4	HCHO	HCHO
6-3-1	8-FPSA	15.5	4.18	0.76	7.39	0.0563
6-3-2		31	3.77	0.72	10.49	0.0754
6-3-3		62	4.36	0.84	10.44	0.0877

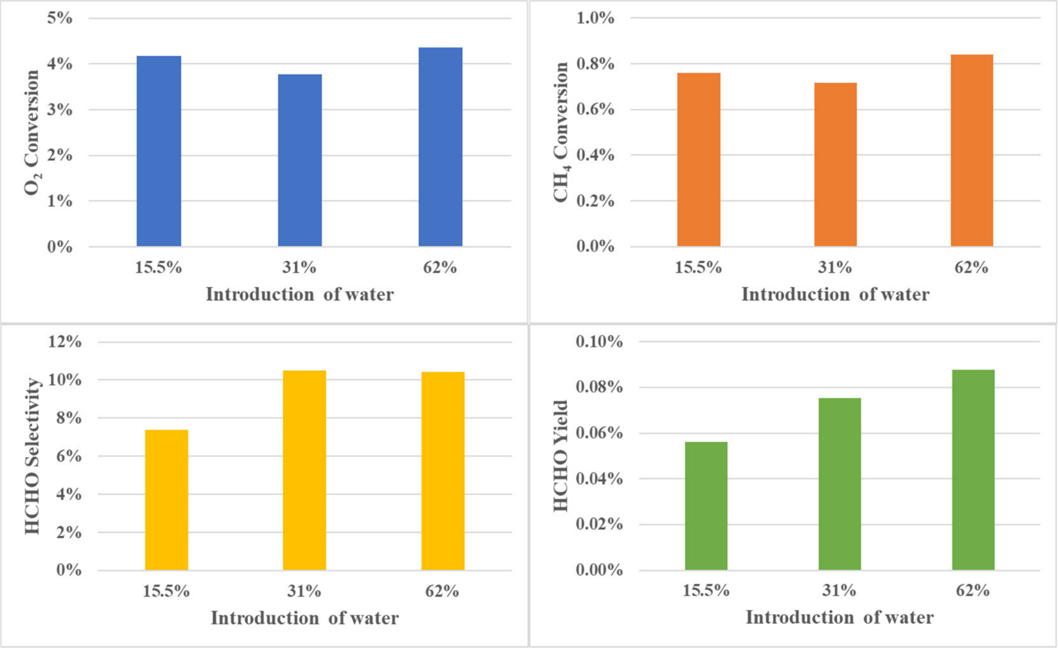

Fig. 6.4 The influence of different water molar fraction in the feed on the 8-FPSA catalytic reaction experiments.

Table 6.4 The influence of different water molar fraction in the feed on the 4-FPSA catalytic reaction experiments.

Experi-ment	Cat.	Water (%)	Flow rate (mL/min)	Conversion (%)		Selectivity (%)	Yield (%)
				O_2	CH_4	HCHO	HCHO
6-4-1	4-FPSA	62	97.5	1.87	0.79	10.38	0.0817
6-4-2			130	1.17	0.50	18.60	0.0930
6-4-3			162.5	0.80	0.38	25.40	0.0971
6-4-4		31	97.5	1.56	0.62	13.32	0.0827
6-4-5			130	1.09	0.47	18.32	0.0867
6-4-5			162.5	0.35	0.12	62.51	0.0769

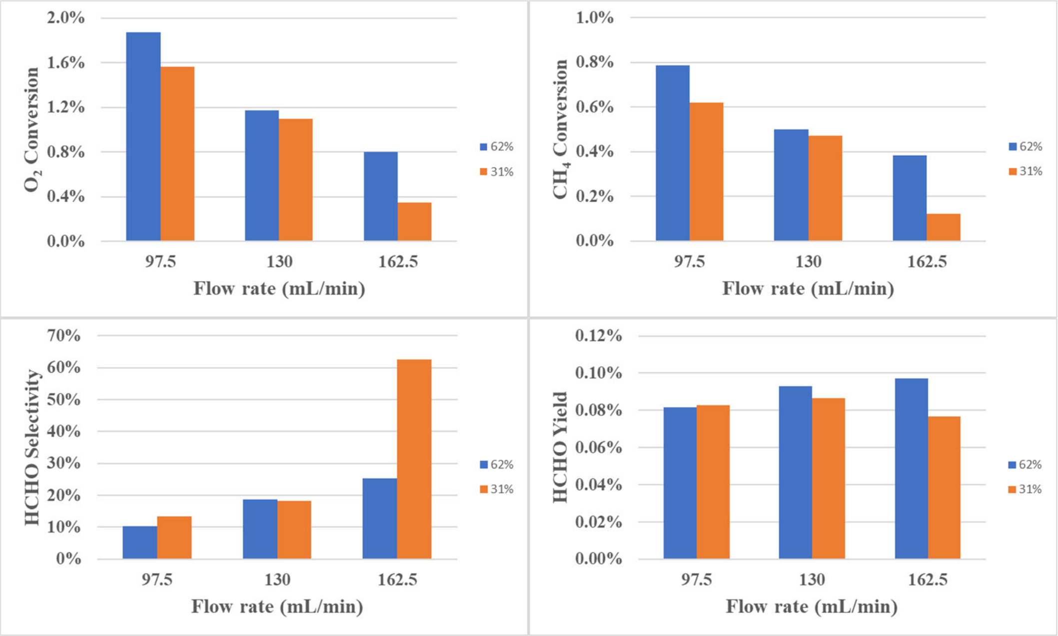

Fig. 6.5 The influence of different water molar fraction in the feed on the 4-FPSA catalytic reaction experiments.

The results in Table 6.3 and Fig. 6.4 show that with the increase of the amount of introduced water, the conversion shows a trend of first decreasing and then increasing, while the selectivity of HCHO shows a trend of first increasing and then decreasing slightly, the yield of HCHO gradually increases. When the amount of water molar fraction in the feed is 31%, the selectivity of HCHO is the highest during the experimental process, but the conversion of O_2 and CH_4 are relatively low. When the amount of water molar fraction in the feed is increased to 62%, the conversion is higher. The highest HCHO yield can be obtained when the amount of introduced water during the experimental process is 62%.

Subsequently, 4-FPSA among the candidate catalysts was placed in a fixed bed reactor to investigate the influence of the amount of water molar fraction in the feed on the catalytic reaction. The results are shown in Table 6.4 and Fig. 6.5.

As shown in Fig. 6.5, it can be observed that as the flow rate increases, the conversion of O_2 and CH_4 decrease, while the selectivity of HCHO increases. In this set of experiments, when the amount of water molar fraction in the feed was 31% and the flow rate was 162.5 mL/min, no significant CO data was observed during GC analysis of the reaction products. Therefore, the calculated conversion of O_2 and CH_4 as well as the selectivity of HCHO obtained from the 6-4-5 experiment are inaccurate. Compared to the water introduced of 31%, the water introduced of 62% resulted in higher conversion of O_2 and CH_4, as well as higher HCHO yield.

The catalytic reaction experiments involving 8-FPSA and 4-FPSA catalysts consistently demonstrated that a higher yield of HCHO was obtained by introducing 62% of water compared to 15.5% and 31% of water during the experiment.

6.1.4 The influence of flow rate and oxygen partial pressure on the reaction

In the direct catalytic oxidation of CH_4 experiment, the flow rate and oxygen partial pressure in the reaction gas directly influence the catalytic reaction. Here, a reaction temperature of 650°C was employed with a heating rate of 10 °C/min. The amount of water molar fraction in the feed was 62% as a constant parameter. The variables investigated were the flow rate and the oxygen partial pressure in the reaction gas. The performance of the 4-FPSA catalyst was examined under different gas flow rates, and the impact of varying oxygen partial pressures in the reaction gas was studied. The experimental results of the catalytic reaction using the 4-FPSA catalyst are presented in Table 6.5, Fig. 6.6 and Fig. 6.7 for comparison and analysis.

Table 6.5 The performance of the 4-FPSA catalyst under different flow rates and oxygen partial pressures.

Experiment	Cat.	CH_4/O_2	Flow rate (mL/min)	Conversion (%)		Selectivity (%)	Yield (%)
				O_2	CH_4	HCHO	HCHO
6-5-1	4-FPSA	R5 5/1	97.5	3.28	0.72	13.92	0.0997
6-5-2			130	1.54	0.39	17.25	0.0671
6-5-3			162.5	1.37	0.35	24.02	0.0842
6-5-4		R3 3/1	97.5	1.87	0.79	10.38	0.0817
6-5-5			130	1.17	0.50	18.60	0.0930
6-5-6			162.5	0.80	0.38	25.40	0.0971
6-5-7		R1 1/1	130	0.74	1.11	9.30	0.1036
6-5-8			162.5	0.47	0.73	14.31	0.1042
6-5-9			195	0.33	0.57	17.74	0.1015

This group of experiments investigated the performance of the 4-FPSA catalyst under different flow rates (97.5, 130, 162.5, and 195 mL/min) and CH_4/O_2 ratios (5/1, 3/1, and 1/1). The experimental results demonstrated that both the flow rate and oxygen partial pressure had an impact on the experimental outcomes, including the conversion of O_2 and CH_4, as well as the selectivity and yield of HCHO.

With increasing flow rate, the conversion of O_2 and CH_4 exhibited a decreasing trend, while the selectivity of HCHO increased. This can be attributed to the shorter residence time of reactants on the catalyst surface due to the accelerated gas flow rate, resulting in lower conversion and reduced deep oxidation of CH_4 during the reaction, thereby enhancing the selectivity of HCHO. For CH_4/O_2 ratios of 5/1 and 3/1, when the flow rate exceeded 162.5 mL/min, no data for CO and CO_2 were observed in the discharged gas, and therefore, experimental data for flow rates higher than 162.5 mL/min were not recorded. Among the completed experiments, the one conducted at a flow rate of 162.5 mL/min achieved a higher HCHO yield.

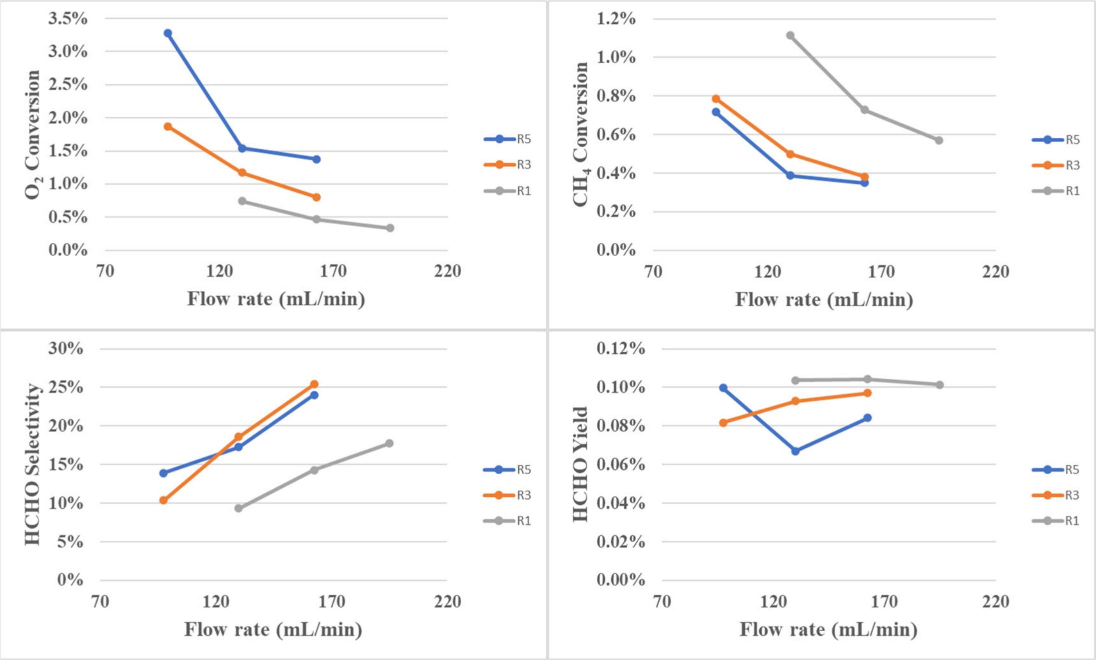

Fig. 6.6 The performance of the 4-FPSA catalyst under different flow rates and oxygen partial pressures.

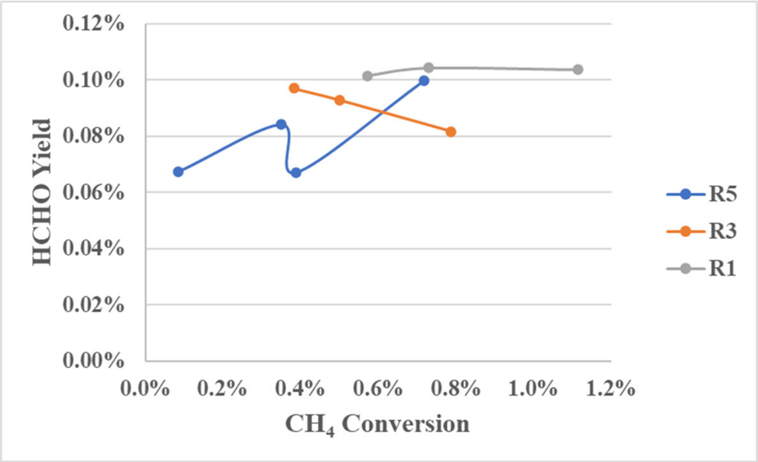

Fig. 6.7 The trends of CH_4 conversion and HCHO yield for the 4-FPSA catalyst.

Comparing the experimental results at different oxygen partial pressures, it can be observed that an increase in oxygen partial pressure leads to a decrease in O_2 conversion and an increase in CH_4 conversion. When the CH_4/O_2 ratio is 1/1, the HCHO yield at various flow rates remains at a relatively high level.

Fig. 6.7 illustrates the trends in CH_4 conversion and HCHO yield for the 4-FPSA catalyst. It can be observed that when the CH_4/O_2 ratio is 1/1, both the CH_4 conversion and HCHO yield exhibit significant advantages.

The performance of the 4-FPSP catalyst with different supports was investigated under various gas flow and oxygen partial pressures. The catalytic reaction experiments were conducted at a temperature of 650°C with a heating rate of 10 °C/min. The amount of water molar fraction in the feed was 62%, while the flow rate and oxygen partial pressure were controlled as variables. The experimental results are presented and compared in Table 6.6, Fig. 6.8 and Fig. 6.9.

Table 6.6 The performance of the 4-FPSP catalyst under different gas flow rates and oxygen partial pressures.

Experiment	Cat.	CH_4/O_2	Flow rate (mL/min)	Conversion (%)		Selectivity (%)	Yield (%)
				O_2	CH_4	HCHO	HCHO
6-6-1	4-FPSP	R5 5/1	97.5	27.84	3.13	0.76	0.0237
6-6-2			130	17.18	2.03	1.45	0.0296
6-6-3			162.5	12.84	1.59	5.58	0.0888
6-6-4		R3 3/1	97.5	16.82	3.59	3.26	0.1172
6-6-5			130	12.65	2.83	4.16	0.1180
6-6-6			162.5	7.80	1.77	6.93	0.1225
6-6-7		R1 1/1	97.5	9.95	8.43	1.70	0.1435
6-6-8			130	6.38	5.73	3.14	0.1799
6-6-9			162.5	4.34	3.96	4.77	0.1887
6-6-10			195	3.35	3.07	5.86	0.1797
6-6-11			227.5	2.67	2.39	4.56	0.1091

The results showed that similar to the performance of the 4-FPSA catalyst, an increase in flow rate led to a decrease in the conversion of O_2 and CH_4, while the selectivity of HCHO gradually increased. In the completed experiments, higher HCHO yield were observed at a flow rate of 162.5 mL/min. Furthermore, an increase in oxygen partial pressure resulted in a decrease in O_2 conversion and an increase in CH_4 conversion, with the highest HCHO yield obtained at a CH_4/O_2 ratio of 1/1.

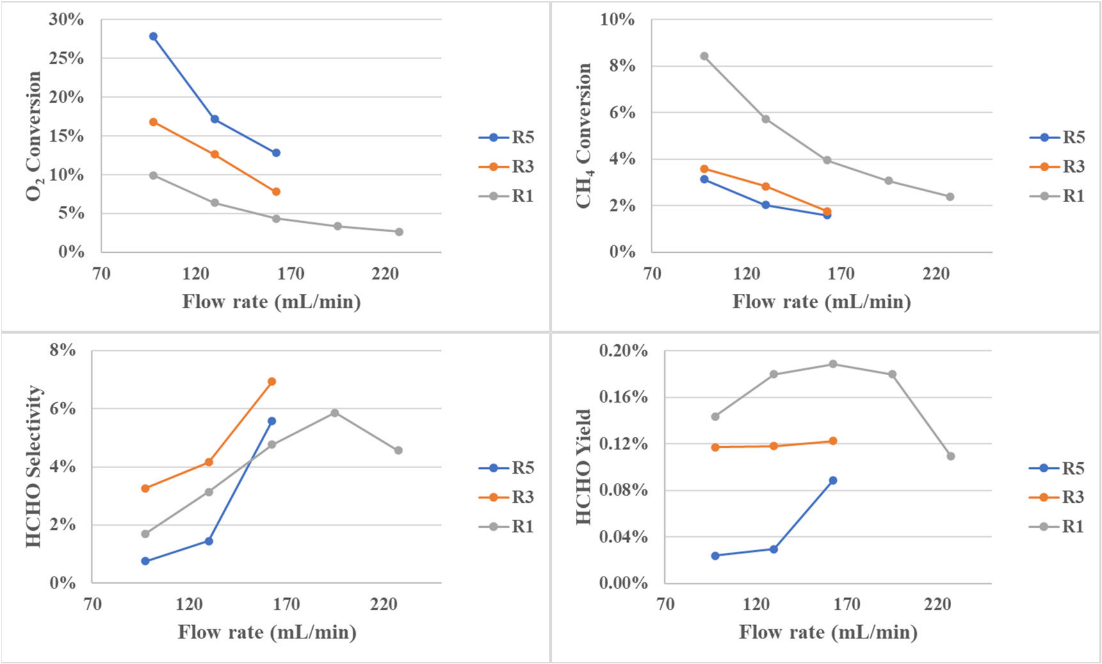

Fig. 6.8 The performance of the 4-FPSP catalyst under different flow rates and oxygen partial pressures.

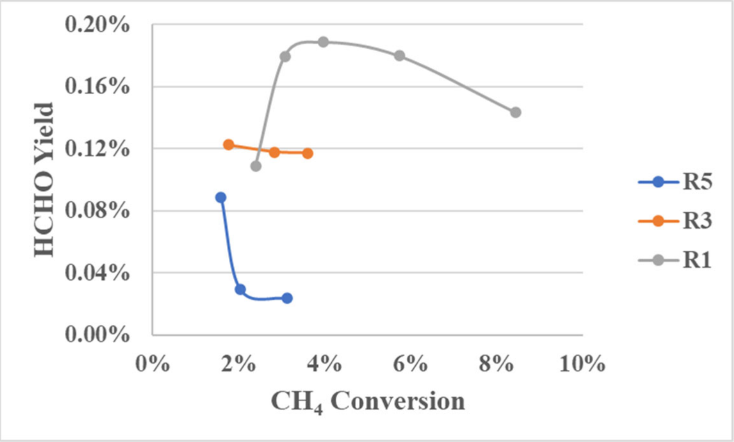

Fig. 6.9 The trends in CH_4 conversion and HCHO yield for the 4-FPSP catalyst.

The trend is clearly observed in Fig. 6.9, where the HCHO yield at CH_4/O_2 ratio of 1/1 (R1) is significantly higher compared to the experiments with oxygen partial pressures of 5/1 (R5) and 3/1 (R3). Correspondingly, the CH_4 conversion of CH_4/O_2 ratio of 1/1 also falls within a higher range.

The experimental results demonstrate that the 4-FPSP catalyst, with the same loading amount as 4-FPSA, exhibits similar trends in CH_4 conversion and selectivity and yield of HCHO. Considering the previous findings that lower loading amounts of catalysts seem to favor higher selectivity, further investigations were conducted using the 2-FPSP catalyst with an even lower loading amount. The catalytic performance of the 2-FPSP catalyst was evaluated under various flow rates and CH_4/O_2 ratios in a fixed bed reactor. The experimental conditions included a reaction temperature of 650°C with a heating rate of 10 °C/min, a water molar fraction in the feed of 62%, and controlled variables of gas flow rate and oxygen partial pressure. The experimental data and comparative results are presented in Table 6.7, Fig. 6.10 and Fig. 6.11.

Table 6.7 The performance of the 2-FPSP catalyst under different flow rates and oxygen partial pressures.

Experiment	Cat.	CH_4/O_2		Flow rate (mL/min)	Conversion (%)		Selectivity (%)	Yield (%)
					O_2	CH_4	HCHO	HCHO
6-7-1	2-FPSP	R5	5/1	97.5	10.92	1.45	4.61	0.0667
6-7-2				130	5.70	0.85	8.93	0.0761
6-7-3				162.5	3.69	0.61	12.92	0.0789
6-7-4		R3	3/1	97.5	5.23	1.50	7.82	0.1173
6-7-5				130	3.50	1.04	12.96	0.1345
6-7-6				162.5	2.68	0.84	14.26	0.1191
6-7-7		R1	1/1	97.5	3.23	3.84	3.71	0.1425
6-7-8				130	1.82	2.21	5.34	0.1183
6-7-9				162.5	1.27	1.56	9.20	0.1437
6-7-10				195	1.02	1.30	8.00	0.1037
6-7-11				227.5	0.77	1.00	9.18	0.0916

The experimental results demonstrate similar trends in the conversion of O_2 and CH_4 and the selectivity of HCHO compared to the previous two catalysts. As the flow rate increases, the conversion of O_2 and CH_4 decrease, while the HCHO selectivity shows an overall increasing trend. The catalytic reaction performed at a flow rate of 162.5 mL/min exhibited higher HCHO yield. Under different CH_4/O_2 ratios, an increase in oxygen partial pressure provides an ample oxygen environment for the oxidation of CH_4, resulting in an increased CH_4 conversion. When the CH_4/O_2 ratio was 5/1 and 3/1, the quantities of CO and CO_2 in the outlet products could not be detected in catalytic reactions with flow rates higher than 162.5 mL/min. The trends in CH_4 conversion and HCHO yield are more clearly illustrated in Fig. 6.11. Compared to the R3 and R1 experiments, the catalytic experiment with a CH_4/O_2 ratio of 1/1 (R1) achieved higher CH_4 conversion and HCHO yield. The highest HCHO yield was obtained in the experiment with a flow rate of 162.5 mL/min.

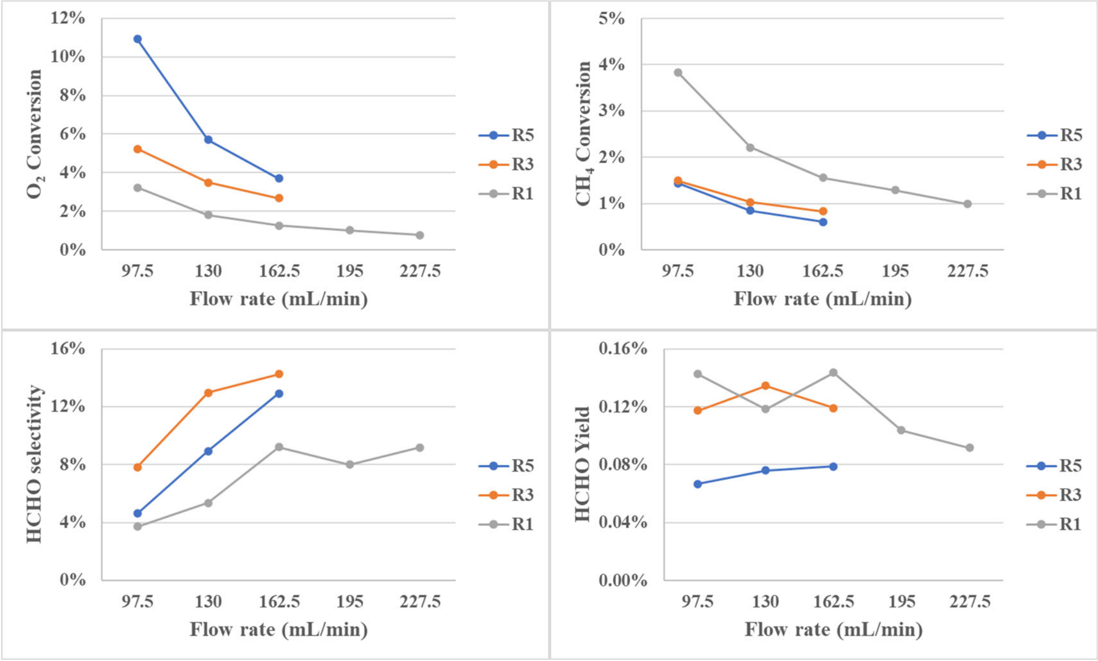

Fig. 6.10 The performance of the 2-FPSP catalyst under different flow rates and oxygen partial pressures.

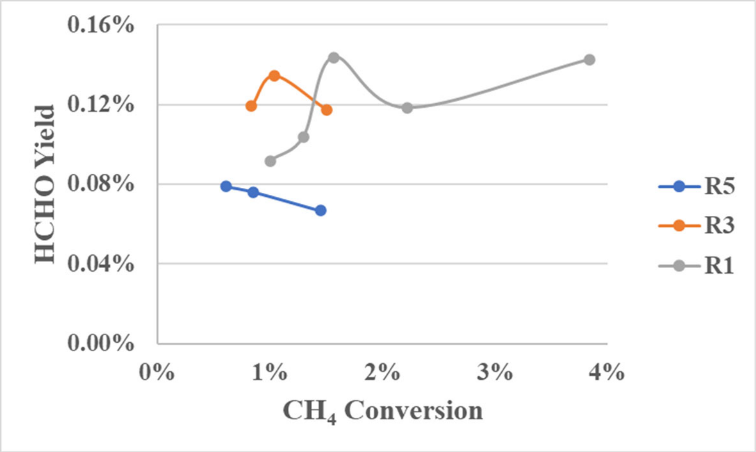

Fig. 6.11 The trends in CH_4 conversion and HCHO yield for the 2-FPSP catalyst.

This section discusses the manipulation of experimental parameters in catalytic reaction experiments, including the influence of different catalysts, reaction temperatures, pre-oxidation reaction, amount of water introduced, flow rates and oxygen partial pressures. Based on the discussions, it was determined that conducting catalytic reaction experiments at a temperature of 650°C, pre-oxidizing the catalyst before the start of the experiments, water molar fraction in the feed of 62%, using a flow rate of 162.5 mL/min, and CH_4/O_2 ratio of 1/1 resulted in higher HCHO yields.

6.2 The influence of catalyst types on the catalytic reaction

6.2.1 The influence of catalyst size on the reaction

It is well known that the size of the catalyst plays a significant role in the catalytic reaction process, as it affects the contact area between the reactant gases and the catalyst, thereby influencing the CH_4 conversion and HCHO selectivity. In the previous catalytic reaction experiments, spherical aerogel composite materials were used as catalysts in a fixed bed reactor. Here, the influence of catalyst size on the catalytic reaction was investigated. The spherical catalyst 8-FPSA was crushed and sieved to retain composite materials within the size range of 160~315 μm (Fig. 6.12 (b)) for use as catalysts in the fixed bed reactor for catalytic reaction testing.

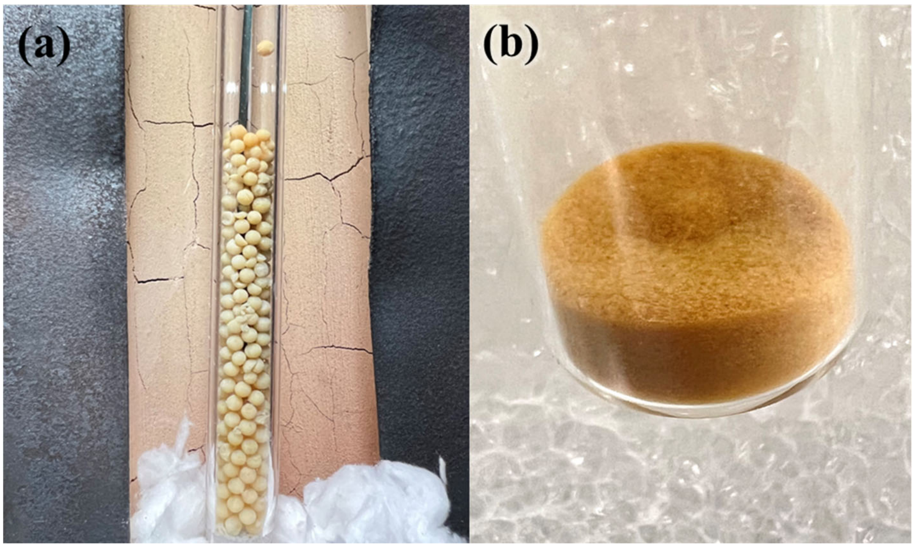

Fig. 6.12 The performance of 8-FPSA catalysts with different sizes: (a) 2-3 mm and (b) 160~315 μm.

The catalytic reaction experiments were conducted at a temperature of 650°C with a heating rate of 10 °C/min. Prior to the reaction, the 8-FPSA catalyst material was subjected to pre-oxidation reaction. The reactant gas contained 62% water. The variable controlled was the different sizes of the catalyst. The experimental results are presented in Table 6.8 and Fig. 6.13.

Table 6.8 The performance of 8-FPSA catalysts with different sizes in the catalytic reaction.

Experiment	Cat.	Catalysts sizes	Conversion (%)		Selectivity (%)	Yield (%)
			O_2	CH_4	HCHO	HCHO
6-8-1	8-FPSA	2~3 mm	16.07	1.93	4.58	0.0885
6-8-2		160~315μm	18.42	2.15	4.14	0.0890

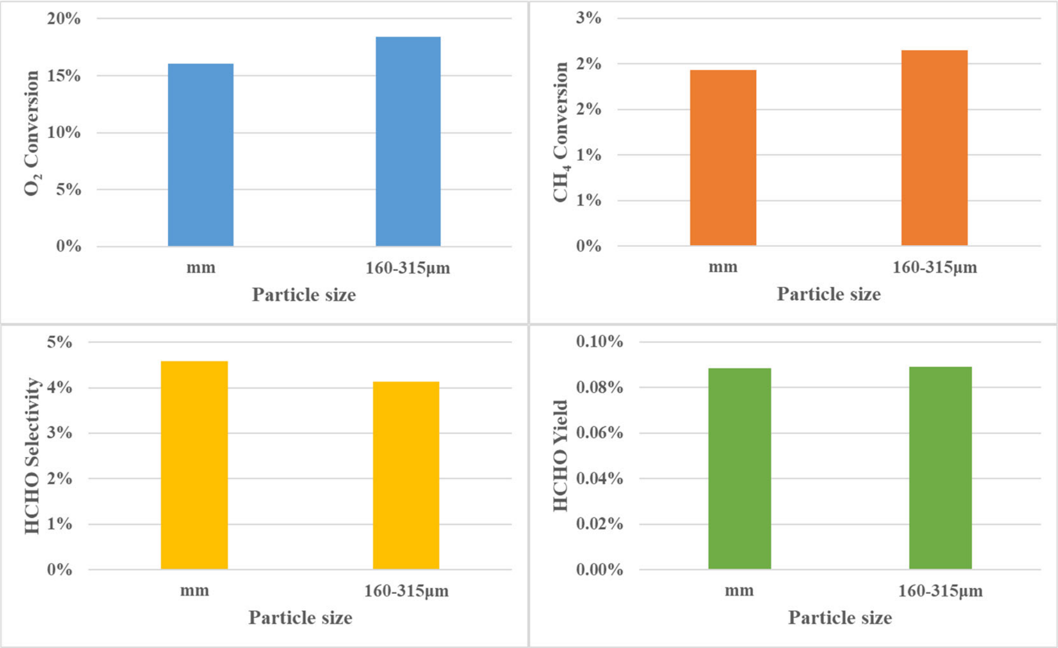

Fig. 6.13 The performance of 8-FPSA catalysts with different sizes in the catalytic reaction.

The experimental results showed that compared to the millimeter-sized catalyst, the catalyst with a size range of 160~315 μm exhibited higher O_2 and CH_4 conversion but lower HCHO selectivity in the catalytic reaction. This can be attributed to the increased direct contact area between the catalyst and the reactant gas when the catalyst size is reduced, allowing for more efficient interaction and reaction between the gas and the active components in the catalyst. However, while promoting CH_4 conversion, the increased contact area also intensifies the occurrence of deep oxidation reactions, leading to a higher generation of CO and CO_2 and consequently reducing the HCHO selectivity. Calculation results indicated that the catalyst with a size range of 160~315 μm achieved higher HCHO yields.

Subsequently, the lower-loaded 4-FPSA catalyst with reduced particle size was obtained by crushing and sieving, targeting the size range of 160~315 μm, as shown in Fig. 6.14. However, it was observed that the small-sized 160~315 μm catalyst adhered to the metal sieve, making it difficult to collect and therefore the small size 4-FPSA could not be tested for catalytic reactions.

Fig. 6.14 The sieving of 4-FPSA catalyst.

6.2.2 The influence of catalyst supports on the reaction

Table 6.9 The performance of catalysts 4-FPSA and 4-FPSP with different supports in the reaction experiments.

Experi-ment	Cat.	CH_4/O_2	Flow rate (mL/min)	Conversion (%)		Selectivity (%)	Yield (%)
				O_2	CH_4	HCHO	HCHO
6-9-1	4-FPSA	1/1	130	0.74	1.11	8.91	0.0993
6-9-2			162.5	0.47	0.73	14.31	0.1042
6-9-3			195	0.33	0.57	17.18	0.0983
6-9-4	4-FPSP	1/1	97.5	9.95	8.43	1.70	0.1435
6-9-5			130	6.38	5.73	3.14	0.1799
6-9-6			162.5	4.34	3.96	4.77	0.1887
6-9-7			195	3.35	3.07	5.86	0.1797
6-9-8			227.5	2.67	2.39	4.56	0.1091

In the previous experimental discussions, the performance of different catalysts under various experimental parameters was examined. It was observed that the series of composite catalysts (FPSA) with SiO_2 aerogel as the support and the series of composite catalysts (FPSP) with SiO_2 precipitate as the support exhibited some differences in catalytic oxidation of CH_4, despite having the same active component loading. The catalyst support plays a crucial role in the catalyst system, providing a suitable bed for the deposition of active components and determining the internal structure of the catalyst.

Here, a catalytic reaction experiment was conducted at 650°C with a heating rate of 10 °C/min, using the CH_4/O_2 ratio (5/1) and varying flow rates, water molar fraction in the feed was 62%. The performance of the catalysts with different supports, 4-FPSA and 4-FPSP, was investigated in terms of CH_4 and O_2 conversion, selectivity and yield of HCHO. The results are presented in Table 6.9 and Fig. 6.15.

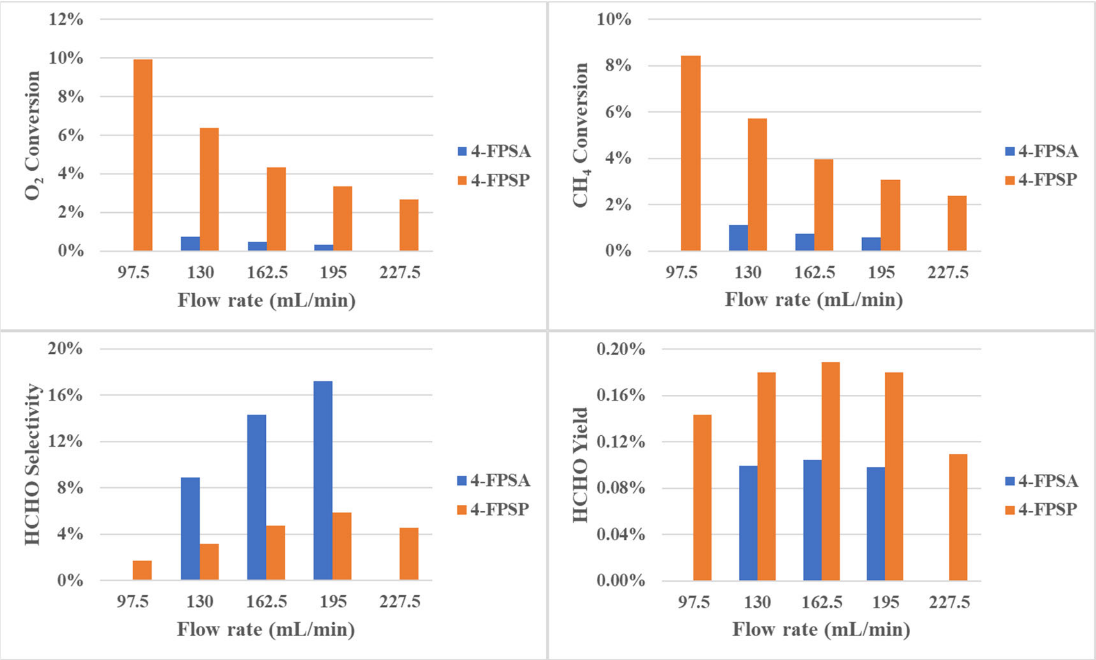

Fig. 6.15 The performance of catalysts 4-FPSA and 4-FPSP with different supports in the catalytic reaction experiments.

The results in Fig. 6.15 demonstrate that under the CH_4/O_2 ratio of 1/1, as the flow rate increases, the conversion of CH_4 and O_2 decrease. In the 4-FPSP catalyst, the selectivity of HCHO initially increases and then decreases. Compared to the 4-FPSA catalyst, the 4-FPSP catalyst exhibits higher conversion of CH_4 and O_2. This can be attributed to the fact that in the 4-FPSP catalyst with SiO_2 precipitate as the support, a large amount of active components is dispersed on the support surface, allowing for enhanced contact and reaction with the reactant gases, thus promoting the catalytic reaction and increasing the conversion of CH_4 and O_2. However, this promotion of the catalytic reaction also intensifies the deep oxidation of CH_4, resulting in the generation of more CO and CO_2, leading to a lower selectivity of HCHO in the 4-FPSP catalyst. The highest HCHO yield is obtained at a flow rate of 162.5 mL/min.

6.2.3 The influence of catalyst loading on the reaction

As it is well known, the catalyst loading directly affects catalytic activity. Basic characterization of the materials reveals differences in the redox ability and active temperature range of catalysts with different loading levels within the same series. Catalysts with lower loading levels appear to exhibit superior redox ability. Previous catalytic experiments have provided relevant data highlighting these differences.

Table 6.10 The performance of catalysts 4-FPSP and 2-FPSP with different loading in the reaction experiments.

Experiment	Cat.	CH_4/O_2	Flow rate (mL/min)	Conversion (%)		Selectivity (%)	Yield (%)
				O_2	CH_4	HCHO	HCHO
6-10-1	4-FPSP	1/1	97.5	9.95	8.43	1.70	0.1435
6-10-2			130	6.38	5.73	3.14	0.1799
6-10-3			162.5	4.34	3.96	4.77	0.1887
6-10-4			195	3.35	3.07	5.86	0.1797
6-10-5			227.5	2.67	2.39	4.56	0.1091
6-10-6	2-FPSP	1/1	97.5	3.23	3.84	3.71	0.1425
6-10-7			130	1.82	2.21	5.34	0.1183
6-10-8			162.5	1.27	1.56	9.20	0.1437
6-10-9			195	1.02	1.30	8.00	0.1037
6-10-10			227.5	0.77	1.00	9.18	0.0916

Here, a comparison was made between the well-performing catalyst 4-FPSP and 2-FPSP with even lower loading level, regarding their performance in the catalytic reaction. The reaction experiments were conducted at 650℃ with a heating rate of 10 ℃/min, under a CH_4/O_2 ratio of 1/1 and different flow rates, while introducing 62% water. The conversion of CH_4 and O_2, as well as the selectivity and yield of HCHO were examined for both 4-FPSP and 2-FPSP catalysts. The results are presented in Table 6.10 and Fig. 6.16.

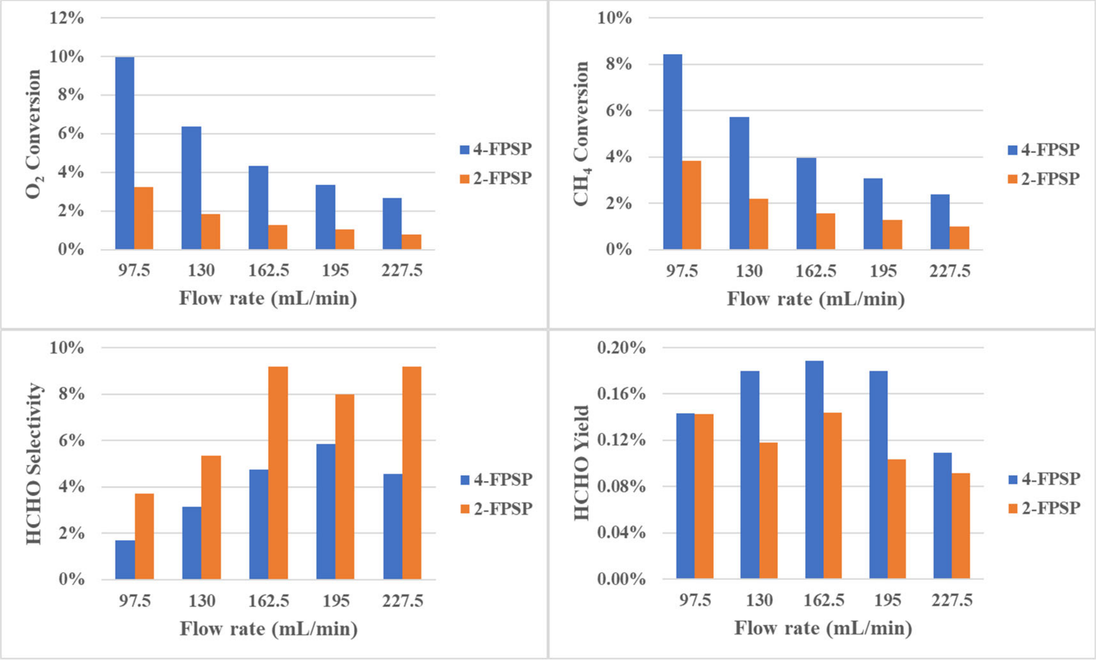

Fig. 6.16 The performance of catalysts 4-FPSP and 2-FPSP with different loading amounts in the reaction experiments.

The comparative results depicted in Fig. 6.16 demonstrate a gradual decrease in the conversion of both CH_4 and O_2 with increasing flow rate, accompanied by an initial increase and subsequent decrease in HCHO selectivity. The catalyst 4-FPSP exhibits higher conversion for CH_4 and O_2 compared to the 2-FPSP catalyst, while the 2-FPSP catalyst shows higher selectivity of HCHO. These findings are consistent with the previous discussion, where it was established that the dispersion of active components in catalysts with lower loading contributes to improved selectivity of the target product. However, due to the significantly higher CH_4 conversion achieved by the higher-loaded catalyst 4-FPSP, calculations indicate that the 4-FPSP catalyst exhibits a higher HCHO yield. The highest HCHO yield was obtained by the 4-FPSP catalyst at a gas flow rate of 162.5 mL/min.

This section discusses the impact of different catalysts on the catalytic reaction, specifically investigating the influence of catalyst size, catalyst support, and active component loading on the performance in catalytic reaction experiments. Through experimental discussions, it is evident that reducing the catalyst size improves the conversion of CH_4 in the catalytic reaction. Compared to the SiO_2 aerogel-based catalyst, the catalyst supported on SiO_2 precipitate exhibits higher CH_4 conversion. The results showed that catalysts with sizes of 160~315 μm and 4-FPSP with SiO_2-precipitated catalyst support obtained high yields of HCHO in the catalytic reactions.

6.3 Chapter summary

Based on the advantages of SiO_2 as a catalyst support and Fe-MoO_x and $FePO_x$ as active components, this chapter investigates the performance of SiO_2-based composite materials containing Fe-MoO_x and $FePO_x$ as candidate catalysts for the selective direct catalytic oxidation of CH_4 to HCHO in a fixed bed reactor. The influence of reaction temperature, pre-oxidation reaction, water introduction, oxygen partial pressure, and flow rate on the catalytic reaction were examined, along with the performance variations of catalysts with different sizes, different support types, and different loading amounts in the catalytic reaction. The CH_4 conversion, HCHO selectivity and HCHO yield in the catalytic reaction were analyzed based on the experimental results. The conclusions are as follows：

(1) Catalytic reaction experiments conducted at 650°C, pre-oxidation of the catalyst before the start of the experiment, a water molar fraction in the feed of 62%, a reaction flow rate of 162.5 mL/min and a CH_4/O_2 ratio of 1/1 were able to achieve higher yields of HCHO.

(2) Based on the experimental and result analysis, it was found that the catalyst 4-FPSP with a size range of 160~315 μm and SiO_2 precipitate as the support exhibited higher HCHO yield in the catalytic oxidation of CH_4.

In the series of experiments aiming at the selective direct catalytic oxidation of CH_4 in a fixed bed reactor, preliminary tests were conducted to screen the candidate catalysts. In subsequent catalytic reaction experiments, the optimal experimental parameters from this chapter will be referenced to investigate the performance of selective direct catalytic oxidation of CH_4 under different experimental conditions using the catalyst in a fluidized-bed reactor.

Chapter 7 Performance of catalyst selective catalytic oxidation of methane in fluidized bed reactor

In a catalytic reaction, there is no relative motion between the solid particles when the reaction gas flows through the reactor bed at a low flow rate, the bed is a fixed bed. By further increasing the gas flow rate, the power and buoyancy brought by the gas to the particles exceeds the effect of gravity of the solid particles, which are in a state of constant flow and agitation and have the characteristics of a flowing liquid, a state known as fluidization.

A fluidized bed is a type of bed in which solid particles exhibit a fluid-like state within a reactor due to the action of gas flow. The operation of a fluidized bed reactor (FBR) relies on the dynamic behavior and mass transfer properties of the fluidized bed. Catalyst particles are placed inside the reactor, and the reactant gas enters from the bottom. The bed, composed of catalyst particles, forms a fluidized bed layer where the gas continuously agitates and flows, facilitating physical adsorption, surface diffusion, and catalytic chemical reactions. The reaction products detach from the catalyst surface and are promptly discharged from the outlet, while the catalyst particles re-engage in the reaction cycle, enabling the continuous progress of the catalytic reaction. Compared to fixed bed reactors, FBR offer several distinct advantages: the thorough mixing of catalyst particles in a fluidized state enables efficient heat and mass transfer; the uniform mixing of catalyst and reactant gas achieves process uniformity; the free movement of catalyst particles in the fluidized bed minimizes the risk of reactor blockage.

Gas-phase catalytic oxidation reactions are typically performed by mixing the reactants with oxygen and other inert dilution gases and passing the mixture together into the reactor. And in some cases, the process can be divided into two steps. The catalyst serves as a support for oxygen storage and supply. In the first step, the catalyst is reduced during the reaction with the reactant gas. In the second step, oxidation occurs as the catalyst mixes with the oxygen containing gas. During this process, the reduction of gaseous oxygen can enhance the selectivity of the target product to a certain extent. In conventional reactors, these two steps can be conducted sequentially in separate reactors, or the catalyst can be continuously transferred between the two reactors, thus providing steady-state operation. However, a two-zone fluidized bed reactor (TZFBR) provides a continuous operating reaction system for this reaction mode, but in a single reactor.

This chapter presents the performance of selected catalyst candidates in two different types of reactors, FBR and TZFBR. The investigation includes examining the minimum fluidization velocity, issues and improvements, the influence of catalyst size, oxygen partial pressure, and gas flow rate on catalytic reactions in FBR. Furthermore, the influence of experimental process parameters such as catalyst support, CH_4 introduction point, inert diluent gas introduction, and flow rate on catalytic reactions in TZFBR are explored. The performance in different reactors is compared and the influence of the experimental process and experimental parameters on the catalytic reaction is discussed. Analysis of experimental results of catalytic reactions under different experimental parameters including conversion of CH_4, selectivity and yield of HCHO.

7.1 Performance of catalyst in fluidized bed reactors

7.1.1 Testing of minimum fluidization velocity

The minimum fluidization velocity (U_{mf}) refers to the apparent linear velocity of a fluid at which the solid catalyst particles in a bed transition from a static state to a fluidized state. It is the point at which the upward drag force exerted by the fluid equals the weight of the particle bed. U_{mf} depends on factors such as the density, size, and shape of the solid particles, as well as the density and viscosity of the gas. The calculation of U_{mf} aims to determine the minimum gas flow rate required to initiate and maintain the suspension of solid catalyst particles in a fluidized bed, ensuring their proper fluidization and preventing issues like clogging.

Table 7.1 U_{mf} testing record.

Flow rate (ml/min)	Linear velocity (cm/min)	ΔP Ascendant (cm water column)	ΔP descendant (cm water column)	ΔP (cm H_2O)	ΔP (Pa)
500	89.9	0.65	0.6	0.88	0.6
250	45.1	0.6	0.6	0.88	0.6
200	36.0	0.6	0.6	0.88	0.6
150	27.0	0.6	0.6	0.88	0.6
130	23.4	0.6	0.6	0.88	0.6
110	19.9	0.6	0.55	0.88	0.6
90	16.2	0.6	0.5	0.88	0.5
70	12.6	0.6	0.45	0.88	0.5
50	9.1	0.6	0.4	0.88	0.4
40	7.1	0.5	0.35	0.88	0.4
30	5.3	0.4	0.3	0.88	0.3
20	3.6	0.3	0.2	0.88	0.2
10	1.8	0.1	0.1	0.88	0.1
0	0.0	0	0	0.88	0.0

The U_{mf} of the catalyst 4-FPSP in a fluidized bed was determined using a quartz tube from FBR and a pressure drop column. Based on previous experiments conducted in a fixed bed reactor, the optimum activity temperature for the FPSP catalyst series was found to be 650°C. Therefore, the temperature of 650°C was chosen for the U_{mf} testing. The fluidized bed had a radius of 1.33 cm, and N_2 was used as the test gas. The catalyst mass was 5 g, and the particle size ranged from 160~315 μm.

To conduct the U_{mf} test, N_2 gas was introduced into the reactor at a certain flow rate, and the flow rate was gradually increased while recording the pressure drop with an U-shaped manomenter, during the rise in flow rate. After increasing the flow rate to 500 mL/min, there was no significant change in the pressure drop. The flow rate was then started to be reduced and pressure drop was recorded at the same flow rate. The data obtained from the experiment are presented in Table 7.1 and the graphical of the data is shown in Fig. 7.1.

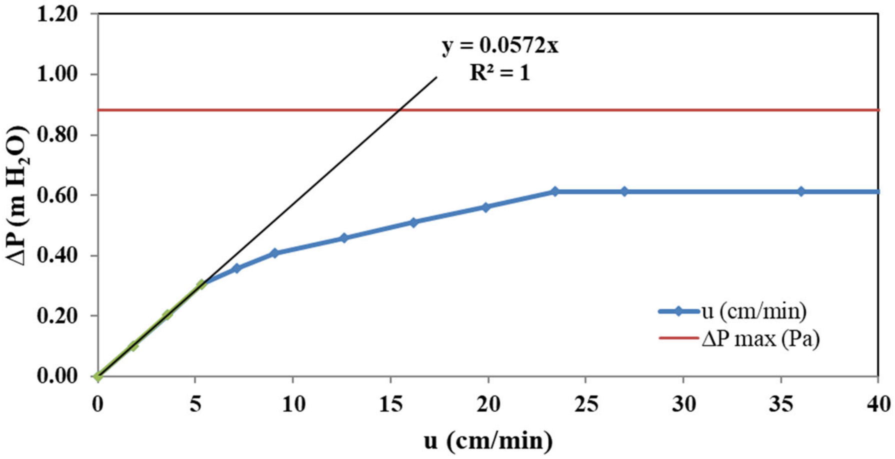

Fig. 7.1 ΔP-u_0 curve.

According to the description in section 2.6.2, U_{mf} is defined as the linear velocity (u) at the intersection of the straight line (ΔP-u0) obtained during the initial loosening of the fixed bed and the straight line representing the maximum theoretical pressure drop (ΔPmax) in the bed.

The slope is obtained from the ΔP-u line.

y=0.0572*x   k=0.0572

Maximum theoretical pressure drop ΔP_{max}:

ΔP_{max}=F/S =0.005 kg/π $(0.0133)^2$=9.00 kg/m^2 = 88.2 Pa= 0.882 cm

As shown in Fig. 7.1, U_{mf} is the linear velocity at the intersection point of the ΔP-u line and Δpmax:

u=ΔP_{max}/k =0.882/0.0572 =15.42 cm^3/ (cm^2*min)

Based on the tests and calculations, at standard temperature and pressure (STP) with a catalyst mass of 5 g, the U_{mf} value was determined to be 15.42 cm^3/ (cm^2*min). For the reactor containing 7.5 g of catalyst, we have chosen to use approximately 2 times U_{mf}, resulting in a gas flow rate of 178 mL (STP)/min for subsequent FBR catalytic reaction experiments.

7.1.2 Issues and improvements in reaction experiments

During the initial stages of conducting catalytic reaction experiments, a series of issues arose due to insufficient process optimization, resulting in the experiments not being completed smoothly and the lack of obtainment of reliable experimental data. Here, we present a list of the encountered problems, analyze their causes and propose corresponding improvements. The details of the process are documented below to provide a reference for future catalytic experiments.

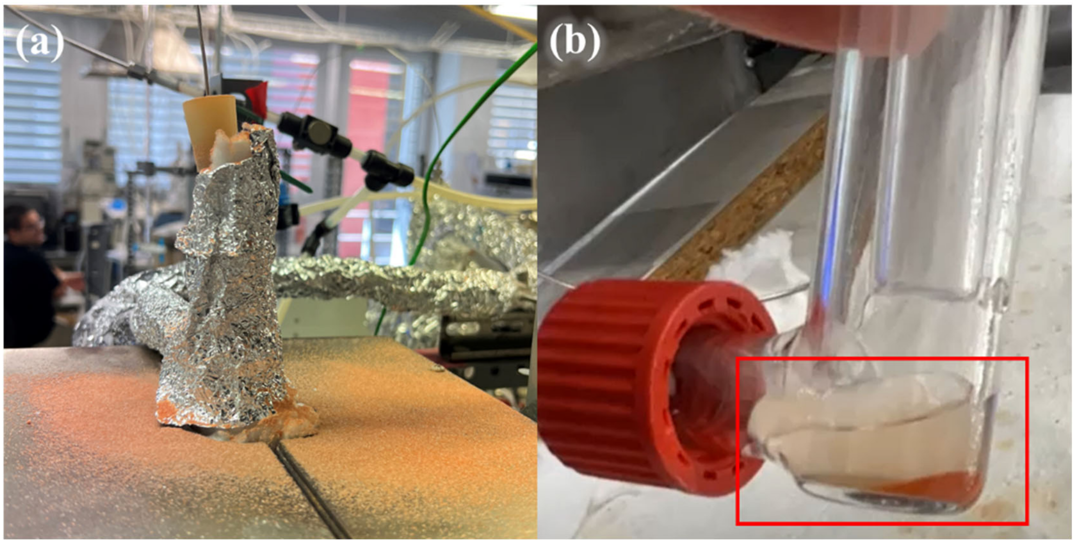

Fig. 7.2 The stopper pops out and the catalyst passes out with the product.

The catalyst was packed into the FBR, where it remained at the lower section of the reactor under the influence of gravity, the reaction gas was introduced from the bottom of the reactor. During the catalytic reaction experiments, the catalyst particles exhibited a fluidized state. The high-temperature fluidization process resulted in varying degrees of catalyst abrasion, generating fine catalyst particles that were discharged along with the unreacted gas and reaction products from the outlet. Due to the numerous bends in the outlet line, the accumulation of small sized catalyst particles causes blockages in the pipeline. The stopper at the top of the reactor pops out, as shown in Fig. 7.2 (a).

Thus, we terminated the experiment and turned off the reaction experimental device. Upon examination of the collected liquid products, some fine catalyst particles were observed, as shown in Fig. 7.2 (b).

The reactor type was changed to a new FBR, as shown in Fig. 7.3. In the new FBR, the upper part of the reactor has a protruding curved outer wall. When the small-sized catalyst particles rose with the gas flow and reach this part, the catalyst to fall back to the bottom of the reactor to some extent due to the blocking effect of the curved outer wall, thereby reducing the loss of small-sized catalyst particles. During the course of the experiment, a similar incident occurred where the stopper from the upper part of the reactor was ejected, leading to the termination of the experiment. After the reactor temperature dropped to room temperature, the exhaust pathway of the reaction device was inspected. The catalyst blocked the exhaust pathway of the reactor and the incomplete reaction gases and products could not be discharged in time leading to an increase in pressure in the reactor and the stopper popping out, as shown in Fig. 7.4.

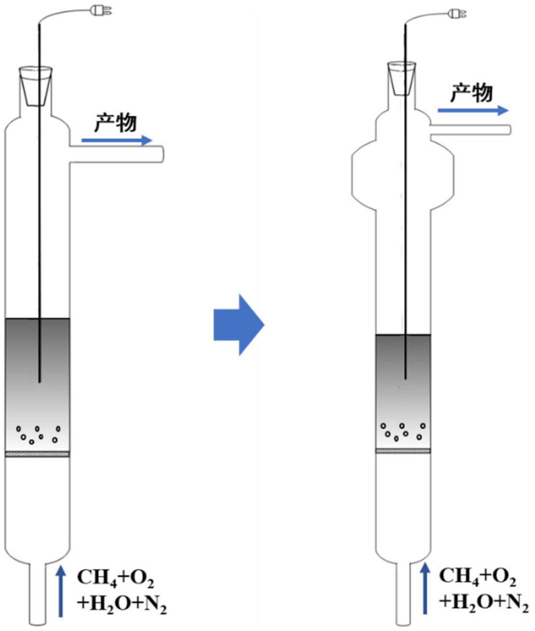

Fig. 7.3 Two types of fluidized bed reactors.

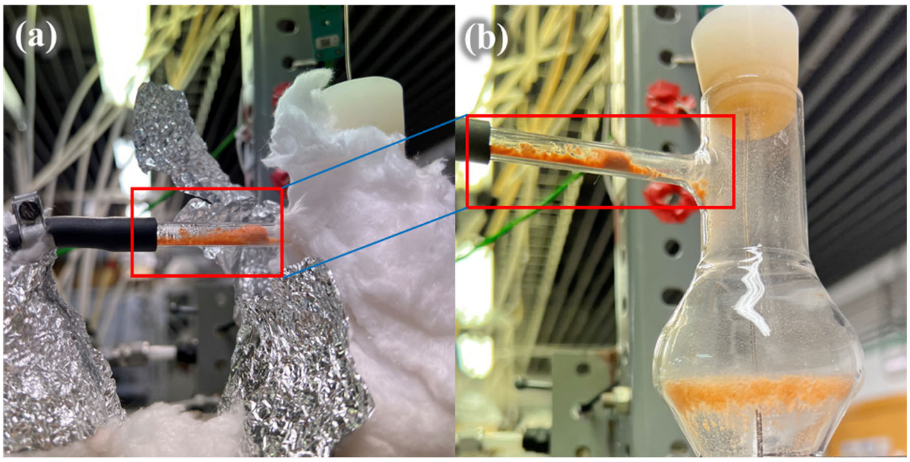

Fig. 7.4 Catalyst blocking the reactor outlet.

In order to improve the issue of small sized catalysts blocking the outlet pipe, three parts of the reaction system were improved, as shown in Fig. 7.5 (a).

(1) As the catalytic reaction temperature was set at 650°C, glass fiber wool was wrapped around the outside of the reactor in order to insulate the reactor. The protruding upper part of the reactor was wrapped in its entirety, leaving the lower part of the protruding part isolated from the heater at the periphery of the reactor, resulting in incomplete heating. The bigger part of the upper part of the reactor was wrapped, resulting in the lower part of the protruding part being isolated from the heater at the periphery of the reactor, making the reactor incompletely heated. The temperature of the protruding part of the reactor was below 650°C resulting in a certain degree of condensation of water vapor and therefore a build-up of small sized catalyst and water vapor at the outlet of the reactor. Changing the way the insulating glass wool was wrapped as shown in Fig. 7-5 (a) left, insulated the reactor and at the same time was able to guarantee the heating control of the protruding part of the heating furnace.

(2) A small amount of quartz wool was placed at the gas outlet of the reactor. With the quartz wool blocking, the small size catalyst no longer exited the channel in large quantities, reducing the possibility of blockage at the outlet.

(3) In the preliminary experiments, the outlet blockage caused an increase in pressure

in the reactor and the catalyst ran out in large quantities with the rapid ejection of the stopper. A stretchable tape was used to bind the stopper in the upper part of the reactor to provide resistance to the stopper popping out again.

The experimental device was improved and the catalytic reaction experiment was performed again. Although the experimental process was completed, the airflow was unstable and the real-time data of the exit product could not be accurately monitored. The experiment was repeated and the experiment was terminated when the stopper ran out during the experiment. After the reactor had cooled down and the insulation on the outside of the reactor was removed, it was found that the catalyst was adhering to the quartz wool at the outlet, blocking the reactor outlet as shown in Fig. 7.5 (b~c).

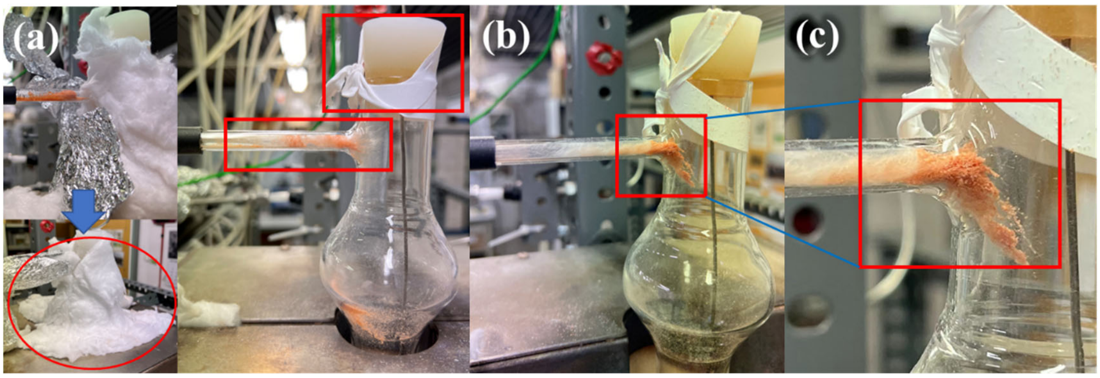

Fig. 7.5 Blockage at the outlet of the modified reactor.

The quartz wool at the outlet was replaced and the experiment was repeated. Midway through the experiment the outlet gas stream was unstable and a catalyst blockage was found at the reactor outlet as shown in Fig. 7.6 (a~b). When the experiment was repeated again the stopper ran out and the experiment was terminated. After the reactor had cooled down and the external insulation of the reactor was removed, it was found that the blocked quartz wool had transferred with the airflow to the connection between the reactor and the pipe, as shown in Fig. 7.6 (c).

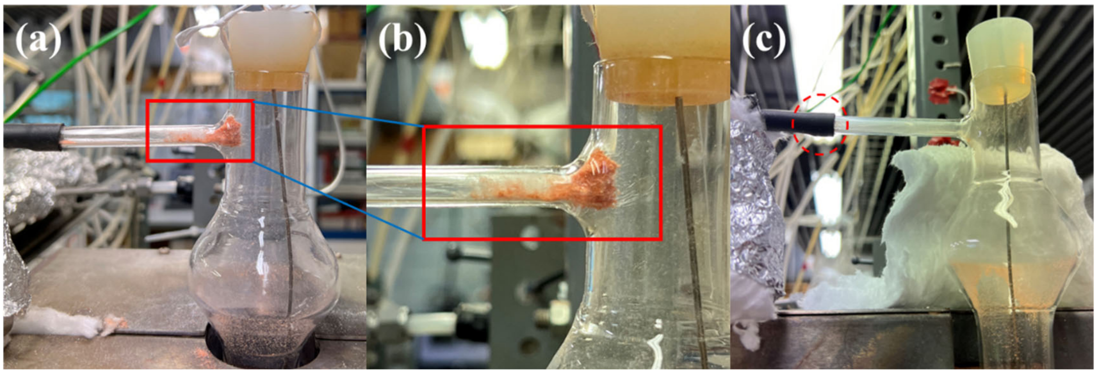

Fig. 7.6 Blockage at the outlet of the reactor.

To solve the problem of the catalyst blocking the reactor outlet, the quartz wool was positioned in the upper bigger part of the reactor so that the catalyst rose with the airflow to this point and no longer flowed into the outlet. At the end of the reaction experiment, the reactor insulation was removed to inspect the reaction device. Fig. 7.7 (a~b) shows that a large number of small sized catalysts were lodged in the bigger part of the reactor. The placement of the quartz wool was changed again as shown in Fig. 7.7 (c) and only a small amount of catalyst was found to have adhered to the quartz wool after the experiment was completed. There was no catalyst blockage at the outlet position and the experiment was successfully completed.

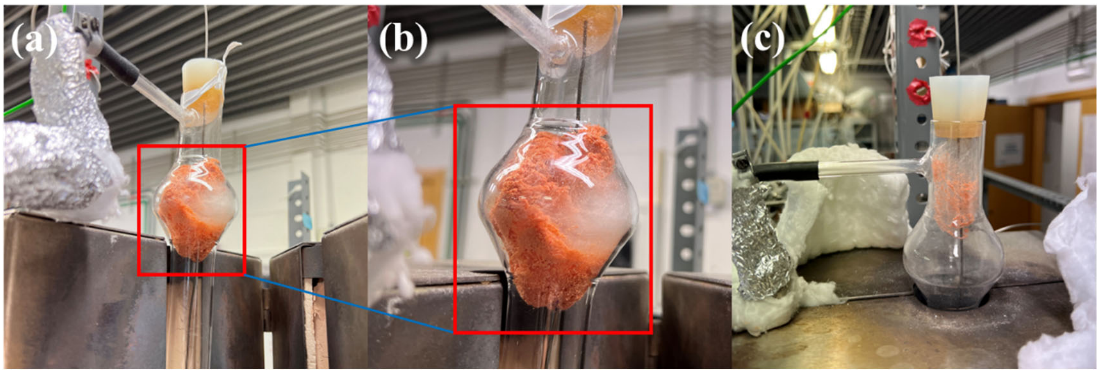

Fig. 7.7 Repositioning the quartz wool.

7.1.3 The catalyst particle size before and after simulating the fluidization experiment

In previous experiments with catalytic reactions, it was found that the small size catalyst would follow the gas flow to the outlet of the reactor, causing the outlet to become blocked or a large amount of catalyst to remain on the quartz wool. To avoid this phenomenon, we carried out simulated fluidization experiments on the catalyst before catalytic reaction experiments. The change in catalyst size was observed before and after the experiment and the catalyst was sieved to remove the small size catalyst. The simulated fluidization experiments were carried out using a conventional FBR at room temperature, air was passed in to simulate the passage of the reaction gas and the outlet was blocked with quartz wool, the experimental device is shown in Fig. 7.8.

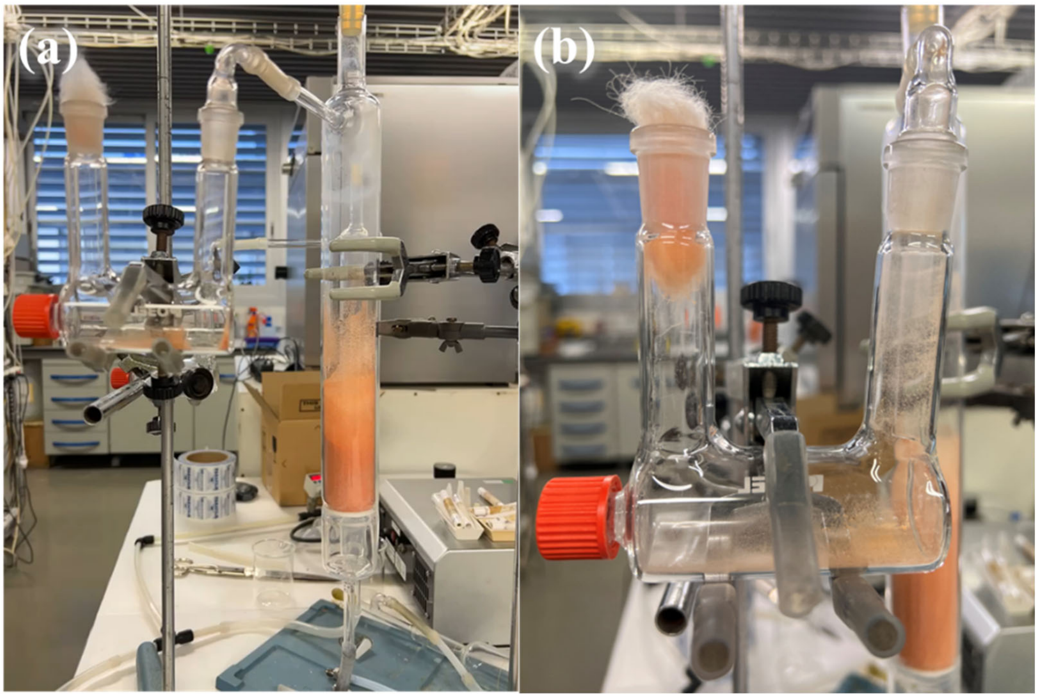

Fig. 7.8 Simulated fluidization experimental device.

After the introduction of the air stream, small size catalyst gradually appeared in the glass collection bottle. A gradual change in colour at the quartz wool indicated that some of the small size catalyst had adhered to the quartz wool at the outlet. After 2 d of continuous simulated fluidization experiments, the remaining catalyst in the reactor was collected and sieved, the mass of catalyst in the different size intervals was weighed and recorded. For comparison, catalysts that had not been subjected to simulated fluidization experiments were sieved and weighed. The size distribution of the two catalysts is shown in Table 7.2 and Fig. 7.9.

Table 7.2 Size distribution of catalyst before and after simulated fluidization.

Particle size (μm)	<90	90~106	106~150	150~180	180~200	200~250	>250
Fresh	1.09%	3.78%	32.28%	17.25%	6.06%	21.36%	17.54%
Used	1.95%	4.85%	34.63%	19.14%	7.02%	18.90%	13.50%

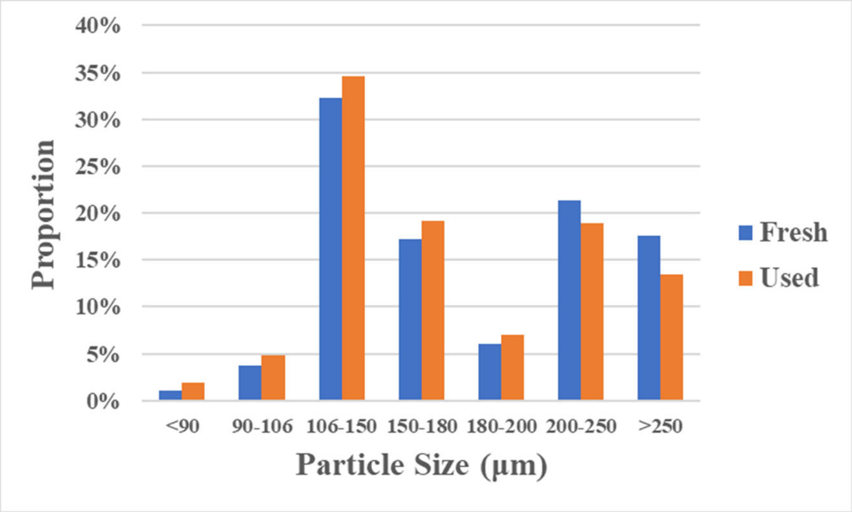

Fig. 7.9 Size distribution of catalyst before and after simulated fluidization.

As a result of simulated fluidization experiments, a higher proportion of the mass of fresh catalyst was found in the large size distribution range. In the small size distribution range, the used catalyst mass accounted for more. The size distribution of the catalysts after the simulated fluidization experiments shifted towards a smaller size distribution overall compared to the fresh catalysts. The data indicated that the collision of the catalysts with each other during the experiment would cause the catalysts to wear and break up, thus splitting the small size catalysts.

Preliminary experiments found that the small size catalyst was highly susceptible to flowing with the gas flow to the FBR outlet. Therefore, a larger size catalyst may be more appropriate. Simulated fluidization experiments were carried out for 2 d on catalysts and supports ranging in size from 160~315 μm to investigate the influence of the fluidization process on the size of the catalysts as well as the SiO_2 precipitating supports. The data is recorded in Table 7.3.

Table 7.3 Mass changes and size distribution of catalyst and support before and after simulated fluidization.

Simulation experiment	The first day			The second day		
Catalyst	Before	After	Size distribution	Before	After	Size distribution
SP	5.72 g	5.38 g (94.1%)	> 160 μm： 5.32 g (98.9%) < 160 μm： 0.06 g (1.1%)	5.32 g	5.21 g (97.9%)	> 160μm： 5.24 g (99.4%) < 160μm： 0.03 g (0.6%)
4-FPSP	5.72 g	5.33 g (93.2%)	> 160 μm： 4.89 g (92.1%) < 160 μm： 0.42 g (7.9%)	4.74 g	4.68 g (98.7%)	> 160μm： 4.29 g (95.1%) < 160μm： 0.22 g (4.9%)

Table 7.3 presents the size distribution information of catalyst 4-FPSP and support SP after a 2-day simulation fluidization experiment. It can be observed that after the first day of simulation, both 4-FPSP and SP experienced a total mass loss of 6% to 7%. The lost material was primarily carried along with the gas flow towards the outlet, accumulating in the glass collection bottle and adhering to the quartz wool at the outlet. Among the remaining materials in the size range >160 μm, 4-FPSP accounted for 92.1% compared to SP (98.9%), indicating that the simulation fluidization experiment caused greater damage to the catalyst compared to the support. This is due to the fact that the overall structure of the catalyst 4-FPSP heated by stirring is not as complete and robust

as the support SP and is more susceptible to damage. The remaining materials with size >160 μm were reintroduced into the reactor for the second day of simulation experiment. The data revealed that the loss of 4-FPSP and SP after the second day of simulation was around 2%. Among the remaining materials, the proportion of support SP with size >160 μm was 99.4%, indicating minimal wear of SP during the second day of simulation. The proportion of 4-FPSP with size >160 μm was 95.1%, showing an improvement compared to the 92.1% observed on the first day.

In order to minimize the problem of the catalyst flowing out of the reactor and blocking the reactor outlet and the reactor exhaust channel, the catalysts used in the subsequent catalytic reaction experiments were subjected to a 2 d simulated fluidization experiment and sieved to the required size.

7.1.4 The influence of catalyst size on the reactions

In FBR, catalyst size has an impact on the fluidization velocity during the reaction, which in turn affects the catalytic reaction. The reactor used in the catalytic experiments allows for catalyst particle sizes higher than 106 μm. To minimize the loss of small-sized catalyst particles, increasing the minimum catalyst particle size to 160 μm may be more suitable.

Table 7.4 Performance of 4-FPSP catalysts of different sizes in catalytic reaction experiments.

Experiment	Cat.	Catalysts sizes (μm)	Conversion (%)		Selectivity (%)	Yield (%)
			O_2	CH_4	HCHO	HCHO
7-1-1	4-FPSP	106~315	24.55	12.81	0.39	0.0505
7-1-2		160~315	21.64	23.37	0.32	0.0751

To investigate the influence of catalyst size variation on catalytic reactions, a catalytic reaction experiment was conducted at a temperature of 650°C, with a heating rate of 10 °C/min. The water molar fraction in the feed was set at 62%, and the gas flow rate was 178 mL/min, with a CH_4/O_2 ratio of 1:1. Two types of 4-FPSP catalysts with different sizes (106~315 μm and 160~315 μm) were used in the catalytic reaction experiments, and their performance in the reaction was compared. The results are presented in Table 7.4 and Fig. 7.10.

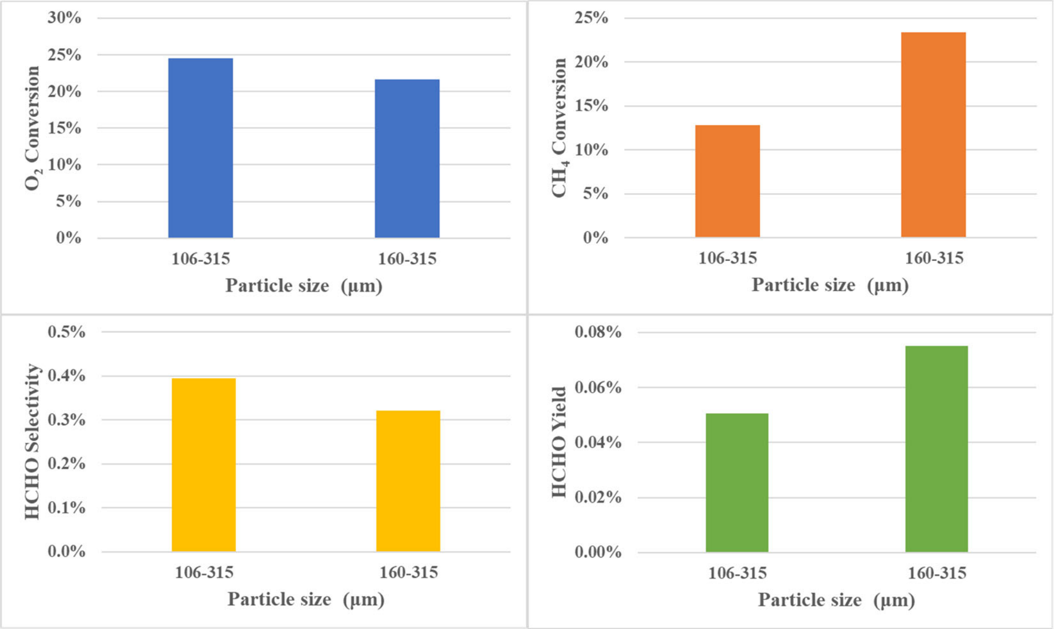

Fig. 7.10 Performance of 4-FPSP catalysts of different sizes in catalytic reaction experiments.

The data presented in the table and the comparative graph indicated that the 160~315 μm size of 4-FPSP catalyst exhibited a higher CH_4 conversion, while the 106~315 μm size of 4-FPSP catalyst demonstrated a higher selectivity of HCHO. This could be attributed to the fact that within the same catalyst, some mass transfer limitations appear with the larger particles, and it is a well known fact that when mass transfer limitations appear in a catalytic system with reactions in series, the selectivity to the intermediate compound decreases. Calculations indicated that the 160~315 μm size of 4-FPSP catalyst achieved a higher HCHO yield. Therefore, 4-FPSP of 160~315 μm size was used as catalyst in subsequent catalytic reaction experiments after simulated fluidization experiments and sieving.

7.1.5 The influence of oxygen partial pressure on the reactions

The influence of oxygen partial pressure on catalytic reactions was further investigated in the FBR. The catalytic reaction experiments were conducted at a temperature of 650°C with a heating rate of 10 °C/min. The water molar fraction in the feed was 62%, and the gas flow rate was 178 mL/min. The oxygen partial pressure in the reaction gas was varied to different levels by adjusting the CH_4/O_2 ratio to 1/1, 3/1, and 5/1, while keeping other parameters constant. The performance of the 4-FPSP catalyst under different oxygen partial pressures in the FBR was examined. The experimental data and results are presented in Table 7.5 and Fig. 7.11 for comparison.

Table 7.5 Influence of different oxygen partial pressures on catalytic reaction.

Experi-ment	Cat.	CH_4/O_2	Flow rate (mL/min)	Conversion (%)		Selectivity (%)	Yield (%)
				O_2	CH_4	HCHO	HCHO
7-2-1	4-FPSP	1/1	178	33.79	32.26	0.11	0.0368
7-2-2		3/1		56.77	15.43	0.17	0.0268
7-2-3		5/1		55.86	10.04	0.20	0.0196

The result showed that as the oxygen partial pressure increases, the conversion of CH_4 increased while the selectivity of HCHO decreased. This could be attributed to the abundant oxygen providing an oxygen-rich environment for the catalytic reaction, promoting the occurrence of the reaction and leading to higher CH_4 conversion. However, the increased conversion of CH_4 also intensifies its deep oxidation, resulting in the generation of more CO and CO_2, which reduced the selectivity to HCHO. Calculations indicated that, consistently with the results obtained in fixed bed reactors, the CH_4/O_2 ratio of 1/1 obtained a higher HCHO yield.

Based on the experimental discussion in this section, higher HCHO yields were obtained with 160~315 μm size of 4-FPSP catalysts in FBR at a flow rate of 178 mL/min and an oxygen partial pressure setting of CH_4/O_2=1/1. Prior to the initiation of catalytic reaction experiments, conducting simulated fluidization experiments on the catalyst proved advantageous for the smooth progress of the catalytic reaction experiments.

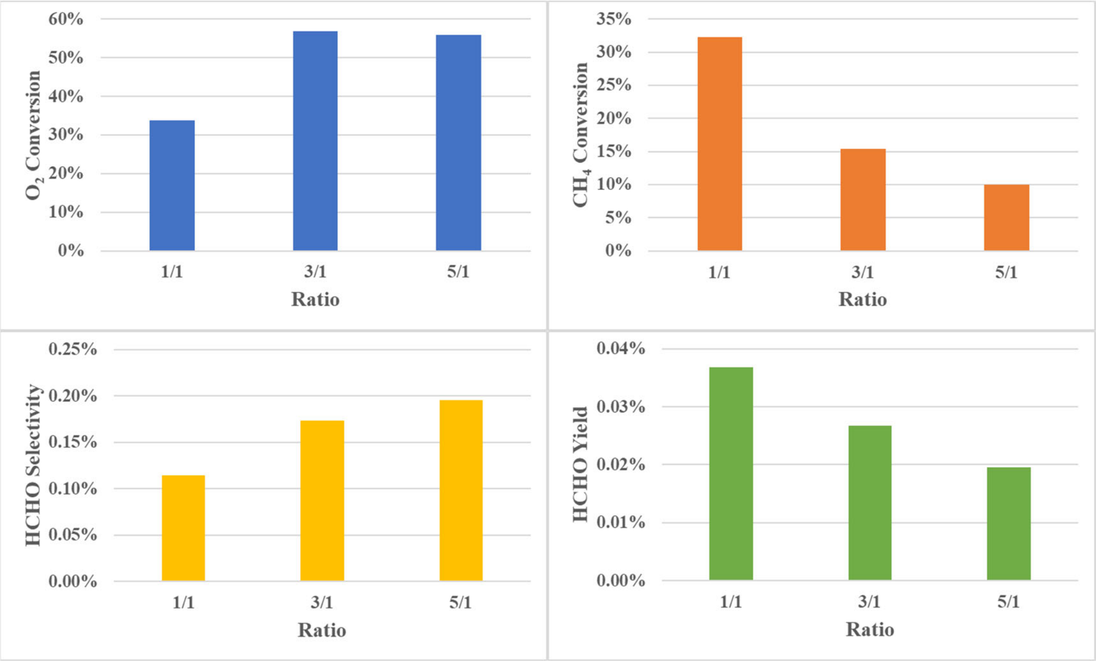

Fig. 7.11 Influence of different oxygen partial pressures on catalytic reaction.

7.2 Performance of the catalyst in the two-zone fluidized bed reactor

The TZFBR is a reactor that allows for two simultaneous chemical reactions to occur, each taking place in the upper and lower sections of the fluidized bed. Oxygen mixed with possibly added inert gas is fed into the lower part of the fluidized bed of the reactor where the catalyst reacts with the gas phase oxygen in an oxidation reaction. CH_4 is fed into the middle point of the fluidized bed and the catalyst is reduced by carrying lattice oxygen that react with the CH_4. The reaction products, unconverted reactants, and inert dilution gases are discharged from the outlet of the reactor.

In the previous section, the performance of the catalyst 4-FPSP in the FBR catalytic reaction experiments was presented. In this section, a comparison was made between the FBR and TZFBR regarding their performance in catalytic reaction experiments. The influence of catalyst support, CH_4 introduction point, N_2 introduction, and reactant gas flow rate on the catalytic performance of the 4-FPSP catalyst in the TZFBR were investigated.

7.2.1 Comparison of the performance of FBR and TZFBR

Table 7.6 Performance of 4-FPSP catalyst in FBR and TZFBR.

Experiment	Cat.	Reactor	Conversion (%)		Selectivity (%)	Yield (%)
			O_2	CH_4	HCHO	HCHO
7-3-1	4-FPSP	FBR	33.79	32.26	0.11	0.0368
7-3-2		TZFBR	24.24	22.48	0.24	0.0538

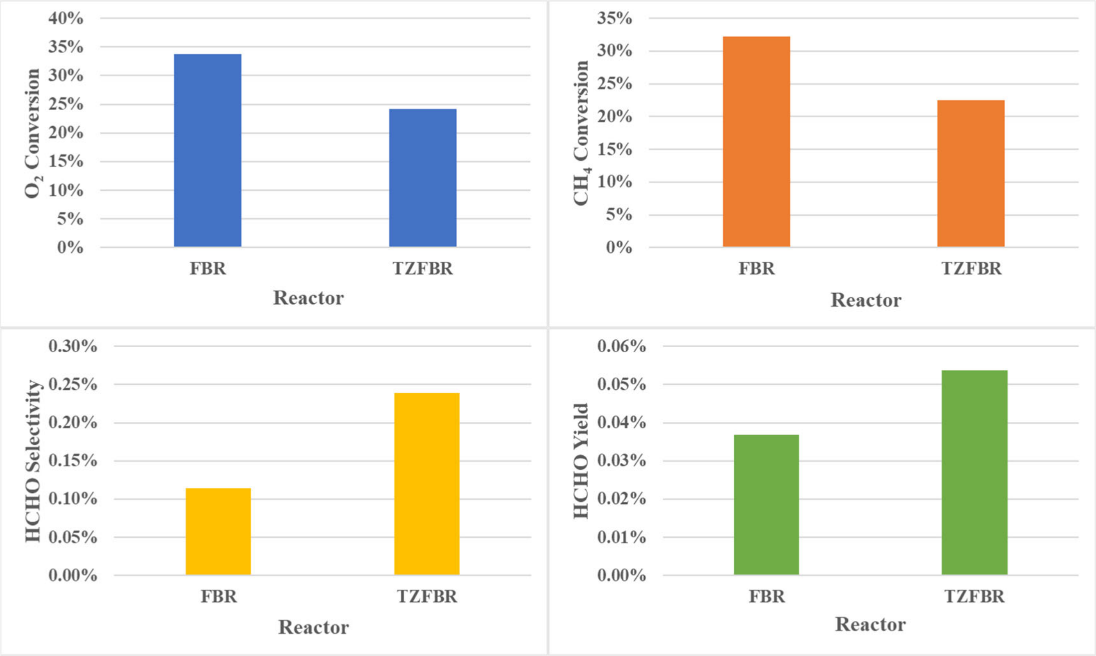

Fig. 7.12 Performance of the 4-FPSP catalyst in FBR and TZFBR.

In order to validate the advantages of TZFBR in catalytic reaction experiments, catalytic reaction experiments were conducted in both reactor configurations using the same experimental parameters to compare the performance of the 4-FPSP catalyst. The catalytic reaction experiments were carried out at a temperature of 650°C with a heating rate of 10 °C/min. The water molar fraction in the feed was 62%, and the gas flow rate was maintained at 178 mL/min with a CH_4/O_2 ratio of 1/1. The experimental data and results are presented and compared in Table 7.6 and Fig. 7.12.

The experimental data showed that the conversion of both CH_4 and O_2 was reduced in TZFBR compared to FBR, while the selectivity of HCHO was increased. This could be attributed to the fact that in TZFBR, CH_4 was introduced from the middle section of the fluidized bed. The reaction zone was only present in a part of the fluidized bed and the amount of catalyst involved in the catalytic reaction was reduced, resulting in a lower conversion of CH_4 and O_2. In the reaction zone, the source of a significant amount of oxygen in the catalytic reaction was the lattice oxygen carried by the catalyst. The reduced oxygen content in the gas phase avoided to some extent the deep oxidation of CH_4, thus improving the selectivity of HCHO. The catalytic reaction carried out in TZFBR was calculated to obtain a higher selectivity of HCHO (2.18 times) and a higher yield of HCHO (1.46 times) compared to FBR.

7.2.2 The influence of catalyst supports on the reactions

We searched for a new SiO_2 precipitation support (H-SP). Compared to the SiO_2 support used previously (D-SP), H-SP has a stronger and denser monolithic structure that is less likely to break down during fluidization. Two SiO_2 supports were subjected to simulated fluidization experiments and sieved and weighed to analyze their size distribution after the simulations. The recorded data are presented in Table 7.7.

From the data, it was evidenced that after 2 days of simulated fluidization experiments, both supports experienced a loss of approximately 1%. The remaining SiO_2 supports were subjected to sieving and weighing, revealing that within the size range of >160 μm, H-SP accounted for 99.3% while D-SP accounted for 95.7%. This confirmed that the H-SP has a more robust overall structure than the D-SP and was relatively less prone to breakage during fluidization collisions.

Table 7.7 Particle size distribution of H-SP and D-SP SiO_2 precipitated supports after simulated fluidization experiment.

Support	Simulation experiment (2 day)		
	Before	After	Size distribution
H-SP	10.0 g	9.9 g (99.0%)	> 160 μm： 9.72 g (99.3%) 106~160 μm： 0.06 g (0.6%) < 106 μm: 0.013 g (0.1%)
D-SP	10.6 g	10.5 g (99.1%)	> 160 μm： 10.07 g (95.7%) 106~160 μm： 0.44 g (4.2%) < 106 μm: 0.01 g (0.1%)

Table 7.8 Particle size distribution of catalysts synthesized using H-SP and D-SP SiO_2 precipitated supports.

Support	Synthesis 4 wt.%FPSP	
	Total	Size distribution
H-SP	8.5 g	> 160 μm： 5.23 g (68.5%) 106~160 μm： 2.10 g (27.5%) < 106 μm: 0.30 g (3.9%)
D-SP	15.1 g	> 160 μm: 1.66 g (11.6%)

106~160 μm： 1.25 g (8.7%)

< 106 μm: 11.38 g (79.6%)

In order to select a more suitable SiO_2 precipitation support for the preparation of catalysts, catalyst synthesis experiments were carried out using both supports for the same preparation process. The synthesized catalyst material was sieved and the mass of the different sizes of catalyst was weighed. The data were recorded in Table 7.8.

The data showed that 68.5% of the total mass of size of ＞160 μm and 3.9% of the total mass of size of < 106 μm of catalysts using H-SP as a support. The mass of size of ＞160 μm of the catalyst using D-SP as a support was 11.6% of the total mass, and the mass of size of ＜106 μm was 79.6% of the total mass. These results indicated that when using H-SP as the support for catalyst preparation, the overall structure was more compact, thereby preventing excessive fragmentation during the preparation process and minimizing the reduction in catalyst size. From the weighting results, by using H-SP as a support, the overall structure of the catalyst was more dense and less likely to be overly fragmented during the preparation process resulting in a smaller catalyst size.

To investigate the influence of different SiO_2 support types on catalytic reactions, catalysts prepared using two different supports were employed in catalytic reaction experiments. The catalytic reaction experiments were conducted at a temperature of 650°C, with a heating rate of 10 °C/min. The water molar fraction in the feed was 62%, the gas flow rate was set at 178 mL/min with a CH_4/O_2 ratio of 1:1. The experimental data and comparative results were presented in Table 7.9 and Fig. 7.13.

Table 7.9 The influence of different types of catalyst supports on catalytic reaction.

Experiment	Cat.	Catalyst support	Conversion (%)		Selectivity (%)	Yield (%)
			O_2	CH_4	HCHO	HCHO

7-4-1	4-FPSP	D-SP	24.24	22.48	0.24	0.0538
7-4-2		H-SP	25.38	28.42	0.29	0.0826

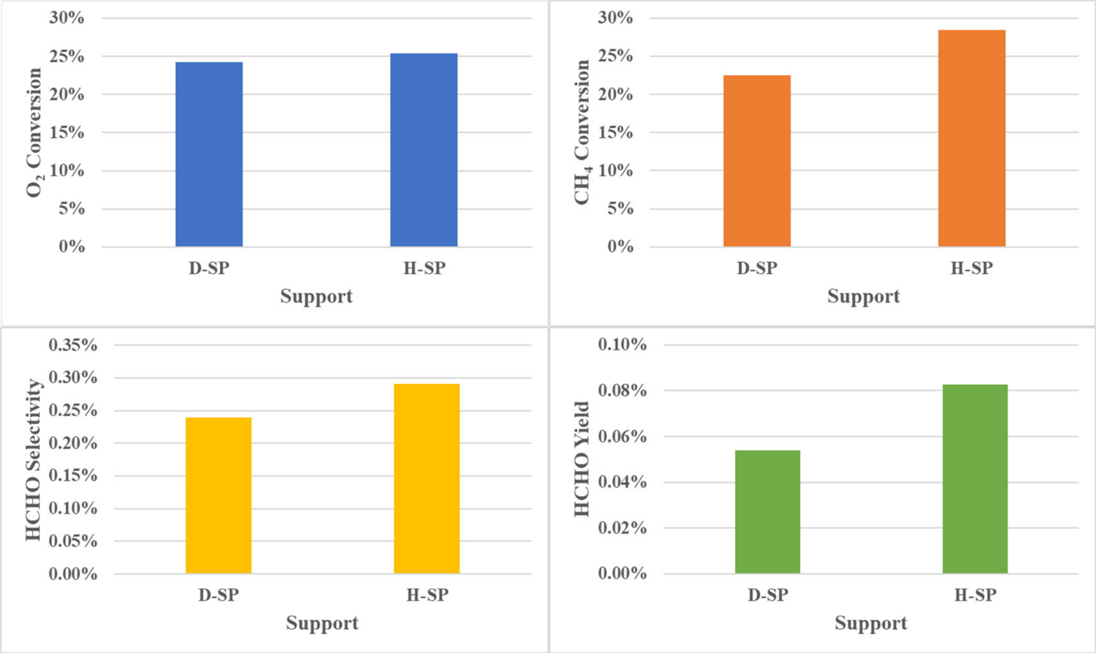

Fig. 7.13 The influence of different types of catalyst supports on catalytic reaction.

The data indicated that the catalyst prepared using the H-SP support achieved higher conversion of CH_4 and O_2, as well as higher selectivity and yield of HCHO. The experimental results indicated that H-SP was more suitable as a catalyst support.

7.2.3 The influence of the location of the CH_4 introduction point on the reaction

In the previous reaction experiments, the CH_4 introduction point was positioned at the middle of the catalyst bed while it remained stationary (5 cm). Once the reaction gases were introduced into the reactor, the catalyst bed particles started to fluidize, causing an increase in the bed height (7.5 cm). As a result, the CH_4 introduction point was no longer located in the middle of the fluidized bed but shifted to the lower part of the bed (5 cm from the top of the bed, 2.5 cm from the bottom). To investigate the influence of the position of the CH_4 introduction point on the catalytic reaction, the experiment was repeated by moving the position of the CH_4 introduction point up to the middle of the fluidized bed (3.75 cm from both the top and bottom of the bed). The experimental parameters remained consistent with the previous. The experimental results and data are recorded in Table 7.10 and Fig. 7.14.

Table 7.10 The influence of CH_4 introduction position on the reaction.

Experi-ment	Cat.	CH_4 introduction point	Conversion (%)		Selectivity (%)	Yield (%)
			O_2	CH_4	HCHO	HCHO
7-5-1	4-FPSP	middle	25.38	28.42	0.29	0.0826
7-5-2		lower	31.92	32.91	0.23	0.0773

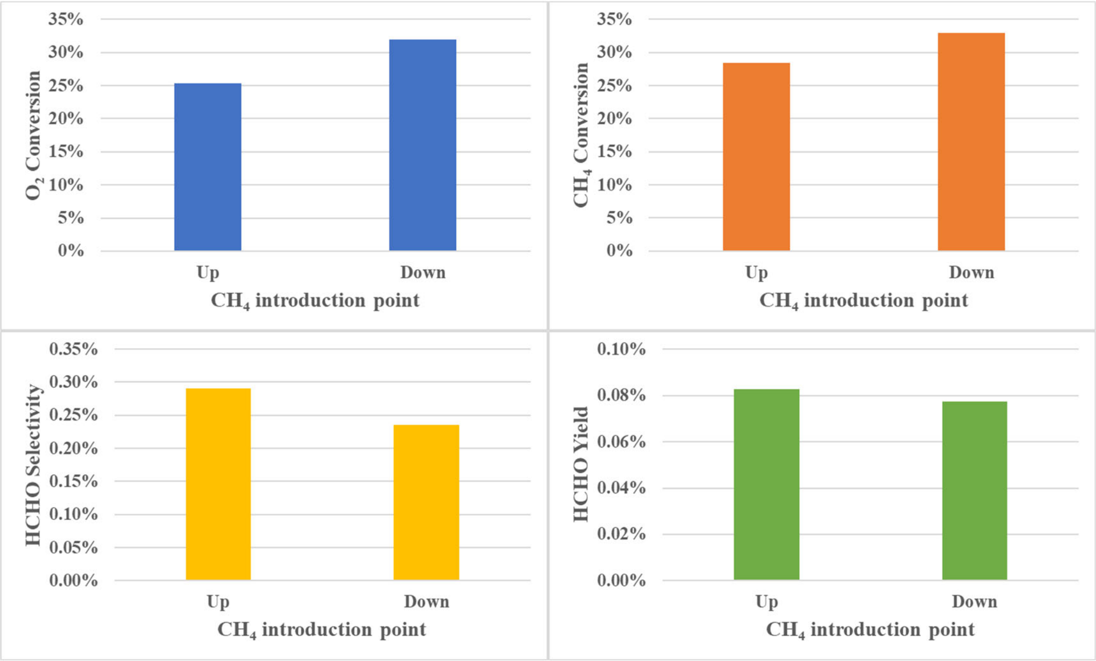

Fig. 7.14 The influence of CH_4 introduction position on the reaction.

The results indicated that shifting the CH_4 introduction point upwards resulted in a slight decrease in the conversion of CH_4 and O_2, but an increase in the selectivity of HCHO. This could be attributed to the reduction in the reaction zone as the CH_4

introduction point was moved upwards, leading to a decrease in the amount of catalyst participating in the reaction and subsequently reducing the conversion of CH_4 and O_2. At the same time, an upward shift in the lower limit of the reaction zone resulted in less gas-phase oxygen in the reaction zone, resulting in higher selectivity for HCHO. It was calculated that a higher yield of HCHO was obtained for the catalytic reaction after the position of the CH_4 introduction point was shifted upwards.

7.2.4 The influence of N_2 introduction on the reaction

In the previous experiments, in order to achieve the same flow rate of 178 mL/min in the regeneration zone in the lower part of the fluidized bed of the reactor, an inert dilution gas N_2 was introduced at the same time as oxygen at the lower inlet of the reactor. In this case, while the flow rate in the lower part reached 178 mL/min, the flow rate in the upper reaction zone, where CH_4 was introduced, was higher than 178 mL/min. Here, a temperature of 650°C was employed as the catalytic reaction temperature, the water molar fraction in the feed was 62% and a CH_4/O_2 ratio of 1:1. The influence of the introduction of the inert dilute gas N_2 on the catalytic reaction was examined and the experimental results are shown in Table 7.11 and Fig. 7.15.

The experimental results demonstrate that the introduction of inert dilution gas N_2 into the TZFBR resulted in increased conversion of O_2 and CH_4, as well as higher selectivity and yield of HCHO. In the previous experiments, the increase in flow rate was due to an increased inflow of CH_4 and O_2 mixture within a unit of time, leading to a decrease in the conversion of O_2 and CH_4. In this case, the increase in flow rate was a result of the introduction of inert dilution gas N_2, which promoted the contact between the catalyst and the reactant gases, thus enhancing the conversion rates of O_2 and CH_4.

Table 7.11 The influence of N_2 introduction on the catalytic reaction.

Experiment	Cat.	N_2 introduction	Conversion (%)	Selectivity (%)	Yield (%)

			O_2	CH_4	HCHO	HCHO
7-6-1	4-FPSP	Yes	31.92	32.91	0.23	0.0773
7-6-2		No	29.56	28.46	0.23	0.0641

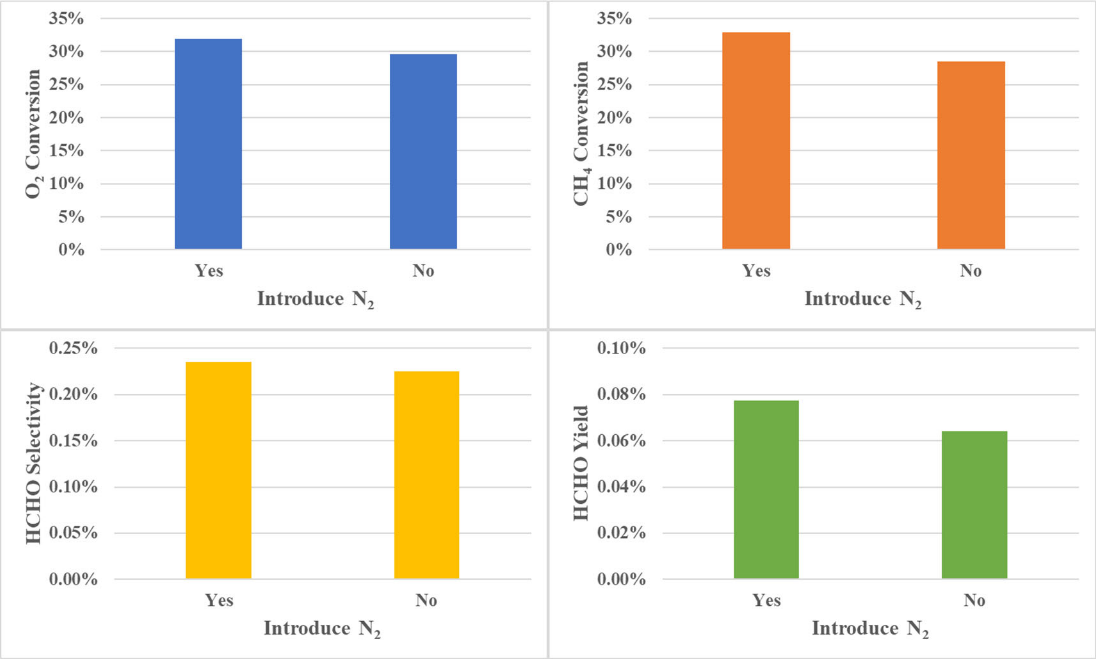

Fig. 7.15 The influence of N_2 introduction on the catalytic reaction.

7.2.5 The influence of flow rate on the reaction

Based on preliminary U_{mf} calculations and taking into account the amount of catalyst in the bed, a series of catalytic reaction experiments were carried out with a flow rate of 2 times the U_{mf} of 178 mL/min. In order to further understand the influence of different flow rates on the catalytic reaction experiments in TZFBR, the flow rate was increased and catalytic reaction experiments were carried out.

Table 7.12 The influence of different flow rates on the catalytic reaction.

Experiment	Cat.	CH_4/O_2	Flow rate (mL/min)	Conversion (%)		Selectivity (%)	Yield (%)
				O_2	CH_4	HCHO	HCHO

7-7-1	4-FPSP	1/1	178	29.56	28.46	0.23	0.0641
7-7-2			267	23.73	25.95	0.26	0.0670
7-7-3			356	33.91	33.80	0.15	0.0510

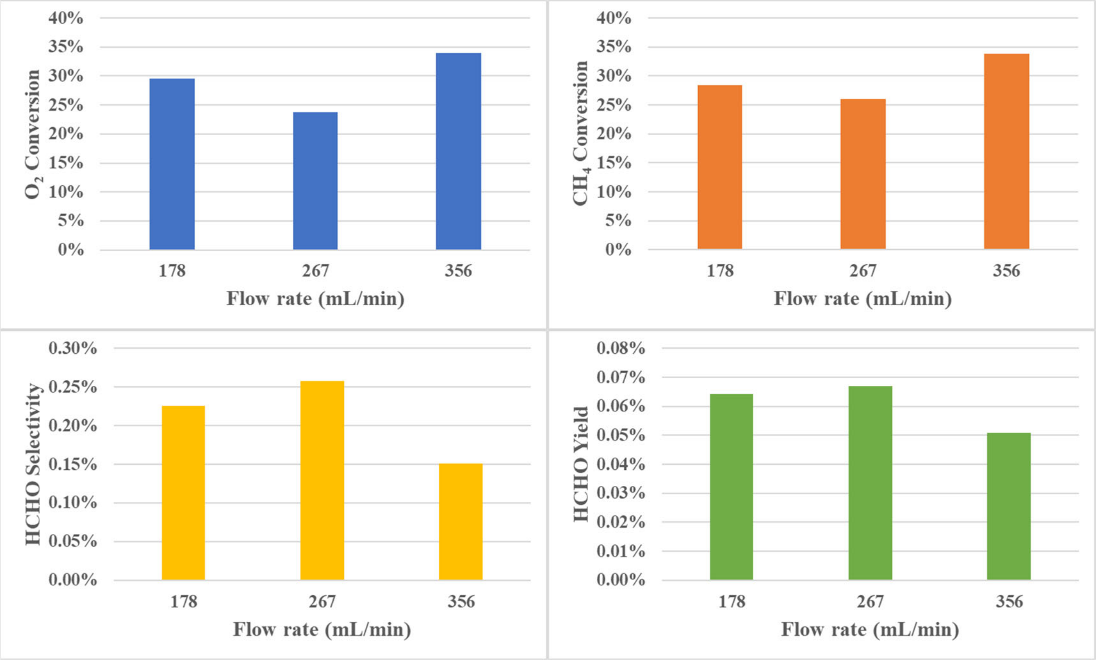

Fig. 7.16 The influence of different gas flow rates on the catalytic reaction.

The experiments were performed at a temperature of 650°C with a heating rate of 10 °C/min. The water molar fraction in the feed was 62% and the CH_4/O_2 ratio was 1:1. The controlled variables were different gas flow rates: 178 mL/min, 267 mL/min, and 356 mL/min. The experimental results are presented in Table 7.12 and Fig. 7.16.

The experimental results showed that the conversion of O_2 and CH_4 tended to decrease and then increase as the flow rate increased, and the selectivity of HCHO reached its highest at a flow rate of 267 mL/min. It was calculated that the highest HCHO yield was obtained for the experiment with a flow rate of 267 mL/min.

Based on the experiments and results analysis in this section, it can be concluded that compared to the FBR, the catalytic reaction conducted in the TZFBR achieved higher selectivity and yield of HCHO. The H-SP type SiO_2 support has a more robust overall structure than D-SP and is less prone to excessive fragmentation during synthesis experiments and the synthesized catalyst is less prone to breakage during fluidization collisions. The synthesized catalyst using H-SP support demonstrated higher CH_4 conversion, as well as increased selectivity and yield of HCHO. Shifting the CH_4 introduction point upward resulted in higher HCHO yield. The introduction of N_2 led to an increased flow rate, which improved the selectivity of HCHO and the conversion of O_2 and CH_4.

7.3 Chapter summary

This chapter presents the performance of the catalysts in two different types of reactors FBR and TZFBR for catalytic reaction experiments. By investigating the influence of U_{mf}, catalyst size, oxygen partial pressure, and gas flow rate in FBR, as well as the influence of catalyst support, CH_4 introduction point, introduction of inert dilution gas, and flow rate in TZFBR, a comparison is made between the performance of different reactors in catalytic reactions. The conclusions are as follows:

(1) The catalyst 4-FPSP was able to achieve higher HCHO yields in FBR with a flow rate of 178 mL/min and an oxygen partial pressure setting of $CH_4/O_2 = 1/1$.

(2) Simulated fluidization experiments were carried out and the catalysts were sieved prior to the start of the catalytic reaction experiments. 160~315 μm size catalysts were more favorable for the catalytic reaction experiments.

(3) H-SP type SiO_2 supports have a more robust overall structure than D-SP. Catalysts synthesized on H-SP supports achieved higher conversions of CH_4 and O_2, as well as higher selectivity and yields of HCHO.

(4) In TZFBR, an upward shift in the position of the CH_4 introduction site resulted in a higher yield of HCHO for the catalytic reaction.

(5) The catalytic reaction in TZFBR achieved higher HCHO selectivity (2.18 times) and higher HCHO yield (1.46 times) compared to FBR.

Conclusion

For the conversion of CH_4 to the more transportable HCHO, this thesis presents the synthesis of a series of candidate catalyst materials using SiO_2 as a support for the direct catalytic oxidation of CH_4 to HCHO in fixed bed reactors, FBR and TZFBR. The SA support, FMSA and FPSA series of candidate catalyst materials were prepared by heating reflux and sol-gel method in combination with ethanol supercritical drying technology. Meanwhile, FPSP candidate catalyst materials were prepared by the impregnation method. The parameters such as the amount of each component added, the time and temperature of heating reflux during the synthesis of SiO_2 aerogel-based composites were adjusted. The influence of the type and temperature of the coagulation bath on the influence of dripping spheres was investigated. The structure and properties of the SiO_2 aerogel-based composites were analyzed using a variety of characterization techniques, including the composition of the physical phase, microscopic morphology and redox properties. The candidate catalysts were filled in fixed bed reactors, FBR and TZFBR, the influence of experimental parameters such as reaction experiment temperature, pre-oxidation reaction, amount of introduced water and oxygen partial pressure and flow rate on the catalytic reaction were investigated, as well as the influence of the introduction point of CH_4 and the introduction of inert dilute gas in TZFBR on the catalytic reaction. The conversion of CH_4, the selectivity and yield of HCHO obtained with different catalysts, different experimental parameters, and in different reactors were compared. The main conclusions are as follows:

(1) The SiO_2 aerogel-based catalyst materials FMSA and FPSA obtained by dropping the sol after 2h10min heating reflux in a PDMS coagulating bath at 80°C have a more

complete overall structure. SiO_2 aerogel-based composites have a three-dimensional skeleton structure with nanoscale particles connected, a rich pore structure with mainly mesopores and a homogeneous dispersion of active components in the composite. The specific surface area of the SiO_2 aerogel-based series of composites can all reach over 1000 m^2/g.

(2) In a fixed bed reactor with a pre-oxidation reaction prior to the catalytic experiments, at an experimental temperature of 650°C, a reaction gas flow rate of 162.5 mL/min, a catalyst mass of 0.6 g, a CH_4/O_2 ratio of 1/1 and the water molar fraction in the feed of 62%, the spherical SiO_2 aerogel-based catalyst 4-FPSA obtained a higher HCHO selectivity, 4-FPSP catalysts with sizes of 160~315 μm obtained higher HCHO yields.

(3) In FBR and TZFBR, catalysts of 160~315 μm size obtained by sieving after simulated fluidization experiments before the start of the experiment were more favorable for the experimental operation of the catalytic reaction. The catalytic reaction in TZFBR achieved higher HCHO selectivity (2.18 times) and higher HCHO yield (1.46 times) compared to FBR.

Conclusión

Para la conversión de CH_4 en el más transportable HCHO, esta tesis presenta la síntesis de una serie de materiales catalíticos candidatos utilizando SiO_2 como soporte, para la oxidación catalítica directa de CH_4 a HCHO en reactores de lecho fijo, FBR y TZFBR. Las series con soporte de aerosol de sílice, FMSA y FPSA, de materiales catalizadores candidatos se prepararon mediante calentamiento en reflujo y método sol-gel en combinación con la tecnología de secado supercrítico de etanol. Por otra parte, los materiales catalizadores candidatos FPSP se prepararon mediante el método de impregnación. Se ajustaron parámetros como la cantidad añadida de cada componente, el tiempo y la temperatura durante la síntesis de los materiales compuestos basados en aerogeles de SiO_2. Se investigó la influencia del tipo y la temperatura del baño de coagulación sobre las características de las esferas de goteo. La estructura y las propiedades de los compuestos basados en aerogeles de SiO_2 se analizaron mediante diversas técnicas de caracterización, como la composición de la fase física, la morfología microscópica y las propiedades redox. Los catalizadores candidatos se utilizaron en reactores de lecho fijo, FBR y TZFBR, y se investigó la influencia de parámetros experimentales como la temperatura de reacción, la preoxidación del catalizador, la cantidad de agua introducida y la presión parcial de oxígeno y el caudal de alimentación, así como la influencia del punto de introducción del CH_4 y la introducción de gas inerte diluido en el TZFBR. Se compararon la conversión de CH_4, la selectividad y el rendimiento a HCHO obtenidos con diferentes catalizadores, diferentes parámetros experimentales y en diferentes reactores. Las principales conclusiones son las siguientes:

(1) Los materiales catalíticos basados en aerogeles de SiO_2 FMSA y FPSA obtenidos por caída del sol tras 2 h10 min de calentamiento a reflujo en un baño coagulante de PDMS a 80°C tienen una estructura global más completa. Los compuestos basados en aerogeles de SiO_2 tienen una estructura de esqueleto tridimensional con partículas a nanoescala conectadas, una rica estructura de poros con mesoporos principalmente y una dispersión homogénea de los componentes activos en el compuesto. La superficie específica de la serie de compuestos a base de aerogel de SiO_2 puede superar los 1000 m^2/g.

(2) En un reactor de lecho fijo con el catalizador esférico a base de aerogel de SiO_2 4-FPSA se obtuvo la mayor selectividad a HCHO con una reacción de preoxidación previa a los experimentos catalíticos, a una temperatura de 650°C, un caudal de gas de reacción de 162,5 mL/min, una masa de catalizador de 0,6 g, una relación CH_4/O_2 de 1/1 y fracción molar de agua en la alimentación del 62%. Los catalizadores 4-FPSP con tamaños de 160~315 μm obtuvieron mayores rendimientos de HCHO.

(3), Los catalizadores de tamaño 160~315 μm fueron los más adecuados para el la operación en FBR y TZFBR. La reacción catalítica en el TZFBR alcanzó una mayor selectividad a HCHO (2,18 veces) y un mayor rendimiento a HCHO (1,46 veces) en comparación con el FBR.

References

[1] M. Ravi, M. Ranocchiari, J.A. van Bokhoven, The direct catalytic oxidation of methane to methanol—a critical assessment, Angew. Chem. Int. Ed., 56 (2017) 16464-16483.

[2] M.J. da Silva, Synthesis of methanol from methane: Challenges and advances on the multi-step (syngas) and one-step routes (DMTM), Fuel Process. Technol., 145 (2016) 42-61.

[3] B. Liu, L. Tian, L. Li, C. Au, A.C. Cheung, Performance of 3% Mo/ZSM-5 catalyst in the presence of water during methane aromatization in supersonic jet expansion, AIChE J., 57 (2011) 1852-1859.

[4] R.H. Crabtree, Aspects of methane chemistry, Chem. Rev., 95 (1995) 987-1007.

[5] D. Saha, H.A. Grappe, A. Chakraborty, G. Orkoulas, Postextraction separation, on-board storage, and catalytic conversion of methane in natural gas: a review, Chem. Rev., 116 (2016) 11436-11499.

[6] P. Tomkins, M. Ranocchiari, J.A. van Bokhoven, Direct conversion of methane to methanol under mild conditions over Cu-zeolites and beyond, Acc. Chem. Res., 50 (2017) 418-425.

[7] C. Zheng, H. Chen, Y. Yang, Q. Wang, D. Fang, Surfactant-assisted preparation of Cu/ZnO/Al_2O_3 catalyst for methanol synthesis from syngas, Mol. Catal., 366 (2013) 48–53.

[8] R. Horn, R. Schlögl, Methane activation by heterogeneous catalysis, Catal. Lett., 145 (2015) 23-39.

[9] S. Feyel, J. Döbler, R. Höckendorf, M.K. Beyer, J. Sauer, H. Schwarz, Activation of Methane by Oligomeric $(Al_2O_3)x+$ (x= 3, 4, 5): The Role of Oxygen-Centered Radicals in Thermal Hydrogen-Atom Abstraction, Angew. Chem. Int. Ed., 47 (2008) 1946-1950.

[10] E. Yang, J.G. Lee, D.H. Kim, Y.S. Jung, J.H. Kwak, E.D. Park, K. An, SiO_2@ V_2O_5@ Al_2O_3 core-shell catalysts with high activity and stability for methane oxidation to formaldehyde, J. Catal., 368 (2018) 134-144.

[11] K. Otsuka, M. Hatano, Catalysts for the synthesis of formaldehyde by partial oxidation of methane, J. Catal., 108 (1987).

[12] J.M. Fox, R.F. Geosits, A.H. Koenig, F.R. Danforth, Remote gas processing and marketing, (1987).

[13] J. Fox, ChemInform Abstract: The Different Catalytic Routes for Methane Valorization: An Assessment of Processes for Liquid Fuels, ChemInform, (1993).

[14] X. Guo, G. Fang, G. Li, H. Ma, H. Fan, L. Yu, C. Ma, X. Wu, D. Deng, M. Wei, Direct, nonoxidative conversion of methane to ethylene, aromatics, and hydrogen, Science, 344 (2014) 616-619.

[15] J.H. Lunsford, The catalytic oxidative coupling of methane, Angewandte Chemie International Edition in English, 34 (1995) 970-980.

[16] V.L. Sushkevich, D. Palagin, M. Ranocchiari, J.A. Van Bokhoven, Selective anaerobic oxidation of methane enables direct synthesis of methanol, Science, 356 (2017) 523-527.

[17] J. Shan, M. Li, L.F. Allard, S. Lee, M. Flytzani-Stephanopoulos, Mild oxidation of methane to methanol or acetic acid on supported isolated rhodium catalysts, Nature, 551 (2017) 605-608.

[18] J. Tian, J. Tan, Z. Zhang, P. Han, M. Yin, S. Wan, J. Lin, S. Wang, Y. Wang, Direct conversion of methane to formaldehyde and CO on B_2O_3 catalysts, Nat. Commun., 11 (2020) 5693.

[19] L. Zhong, F. Yu, Y. An, Y. Zhao, Y. Sun, Z. Li, T. Lin, Y. Lin, X. Qi, Y. Dai, Cobalt carbide nanoprisms for direct production of lower olefins from syngas, Nature, 538 (2016) 84-87.

[20] F. Jiao, J. Li, X. Pan, J. Xiao, H. Li, H. Ma, M. Wei, Y. Pan, Z. Zhou, M. Li, Selective conversion of syngas to light olefins, Science, 351 (2016) 1065-1068.

[21] J.H. Lunsford, Catalytic conversion of methane to more useful chemicals and fuels: a challenge for the 21st century, Catal. Today, 63 (2000) 165-174.

[22] J.A. Labinger, J.E. Bercaw, Understanding and exploiting C-H bond activation, Cheminform, 33 (2002) 507-514.

[23] J.H. Kang, E.W. Shin, W.J. Kim, J.D. Park, H.M. Sang, Selective hydrogenation of acetylene on Pd/SiO_2 catalysts promoted with Ti, Nb and Ce oxides, Catal. Today, 63 (2000) 183-188.

[24] F. Arena, A. Parmaliana, Scientific Basis for Process and Catalyst Design in the Selective Oxidation of Methane to Formaldehyde, Acc. Chem. Res., 36 (2003) 867.

[25] S. Yuan, Y. Li, J. Peng, Y. Questell-Santiago, K. Akkiraju, L. Giordano, D.J. Zheng, S. Bagi, Y. Román-Leshkov, S. Yang, Conversion of Methane into Liquid Fuels-Bridging Thermal Catalysis with Electrocatalysis, Adv. Energy Mater., 10 (2020).

[26] W.H. Cheng, Methanol and Formaldehyde Oxidation Study over Molybdenum Oxide, J. Catal., 158 (1996) 477-485.

[27] N.D. Spencer, Partial oxidation of methane to formaldehyde by means of molecular oxygen, J. Catal., 109 (1988) 187-197.

[28] N.D. Spencer, C.J. Pereira, R.K. Grasselli, The effect of sodium on the $MoO_3 \cdot SiO_2$-catalyzed partial oxidation of methane, 126 (1990) 546-554.

[29] M.R. Smith, U.S. Ozkan, The Partial Oxidation of Methane to Formaldehyde: Role of Different Crystal Planes of MoO_3, J. Catal., 141 (1993) 124-139.

[30] M.R. Smith, L. Zhang, S.A. Driscoll, U.S. Ozkan, Effect of surface species on activity and selectivity of MoO_3/SiO_2 catalysts in partial oxidation of methane to formaldehyde, Catal. Lett., 19 (1993) 1-15.

[31] L. Rodríguez, Partial oxidation of methane to formaldehyde over Mo/HZSM-5 catalysts, Appl. Catal. A-Gen., 203 (2000) 81-90.

[32] N. Ohler, A.T. Bell, Study of the elementary processes involved in the selective oxidation of methane over MoO_x/SiO_2, J. Phys. Chem. B, 110 (2006) 2700.

[33] S. Chempath, A.T. Bell, A DFT study of the mechanism and kinetics of methane oxidation to formaldehyde occurring on silica-supported molybdena, J. Catal., 247 (2007) 119-126.

[34] H. Liu, R. Liu, K. Liew, R.Johnson, J.Lunsford, Partial oxidation of methane by nitrous oxide over molybdenum on silica, J. Am. Chem. Soc., (1984).

[35] T. Sugino, A. Kido, N. Azuma, A. Ueno, Y. Udagawa, Partial Oxidation of Methane on Silica-Supported Silicomolybdic Acid Catalysts in an Excess Amount of Water Vapor, J. Catal., 190 (2000) 118-127.

[36] T. Kobayashi, K. Nakagawa, K. Tabata, M. Haruta, Partial oxidation of methane over silica catalysts promoted by 3d transition metal ions, J. Chem. Soc., Chem. Commun., (1994) 1609-1610.

[37] Q. Zhang, L. Yang, D. An, W. Ye, Catalytic behavior and kinetic features of FeO_x/SBA-15 catalyst for selective oxidation of methane by oxygen, Appl. Catal. A-Gen, 356 (2009) 103-111.

[38] Jieli, He, and, Yang, Li, and, Dongli, An, and, Qinghong, Selective oxidation of methane to formaldehyde by oxygen over silica-supported iron catalysts, J. Nat. Gas Chem., (2009).

[39] W. Ye, K. Otsuka, Structure of catalytic active site for oxidation of methane to methanol by H_2O_2 gas mixture over iron-containing catalysts, J. Mol. Catal. A-Chem, 111 (1996) 341-356.

[40] Y. Wang, O.K. Ebitani, In situ FTIR study on the active oxygen species for the conversion of methane to methanol, Catal. Lett., (1995).

[41] Xiaoxing, Wang, and, Ye, Wang, and, Qinghu, Tang, and, Qian, MCM-41-supported iron phosphate catalyst for partial oxidation of methane to oxygenates with oxygen and nitrous oxide, J. Catal., 217 (2003) 457-467.

[42] A. Matsuda, H. Tateno, K. Kamata, M. Hara, Iron phosphate nanoparticle catalyst for direct oxidation of methane into formaldehyde: effect of surface redox and acid–base properties, Catal. Sci. Technol., 11 (2021).

[43] W. Ye, X. Wang, S. Zheng, G. Qian, Q. Tang, Q. Zhang, H. Wan, SBA-15-supported iron phosphate catalyst for partial oxidation of methane to formaldehyde, Catal. Today, 93 (2004) 155-161.

[44] Q. Sun, J.I.D. Cosimo, R.G. Herman, K. Klier, M.M. Bhasin, Selective oxidation of methane to formaldehyde and C2 hydrocarbons over double layered Sr/La_2O_3 and MoO_3/SiO_2 catalyst bed, Catal. Lett., 15 (1992) 371-376.

[45] A. Sen, M. Lin, Catalytic partial oxidation of methane to methanol and formaldehyde, (2004) 48.

[46] F. Kapteijn, J. Rodriguez-Mirasol, J.A. Moulijn, Heterogeneous catalytic decomposition of nitrous oxide, Appl. Catal. B-Environ., 9 (1996) 25-64.

[47] S. Mansouri, O. Benlounes, C. Rabia, R. Thouvenot, M.M. Bettahar, S. Hocine, Partial oxidation of methane over modified Keggin-type polyoxotungstates, J. Mol. Catal. A-Chem., 379 (2013) 255-262.

[48] R. Nedyalkova, D. Niznansky, A.C. Roger, Iron-ceria-zirconia fluorite catalysts for methane selective oxidation to formaldehyde, Catal. Commun., 10 (2009) 1875-1880.

[49] M.A. Banares, L.J. Alemany, M. Lopez, Partial oxidation of methane to formaldehyde on silica-supported transition metal oxide catalysts, Catal. Today, 33 (1997) 73-83.

[50] A.D. Lucas, J.L. Valverde, P. CaIzares, L. Rodriguez, Partial oxidation of methane to formaldehyde over W/SiO_2 catalysts, 184 (1999) 143-152.

[51] A. Erdhelyi, R. Németh, A. Hancz, A. Oszkó, Partial oxidation of methane on potassium-promoted WO_3/SiO_2 and on K_2WO_4/SiO_2 catalysts, Appl. Cataly. A-Gen., 211 (2001) 109–121.

[52] Y.C. Li, Studies on the SbO_x species of SbO_x/SiO_2 catalysts for methane-selective oxidation to formaldehyde, Appl. Cataly. A-Gen., (2006).

[53] W. Ye, Y. Ohishi, T. Shishido, Q. Zhang, K. Takehira, Characterizations and catalytic properties of Cr-MCM-41 prepared by direct hydrothermal synthesis and template-ion exchange, J. Catal., 220 (2003) 347-357.

[54] H. Matsumura, K. Okumura, T. Shimamura, N.O. Ikenaga, T. Miyake, T. Suzuki, Selective oxidation of methane to formaldehyde over antimony oxide-loaded catalyst, J. of Mol. Catal. A-Chem., 250 (2006) 122-130.

[55] B. Michalkiewicz, J. Sreńscek-Nazzal, P. Tabero, B. Grzmil, U. Narkiewicz, Selective methane oxidation to formaldehyde using polymorphic T-, M-, and H-forms of niobium (V) oxide as catalysts, Chem. Pap., 62 (2008) 106-113.

[56] J. Ohyama, D. Abe, A. Hirayama, H. Iwai, Y. Tsuchimura, K. Sakamoto, M. Irikura, Y. Nakamura, H. Yoshida, M. Machida, Selective oxidation of methane to formaldehyde over a silica-supported cobalt single-atom catalyst, J. Phys. Chem. C, 126 (2022) 1785-1792.

[57] K. Tabata, T. Kawabe, Y. Yamaguchi, E. Suzuki, T. Yashima, Selective oxidation of methane over $Sn1\text{-}xGe_xO_2$, J. Catal., 231 (2005) 430-437.

[58] M.A. Aegerter, N. Leventis, M.M. Koebel, Aerogels handbook, Springer Science & Business Media, 2011.

[59] S. Alwin, X. Sahaya Shajan, Aerogels: promising nanostructured materials for energy conversion and storage applications, Materials for renewable and sustainable energy, 9 (2020) 1-27.

[60] A. Du, B. Zhou, Z. Zhang, J. Shen, A special material or a new state of matter: a review and reconsideration of the aerogel, Materials, 6 (2013) 941-968.

[61] W. Wang, M. Qiao, H. Li, J. Deng, Amorphous NiP/SiO_2 aerogel: Its preparation, its high thermal stability and its activity during the selective hydrogenation of cyclopentadiene to cyclopentene, Appl. Cataly. A-Gen., 166 (1998) L243-L247.

[62] J. Zhu, J. Xie, M. Chen, D. Jiang, Low Temperature Preparation and Visible Light Induced Photocatalytic Activity of Europium Doped Hydrophobic Anatase TiO_2–SiO_2 Photocatalysts, J. Nanosci. Nanotechno., 10 (2010) 7663-7666.

[63] A.S.S.L.N.A.B.N. Martyanov, Preparation of HKUST-1@silica aerogel composite for continuous flow catalysis, J. Sol-Gel Sci. Technol., 84 (2017).

[64] A. Lw, A. Tc, A. Jz, J.B. Yi, C. Jw, Z.A. Quan, A. Xl, High catalytic activity and stability quasi homogeneous alkali metal promoted Ni/SiO_2 aerogel catalysts for catalytic cracking of n -decane, Fuel, 268.

[65] D. Proki-Vidojevi, S.B. Glii, J.B. Krsti, A.M. Orlovi, Aerogel Re/Pd-TiO_2/SiO_2 and Co/Mo-Al_2O_3/SiO_2 catalysts for hydrodesulphurisation of dibenzothiophene and 4,6-dimethyldibenzothiophene, Catal. Today, (2020).

[66] K.T. Hassan, J. Wang, X. Han, J.J. Sharp, G.A. Bhaduri, V. Martis, L. Šiller, Catalytic Performance of Nickel Nanowires Immobilized in Silica Aerogels for the CO_2 Hydration Reaction, Acs Omega, 4 (2019) 1824-1830.

[67] N. Ettekali, S. Allahyari, N. Rahemi, F. Abedini, One-pot oxidative-adsorptive desulfurization of model and real fuel using micro-mesoporous SiO_2 aerogel supported MoO_3, Microporous Mesoporous Mater., 326 (2021) 111376-.

[68] R.M. Al Soubaihi, K.M. Saoud, J. Dutta, Low-temperature CO oxidation by silver nanoparticles in silica aerogel mesoreactors, Chem. Eng. J., 455 (2023) 140576.

[69] X. Li, G. Qin, Y. Wang, W. Wei, Keggin-type phosphotungstic acid supported on mesoporous SiO_2-Al_2O_3 aerogel like beads and their application in the isopropylation of naphthalene, J. Sol-Gel Sci. Technol., 72 (2014) 405-414.

[70] R.M. Al Soubaihi, K.M. Saoud, F. Ye, M.T.Z. Myint, S. Saeed, J. Dutta, Synthesis of hierarchically porous silica aerogel supported Palladium catalyst for low-temperature CO oxidation under ignition/extinction conditions, Microporous Mesoporous Mater., 292 (2020) 109758.

[71] P. Bansal, A. Verma, S. Talwar, Detoxification of real pharmaceutical wastewater by integrating photocatalysis and photo-Fenton in fixed-mode, Chem. Eng. J., 349 (2018) 838-848.

[72] W. Nam, J. Kim, G. Han, Photocatalytic oxidation of methyl orange in a three-phase fluidized bed reactor, Chemosphere, 47 (2002) 1019-1024.

[73] R. Zhang, H. You, T. Liu, W. Wang, D. Wu, Heterogeneous photo-Fenton degradation of quinoline with a novel internal circulating fluidized-bed reactor, Environ. Eng. Manag. J., 15 (2016).

[74] J. Herguido, M. Menéndez, Advances and trends in two-zone fluidized-bed reactors, Curr. Opin. Chem. Eng., 17 (2017) 15-21.

[75] J. Herguido, M. Menéndez, J. Santamaría, On the use of fluidized bed catalytic reactors where reduction and oxidation zones are present simultaneously, Catal. Today, 100 (2005) 181-189.

[76] L. Pérez-Moreno, J. Soler, J. Herguido, M. Menéndez, Stable hydrogen production by methane steam reforming in a two zone fluidized bed reactor: Experimental assessment, J. Power Sources, 243 (2013) 233-241.

[77] L. Pérez-Moreno, J. Soler, J. Herguido, M. Menéndez, Stable steam reforming of ethanol in a two-zone fluidized-bed reactor, Ind. Eng. Chem. Res., 51 (2012) 8840-8848.

[78] M. Lobera, C. Téllez, J. Herguido, M. Menéndez, Catalytic purification of H_2-rich streams by CO-PROX over Pt-Co-Ce/γ-Al_2O_3 in fluidized bed reactors, Catal. Today, 157 (2010) 404-409.

[79] M.P. Gimeno, J. Soler, J. Herguido, M. Menendez, Use of Fluidized Bed Reactors for Direct Gas Phase Oxidation of Benzene to Phenol, Ind. Eng. Chem. Res., 49 (2010) 6810-6814.

[80] G. García, E. Campos, I. Fonts, J. Sánchez, J. Herguido, Gas catalytic upgrading in a two-zone fluidized bed reactor coupled to a cogasification plant, Energ. Fuel., 27 (2013) 2835-2845.

[81] M.a.P. Gimeno, J. Soler, J. Herguido, M. Menéndez, Counteracting catalyst deactivation in methane aromatization with a two zone fluidized bed reactor, Ind. Eng. Chem. Res., 49 (2010) 996-1000.

[82] M.M. Sastre, J.H. Huerta, C.T. Ariso, J.S. Herrero, M.P.G. Tolosa, Method for obtaining aromatic hydrocarbons from methane, in, Google Patents, 2014.

[83] P. Ugarte, P. Durán, J. Lasobras, J. Soler, M. Menéndez, J. Herguido, Dry reforming of biogas in fluidized bed: Process intensification, Int. J. Hydrogen Energy, 42 (2017) 13589-13597.

[84] J. Fricke, Aerogels-highly tenuous solids with fascinating properties, J. Non-Cryst. Solids, 100 (1988) 169-173.

[85] J.L. Gurav, J. In-Keun, P. Hyung-Ho, E.S. Kang, D.Y. Nadargi, Silica Aerogel: Synthesis and Applications, J. Nanomater., 2010 (2010) 23.

[86] M.F. Casula, D. Loche, S. Marras, G. Paschina, A. Corrias, Role of urea in the preparation of highly porous nanocomposite aerogels, Langmuir, 23 (2007) 3509-3512.

[87] S. Liu, K. Zhu, C. Sheng, X. Shen, T. Gang, A novel building material with low thermal conductivity: Rapid synthesis of foam concrete reinforced silica aerogel and energy performance simulation, Energy Build., 177 (2018) 385-393.

[88] D.W. Schaefer, K.D. Keefer, Structure of random porous materials: Silica aerogel, Phys. Rev. Lett., 56 (1986) 2199-2202.

[89] R. Vacher, T. Woignier, J. Pelous, E. Courtens, Structure and self-similarity of silica aerogels, Phys. Rev. B, 37 (1988) 6500.

[90] J. Rouquerol, F. Rouquerol, P. Llewellyn, G. Maurin, K.S. Sing, Adsorption by powders and porous solids: principles, methodology and applications, Academic press, 2013.

[91] J. He, Y. Li, D. An, Q. Zhang, Y. Wang, Selective oxidation of methane to formaldehyde by oxygen over silica-supported iron catalysts, J. nat. gas chem., 18 (2009) 288-294.

[92] A. Parmaliana, F. Arena, F. Frusteri, A. Martınez-Arias, M.L. Granados, J. Fierro, Effect of Fe-addition on the catalytic activity of silicas in the partial oxidation of methane to formaldehyde, Appl. Catal. A-Gen., 226 (2002) 163-174.

[93] X. Wang, Y. Wang, Q. Tang, Q. Guo, Q. Zhang, H. Wan, MCM-41-supported iron phosphate catalyst for partial oxidation of methane to oxygenates with oxygen and nitrous oxide, J. Catal., 217 (2003) 457-467.

[94] M. Bowker, M. House, A. Alshehri, C. Brookes, E.K. Gibson, P.P. Wells, Selectivity determinants for dual function catalysts: applied to methanol selective oxidation on iron molybdate, Catalysis, Structure & Reactivity, (2015).

[95] C.T. Wang, R.J. Willey, Mechanistic Aspects of Methanol Partial Oxidation over Supported Iron Oxide Aerogels, J. Catal., 202 (2001) 211-219.

[96] E. Derhjelm, M.P. House, N. Cruise, J. Holmberg, M. Bowker, J.O. Bovin, A. Andersson, On the Synergy Effect in MoO_3-Fe-2(MoO_4)(3) Catalysts for Methanol Oxidation to Formaldehyde, Top. Catal., 50 (2008) 145.

[97] M. Bowker, C. Brookes, A.F. Carley, M.P. House, M. Kosif, G. Sankar, I. Wawata, P.P. Wells, P. Yaseneva, Evolution of active catalysts for the selective oxidative dehydrogenation of methanol on Fe_2O_3 surface doped with Mo oxide, Phys. Chem. Chem. Phys., 15 (2013) 12056-12067.

[98] A. Alayat, D.N. Mcllroy, A.G. Mcdonald, Effect of synthesis and activation methods on the catalytic properties of silica nanospring (NS)-supported iron catalyst for Fischer-Tropsch synthesis, Fuel Process. Technol., 169 (2018) 132-141.

[99] S. Liu, K. Yao, L.H. Fu, M.G. Ma, Selective synthesis of Fe_3O_4, γ-Fe_2O_3, and α-Fe_2O_3 using cellulose-based composites as precursors, Rsc Adv., 6 (2016).

[100] Z. Xin, Y. Niu, X. Meng, L. Yao, J. Zhao, Structural evolution and characteristics of the phase transformations between α-Fe_2O_3, Fe_3O_4 and γ-Fe_2O_3 nanoparticles under reducing and oxidizing atmospheres, Crystengcomm, 15 (2013) 8166-8172.

[101] Z. Zhao, Y. Cui, Y. Kong, J. Ren, X. Jiang, W. Yan, M. Li, J. Tang, X. Liu, X. Shen, Thermal and Mechanical Performances of the Superflexible, Hydrophobic, Silica-Based Aerogel for Thermal Insulation at Ultralow Temperature, ACS appl. Mater. interfaces, 13 (2021) 21286-21298.

[102] F.G. Denardin, O.W. Perez-Lopez, Methane dehydroaromatization over Fe-M/ZSM-5 catalysts (M= Zr, Nb, Mo), Microporous Mesoporous Mater., 295 (2019) 109961.

[103] A. Kostyniuk, D. Key, M. Mdleleni, Effect of Fe-Mo promoters on HZSM-5 zeolite catalyst for 1-hexene aromatization, J. Saudi Chem. Soc., 23 (2019) 612-626.

[104] T. Horikawa, D.D. Do, D. Nicholson, Capillary condensation of adsorbates in porous materials, Adv. Colloid Interface Sci., 169 (2011) 40-58.

[105] C. Brookes, P.P. Wells, N. Dimitratos, W. Jones, E.K. Gibson, D.J. Morgan, G. Cibin, C. Nicklin, D. Mora-Fonz, D.O. Scanlon, The nature of the molybdenum surface in iron molybdate. The active phase in selective methanol oxidation, J. Phys. Chem. C, 118 (2014) 26155-26161.

[106] F.G. Nogueira, J.H. Lopes, A.C. Silva, R.M. Lago, J.D. Fabris, L.C. Oliveira, Catalysts based on clay and iron oxide for oxidation of toluene, Appl. Clay Sci., 51 (2011) 385-389.

[107] S. Rajagopal, H. Marini, J. Marzari, R. Miranda, Silica-alumina-supported acidic molybdenum catalysts-TPR and XRD characterization, J. Catal., 147 (1994) 417-428.

[108] Y. Wang, K. Otsuka, Catalytic oxidation of methane to methanol with H_2-O_2 gas mixture at atmospheric pressure, J. Catal., 155 (1995) 256-267.

[109] R.L. McCormick, G.O. Alptekin, D. Williamson, T. Ohno, Methane partial oxidation by silica - supported iron phosphate catalysts. Influence of iron phosphate content on selectivity and catalyst structure, Top. Catal., 10 (2000) 115-122.

[110] W. Puthai, M. Kanezashi, H. Nagasawa, T. Tsuru, SiO_2-ZrO_2 nanofiltration membranes of different Si/Zr molar ratios: Stability in hot water and acid/alkaline solutions, J. Membr. Sci., 524 (2017) 700-711.

[111] R. Al-Oweini, H. El-Rassy, Synthesis and characterization by FTIR spectroscopy of silica aerogels prepared using several $Si(OR)_4$ and $R''Si(OR')_3$ precursors, J. Mol. Struct., 919 (2009) 140-145.

[112] E.P. Barrett, L.G. Joyner, P.P. Halenda, The determination of pore volume and area distributions in porous substances. I. Computations from nitrogen isotherms, J. Am. Chem. Soc., 73 (1951) 373-380.

[113] P. Selvam, S.K. Bhatia, C.G. Sonwane, Recent advances in processing and characterization of periodic mesoporous MCM-41 silicate molecular sieves, Ind. Eng. Chem. Res., 40 (2001) 3237-3261.

[114] Y. Zhang, C. Huang, H. Min, H. Shu, P. Gao, Q. Liang, X. Yang, L. Liu, X. Wang, Bowl-like double carbon layer architecture of hollow carbon@$FePO_4$@reduced graphene oxide composite as high-performance cathodes for sodium and lithium ion batteries, J. Alloys Compd., 795 (2019) 34-44.

[115] P. Mills, J. Sullivan, A study of the core level electrons in iron and its three oxides by means of X-ray photoelectron spectroscopy, J. Phys. D: Appl. Phys., 16 (1983) 723.

[116] M. Descostes, F. Mercier, N. Thromat, C. Beaucaire, M. Gautier-Soyer, Use of XPS in the determination of chemical environment and oxidation state of iron and sulfur samples: constitution of a data basis in binding energies for Fe and S reference compounds and applications to the evidence of surface species of an oxidized pyrite in a carbonate medium, Appl. Surf. Sci., 165 (2000) 288-302.

[117] Y. Liu, Z. Li, Y. You, X. Zheng, J. Wen, Synthesis of different structured $FePO_4$ for the enhanced conversion of methyl cellulose to 5-hydroxymethylfurfural, RSC adv., 7 (2017) 51281-51289.

[118] X.Guo, W. Ding, H. Chen, Q. Yan, Preparation and Characterization of Nanosized Fe-P-O Catalyst, Journal of Fuel Chemistry and Technology, 28 (2000) 385-387.

[119] C. Chen, Q. Chen, Y. Li, J. Yang, B. Huang, X. Liu, X. Xing, S. Xiao, S. Chen, R. Wang, Microspherical $LiFePO_{3.98}F_{0.02}$/3DG/C as an advanced cathode material for high-energy lithium-ion battery with a superior rate capability and long-term cyclability, Ionics, 27 (2021) 1-11.

[120] R. Lin, Y. Ding, L. Gong, W. Dong, W. Chen, L. Yuan, Studies on oxy-bromination of methane and coke deposition over $FePO_4/SiO_2$ catalysts, Catal. Today, 164 (2011) 34-39.

[121] V.D.B.C. Dasireddy, D. Hanzel, K. Bharuth-Ram, B. Likozar, The effect of oxidant species on direct, non-syngas conversion of methane to methanol over an $FePO_4$ catalyst material, RSC Adv., 9 (2019) 30989-31003.

[122] Q. Zhang, W. Deng, Y. Wang, Effect of size of catalytically active phases in the dehydrogenation of alcohols and the challenging selective oxidation of hydrocarbons, Chem. Commun., 47 (2011) 9275-9292.

[123] M. Faraldos, M.A. Banares, J.A. Anderson, H. Hu, I.E. Wachs, J.L.G. Fierro, Comparison of silica-supported MoO_3 and V_2O_5 catalysts in the selective partial oxidation of methane, J. Catal., 160 (1996) 214-221.

[124] Y. Xiaoqiang, D. Guoli, H. Dehua, Study on Methane Conversion over WO_{-x}/Co-Fe-Mo-O Catalysts, Petrochemical Technology, 34 (2005) 1134.

[125] V. Vargheese, J. Murakami, K.K. Bando, I.T. Ghampson, G.-N. Yun, Y. Kobayashi, S.T. Oyama, The direct molecular oxygen partial oxidation of CH_4 to dimethyl ether without methanol formation over a Pt/Y_2O_3 catalyst using an NO/NO_2 oxygen atom shuttle, J. Catal., 389 (2020) 352-365.

[126] P. Wallis, S. Wohlrab, V.N. Kalevaru, M. Frank, A. Martin, Impact of support pore structure and morphology on catalyst performance of VO_x/SBA-15 for selective methane oxidation, Catal. Today, 278 (2016) 120-126.

[127] Z. Liu, E. Huang, I. Orozco, W. Liao, R.M. Palomino, N. Rui, T. Duchoň, S. Nemšák, D.C. Grinter, M. Mahapatra, Water-promoted interfacial pathways in methane oxidation to methanol on a CeO_2-Cu_2O catalyst, Science, 368 (2020) 513-517.

Acknowledgement

First of all, I would like to give my heartfelt thanks to my supervisor, Prof. Menendez, Miguel, for your careful and patient guidance and assistance in my experiments and research. The time and effort you put into my degree makes me feel extremely fortunate and touched.

My sincere and hearty thanks and appreciations to my supervisor Prof. Xiaodong Shen. You were always there to help me in time when I encountered difficulties in research and life at school. It’s my honor to be your student for six years.

And my warm gratitude also goes to Javier Lasobras for your help with my experiments and research. It is because of you that everything went smoothly. I still remember the time I said "can I ask you if I have a problem", you looked at me sincerely and said "Always". Words merged into a sentence: thank you, Javi.

My thanks also go to Herguido, Javier and Soler, Jaime. Your patient attention and advice at each of my presentations has given me a lot of new knowledge and ideas. Your enthusiasm, kindness and friendliness have filled me with love for UNIZAR and the city of Zaragoza.

I wish to extend my thanks to Prof. Sheng Cui for all your help and guidance in keeping my degree running smoothly. Thanks to Prof. Yong Kong for providing me with an office cubicle after my return to China, which made it possible for me to complete my thesis. Thanks to counselor Anquan Wang, for all your help over the past three years.

Thanks to Jian Ren and Long Ruan for your help with my experiments. And thanks to Zhiyang Zhao, Ziqian Sun and Fuhao Xu for their advice on my research projects.

Thanks to my lucky star Yang Zhao. You appeared in my life, brighten me and be with me. My dear best friend, always have, always will.

My sincere gratitude goes to my family, you have always been the strongest backing in my life.

Finally, thanks to myself, for all the hard work and perseverance. This is not the end but a new start. Life is a great big canvas, and I am going to paint a bright and colorful painting.

June 2023
Kunmeng Zhu